AFRL-AFOSR-VA-TR-2018-0391

Novel Characterization Methods for Anisotropic and Mixed-Conduction Materials

Matthew Grayson
NORTHWESTERN UNIVERSITY
633 CLARK ST EVANSTON
EVANSTON, IL 60208-0001

10/16/2018
Final Report

Air Force Research Laboratory
AF Office Of Scientific Research (AFOSR)/RTA1

REPORT DOCUMENTATION PAGE

Form Approved
OMB No. 0704-0188

PLEASE DO NOT RETURN YOUR FORM TO THE ABOVE ORGANIZATION.

1. REPORT DATE *(DD-MM-YYYY)*	2. REPORT TYPE	3. DATES COVERED *(From - To)*
08-10-2018	Final Performance Report	15 Jun 2015 through 14 Jun 2018

4. TITLE AND SUBTITLE
Novel Characterization Methods for Anisotropic and Mixed-Conduction Materials

5a. CONTRACT NUMBER

5b. GRANT NUMBER
FA9550-15-1-0247

5c. PROGRAM ELEMENT NUMBER

6. AUTHOR(S)
Grayson, Matthew A.

5d. PROJECT NUMBER

5e. TASK NUMBER

5f. WORK UNIT NUMBER

7. PERFORMING ORGANIZATION NAME(S) AND ADDRESS(ES)
Northwestern University
633 Clark St
Evanston, IL 60208-0001

8. PERFORMING ORGANIZATION REPORT NUMBER

9. SPONSORING/MONITORING AGENCY NAME(S) AND ADDRESS(ES)
USAF, AFRL DUNS 143574726
AF Office of Scientific Research
875 North Randolph Street, RM 3112
Arlington, VA 22203-1954

10. SPONSOR/MONITOR'S ACRONYM(S)

11. SPONSOR/MONITOR'S REPORT NUMBER(S)

12. DISTRIBUTION/AVAILABILITY STATEMENT
Approved for public release; distribution is unlimited

13. SUPPLEMENTARY NOTES

14. ABSTRACT

As per the motivational statement of this grant proposal, state-of-the-art electronic and optoelectronic devices require electronic materials with specialized properties that cannot be characterized with standard methods, or that must be characterized with extra precision. New materials characterization methods have been developed under the three years of support of this grant. These new characterizations led to 3 patents and 8 refereed publications including 2 PRL's, with several additional works in submission. Students graduated with support of this grant include 5 PhD's and 1 MS. Collaborations in this work included international partners (Germany, Israel, and China), collaborations with industry (Teledyne), AFRL (Wright-Patterson), and other US universities (U. Michigan, Alabama U.) The newly developed characterization methods were:
I. Carrier density gradient analysis method; II. Fourier-domain mobility spectral analysis; III. Heterodyne 4-point method for precision Hall effect; IV. Anisotropic conductor characterization; V. Heavy-tail transient analysis; VI. Disorder scaling in non-ohmic conductivity of 2D materials; and VII. Percolation model for electrical and thermal conductivity in disordered media.

15. SUBJECT TERMS
Density gradient; mobility spectral analysis; heterodyne Hall effect; anisotropic conductivity; heavy-tail transient; disorder scaling; percolation conductivity.

16. SECURITY CLASSIFICATION OF:			17. LIMITATION OF ABSTRACT	18. NUMBER OF PAGES	19a. NAME OF RESPONSIBLE PERSON
a. REPORT	b. ABSTRACT	c. THIS PAGE			Matthew A. Grayson
U	U	U	UU	62	19b. TELEPHONE NUMBER *(Include area code)* (847) 491-8137

Title: **Novel Characterization Methods for Anisotropic and Mixed-Conduction Materials**
PI: **Matthew Grayson, Northwestern University**
Division: **Complex Materials and Devices**
Project Manager: **Ken Goretta**

FINAL REPORT ABSTRACT:
As per the motivational statement of this grant proposal, state-of-the-art electronic and optoelectronic devices require electronic materials with specialized properties that cannot be characterized with standard methods, or that must be characterized with extra precision. New materials characterization methods have been developed under the three years of support of this grant. These new characterizations led to 3 patents and 8 refereed publications including 2 PRL's, with several additional works in submission. Students graduated with support of this grant include 5 PhD's and 1 MS. Collaborations in this work included international partners (Germany, Israel, and China), collaborations with industry (Teledyne), AFRL (Wright-Patterson), and other US universities (U. Michigan, Alabama U.)

A short summary of these newly developed characterization methods is provided below:

I. *Carrier density gradient analysis method:* Semiconductor uniformity is essential for all semiconductor applications, including optoelectronic light emitters & sensors, IC's, and logic devices. This method extends the van der Pauw method of electrical characterization so that one can measure small variations in the doping density of semiconductor samples typical to semiconductor devices.

II. *Fourier-domain mobility spectral analysis*: This method allows for electrons and holes of differing mobilities to be separated out from magnetotransport data. The experimental system of interest was lightly *n*-type quantum wells of $Hg_{1-x}Cd_xTe$, which revealed ambipolar conduction of both electrons and holes.

III. *Heterodyne 4-point method for electrical characterization of time varying conductivities*: A new method was developed to improve the sensitivity of Hall measurements by orders of magnitude. This heterodyne Hall effect technique uses ac signal multiplication to measure a pure Hall resistance R_{xy} (B) in arbitrarily shaped samples.

IV. *Anisotropic conductor characterization*: With five contacts, it was demonstrated in a black phosphorus nanolayer that three independent four-point resistance measurements can determine the three independent components of an in-plane anisotropic resistivity tensor. Also, a detailed method for measuring in-plane and cross-plane conductivities of a superlattice has been formally described.

V. *Heavy-tail transient analysis*: Disordered systems exhibit a range of time-scales and manifest slow switching transients, or "heavy-tail" relaxations, which limit performance. An equation was derived that fits all classes of heavy-tail functions, and was experimentally applied in both the low- and high-disorder limits in 2D transistors of black phosphorus.

VI. *Disorder scaling in non-ohmic conductivity of 2D materials:*
In 2D conductors, the gated conductivity is typically non-linear, with changes in the surface

adsorbed gases leading to changes in both the doping level and the mobility. We demonstrate that all of the characterization curves *at different adsorbate concentrations, dopings, and disorder* can all be collapsed ***onto a single universal curve*** that is characteristic of that particular material.

VII. *Percolation model for electrical and thermal conductivity in disordered media:*
Disordered porous media are described in a modified percolation model that is adapted for polymer composites under uniaxial pressure. Percolation is also shown to describe thermal conductivity in metal-organic frameworks fabricated by combustion synthesis.

Note: All eight (8) publications funded by this grant are appended at the end of this report. The remainder of this report is on Year #3 activities alone. The reports from Year #1, Year #2, and the section below on Year #3 have no overlap, and are intended to be read together as a detailed breakdown of the entire 3-year grant activities.
==========

Summary of efforts in Year #3: (6/15/17-6/14/18)

Year #3 advanced the ability to characterize anisotropic conductors with the publication of a new 5-point method. With five contacts, it was demonstrated in a black phosphorus nanolayer that three independent four-point resistance measurements can be made to determine the three independent components of the anisotropic resistivity tensor. The Fourier-domain mobility spectral analysis was also demonstrated experimentally in a publication on HgCdTe in collaboration with Teledyne. Studies of heavy-tail transient relaxation in disordered conductors were shown to obey a universal equation derived for the first time by the PI. Such transients occur in the electrical and mechanical relaxations of amorphous semiconductors, polymers, and other disordered media of technical interest to the Air Force. The importance of being able to predict the asymptotic value of heavy-tail relaxations is of significant technical relevance for efficient reliability testing. Disordered materials were also studied in regimes where they become anisotropic, such as under pressure, and both electrical and thermal conductivity were well-explained by percolation models. Collaborations in this work included international partners (Germany, Israel, and China), collaborations with industry (Teledyne), AFRL (Wright-Patterson), and other US universities (U. Michigan, Alabama U.)

A detailed breakdown is provided below:

1) *Anisotropic conductor characterization*:
Anisotropic in-plane conductors include 2D materials like black phosphorus, and anisotropic cross-plane conductors include superlattices for optical detectors and emitters. Such materials require different characterization techniques than isotropic conductors, to characterize the 3 independent terms of the conductivity tensor. The new 5-point method [2,8] for characterizing the anisotropic conductivity tensor of 2D materials, such as black phosphorus, has now been published in PRL. The method requires that the geometry of the sample be measured, and then a series of five different 4-point measurements identifies a mutually consistent conductivity tensor. We have also submitted a patent application for the equations and methods for testing in-plane and cross-plane conductivity of superlattices. [1] A one-dimensional wire fabricated with a core-shell structure represents the most extreme example of anisotropic conductivity, conducting only in one direction. Such core-shell wires can be designed for high mobility,

whereby the core region is made of a quantum well material like GaAs and the surrounding shell is made of a barrier material like AlGaAs. For such a system, when the dopants are placed in the shell material, an extreme high mobility wire can be fabricated. Here by gating the wire with a side-gate, it becomes possible to observe conductance steps each time a mode gets depopulated. The energy of the modes is observed to correlate with the gate voltages at which depopulation occurs, confirming that the structure of the wires does, in fact, match the intended electronic structure. [3] (Collaboration with **Technical University of Munich**)

2) *Magnetotransport and Fourier-domain mobility spectral analysis for mixed-conduction materials*:
The magnetotransport equipment purchased under this grant provided the measurement capabilities to characterize new materials. Among the new materials characterized were polycrystalline ZrTe5, whose magnetotransport was fit to a 2-band model as bulk narrow-gap semiconductor [5]. The temperature dependence of the Hall effect was used to prove that the Fermi energy drops from the conduction band to the valence band as the temperature decreases, making the Hall sign switch from n-type, to mixed-conduction, to p-type. Another new material was MoS2 nanoparticles synthesized according to a new solid-state reaction that allows small porous nanoparticles to be synthesized rapidly at high temperatures without any aggregation of nanoparticles into larger particles [6]. This synthesis is important for catalysis applications, for example. The Hall effect characterization showed that the resulting porous nanoparticles of MoS2 demonstrated a similar carrier density and resisitivity as bulk MoS2, suggesting that the nanoparticles were single-domain oriented crystals, in spite of being porous. In addition to standard magnetotransport characterization, we also conducted an analysis method developed by the PI called Fourier-transform mobility spectral analysis, which allows for electrons and holes of differing mobilities to be separated out from magnetotransport data. The system of interest was lightly *n*-type quantum wells of $Hg_{1-x}Cd_xTe$, which revealed ambipolar conduction of both electrons and holes. The holes were observed to have a lower mobility and lower density than the electrons, as expected. [4,9] (Collaboration with **U. Michigan & Teledyne**)

3) *Heavy-tail transient analysis in disordered conductors*:
As described in the Year #2 report, in the process of studying anisotropic 2D conductors it was observed that the disorder potential in 2D systems leads to unusual transient effects. When a disordered system relaxes from one steady state to another, often many time scales are involved, such that the overall decay is slower than a simple exponential decay. Such a response is called a "heavy-tail transient" [8]. Normally such transients are associated with amorphous systems [10], but we have demonstrated in a recent paper submission [11] that, remarkably, the same behavior occurs in gated two-dimensional (2D) materials. The exact formula for the generic transient described by dispersive diffusion is:

$$\sigma(t) = \sigma_f + \Delta\sigma \frac{1-C}{e^{(t/\tau)^{\beta(1-C)}} - C} \qquad (1)$$

This powerful equation was first derived by the PI in Ref. [11] and is able to explain an entire class of heavy-tail responses from the stretched exponential decay in one limit ($C \to 0$) to the algebraic decay in the other limit ($C \to 1$). This heavy tail transient was first identified and

characterized in indium-gallium-zinc-oxide amorphous semiconductors, and a parameterization of the experimental data was developed in terms 4-fit parameters in Eq. 1 ($\Delta\sigma$, τ, β, and C) [10]. The PI working with collaborators identified the utility of this heavy-tail fit in an extremely broad class of relaxation phenomena from photoconductivity to piezoresistance, and in an extremely broad class of materials from semiconductor superlattices to 2D materials to concrete blocks. The eight different research thrusts are categorized below, and include three **national collaborations** with universities and **AFRL** labs, as well as two international collaborations with **Israel** and **China**.

Heavy-tail relaxation dynamics have been identified in the following highly disordered electronic systems:

a) *Photoconductivity relaxation in indium gallium-zinc-oxide (IGZO)*: Exposure to ultraviolet light causes non-equilibrium dissociation of oxygen bonds, reducing the coordination number of the cations. When light is turned off, these deep-level traps and their random configuration cause a distribution of trap capture times. (**Grayson**, et al. [10])
b) *Piezoresistance relaxation in composite-polymer foams*: Semiconducting nanoparticles in a polymer matrix with micron-scale air voids show a pressure dependent conductivity. The heavy-tail relaxation of this conductivity with a step change in pressure can be explained through a percolation model of densification with dispersive diffusion dynamics. (**Grayson**, et al. [13])
c) *Plastic conductivity relaxation in nanotube/silicone composites*: Carbon nanotubes in a matrix of silicone rubber make a conductive composite whose conductivity can be used to measure the instantaneous stress. As the composite stretches under plastic deformation, the slow change in stress results in a changing conductivity. (Collaboration with **Noa Lachman-Senesh, Tel Aviv U.**)
d) *Lifetime studies of nanostructured lithium ion battery cathodes*: Graphitic cathodes can be made for lithium ion batteries so that a very large surface area allows for rapid charging / discharging. The stored charge per cycle decays, however, per cycle number following a heavy-tail relaxation. (Collaboration with **Mark Hersam, Northwestern U.**)

The fit is also applicable to disorder in the following semiconductor systems that are not normally considered "highly disordered:"

e) *Gated photoconductivity transients of black phosphorus 2D flakes*: (**Grayson**, et al. [11]) Disorder in black phosphorus flakes can be tuned by intentional exposure to ozone, and heavy-tail transients are shown to relax with different qualitative functional forms depending on whether the sample is pristine (algebraic decay, $C \rightarrow 1$ in Eq. 1, above) or disordered (stretched exponential, $C \rightarrow 0$ in Eq. 1, above). This represents the **first time** that a heavy tail relaxation has been shown to be **tuned by disorder**, and the **first time** that **dispersive diffusion** dynamics have been proposed for **2D materials.**
f) *Type-II superlattice photoluminescence:* Interface roughness leads to a disordered potential for trapping electrons and holes. The relaxation time distribution is due to statistically varying separations between trapped electrons and trapped holes, which leads to statistically distributed luminescence times. (Collaboration with **Elizabeth Steenbergen, AFRL, Wright-Patterson**)
g) MoS_2 photoconductivity: Illumination of a MoS_2 transistor leads to a transient photodecay that fits a heavy-tail response. Again, photoluminescence may be restricted by disorder, in

this case disorder caused by interface roughness, as well as local and remote ionized impurities, and adsorbed gases. (Collaboration with **Patrick Kung, U. Alabama**)

The fit is also generalizable to relaxation in non-electronic systems:

h) *Concrete stress relaxation*: Under constant stress, concrete blocks slowly undergo strain relaxation through microcracks and other deformations. Such relaxations are conjectured to obey the same relaxation equations. (Collaboration with **Sumei Zhang, Harbin Institute of Technology, China**)

4) *Disorder scaling in non-ohmic conductivity of 2D materials:*
In the process of studying 2D conductors, the common effect was observed that the gated conductivity is non-linear, and that changes in the surface adsorbed gases lead to changes in both the doping level and the mobility. The adsorbate dependence of a 2D transistor is typically plotted as a series of apparently dissimilar characterization curves at different adsorbate concentrations. We conducted studies of 2D materials of MoS_2 and Bi_2Te_3 [8,12] to demonstrate that all of these characterization curves *at different adsorbate concentrations* can all be collapsed ***onto a single universal curve*** that is characteristic of that particular material. The theoretical model to explain this behavior makes only two simple assumptions: 1) that the disorder potential amplitude is proportional to the number of adsorbates; and 2) that the effect of screening on the disorder potential can be approximated by a simple dielectric constant. This scaling effect of the disorder potential should lead to simpler and more rigorous characterizations of all 2D transistor sensor devices.

5) *Percolation model for electrical and thermal conductivity in disordered media:*
The last system to be characterized was disordered porous media, which can become anisotropic under uniaxial pressure. The first example is a composite conductor of semiconducting micron-scale grains mixed with a small amount of polymer and up to 50% air [13]. Such systems are typically called composite polymer foams. We studied the conductivity of the extruded threads of such polymer foams as a function of pressure lateral to the threads. We observed that the conductivity of the threads can fit a power law in pressure, indicative of a percolation model for the conductivity. Remarkably, this model seems to be the first time that percolation theory has been applied to the conductivity of composites. Aligned with the importance of characterizing electrical conductivity of percolating networks is the importance of characterizing thermal conductivity. The studies of metal organic framework thermal conductivity grown by combustion synthesis were shown to fit well with a percolation model [7,9]. These metal organic frameworks are important as absorbent layers for natural gas storage in future low-emission vehicles.

List of patents:
[1] "SYSTEM AND METHOD FOR STRIPLNE ELECTRODES FOR THIN FILM CHARACTERIZATION" Patent Pending: 62/427,048 Filing Date: 2017.
Inventors: Matthew Grayson and Yang Tang. This method describes how three parallel stripline electrodes can be used to measure the in-plane and out-of-plane conductivity tensors of a thin film on a conducting substrate. With a B-field parallel to the striplines, the magnetic field dependence of the resistivity tensor yields the density, in-plane, and out-of-plane mobility of multiple electron and hole species. Such mixed conduction anisotropic thin-film layers are standard for IR and THz emitters and detectors.

List of publications and papers:
[2] Lintao Peng, Spencer A. Wells, Christopher R. Ryder, Mark C. Hersam, and **M. Grayson**, *"All-electrical determination of crystal orientation in anisotropic two-dimensional materials,"* Phys. Rev. Lett. **120**, 086801 (2018).

[3] Dominik M. Irber, Jakob Seidl, Damon J. Carrad, Jonathan Becker, Nari Jeon, Bernhard Loitsch, Julia Winnerl, Sonja Matich, Markus Döblinger, Yang Tang, Stefanie Morkötter, Gerhard Abstreiter, Jonathan J. Finley, Matthew Grayson, Lincoln J. Lauhon, and Gregor Koblmüller, "*Quantum transport and subband structure of modulation-doped GaAs/AlAs core-superlattice nanowires*," Nano Letters **17**, 4886 (2017).

[4] Justin Easley, Erdem Arkun, Boya Cui, Michael Carmody, Lintao Peng, **M. Grayson**, and Jamie Phillips, "*Analysis of Carrier Transport in n-type $Hg_{1-x}Cd_xTe$ with Ultra-Low Doping Concentration*," J. Electronic Materials **47**, 5699 (2018).

[5] S. A. Miller, I. Witting, U. Aydemir, Lintao Peng, A. J. E. Rettie, P. Gorai, D. Y. Chung, M. G. Kanatzidis, **M. Grayson**, V. Stevanović, E. S. Toberer, and G. J. Snyder "*Polycrystalline $ZrTe_5$ parametrized as a narrow-band-gap semiconductor for thermoelectric performance*," Phys. Rev. Applied **9**, 014025 (2018).

[6] Saiful M. Islam, Jeffrey D. Cain, Fengyuan Shi, Yihui He, Lintao Peng, Abhishek Banerjee, Kota S. Subrahmanyam, Yuan Li, Shulan Ma, Vinayak P. Dravid, **Matthew Grayson**, and Mercouri G. Kanatzidis, "*Conversion of Single Crystal $(NH_4)_2Mo_3S_{13}{\cdot}H_2O$ to Isomorphic Pseudocrystals of MoS_2 Nanoparticles,*" Chem. Mater. **30**, 3847 (2018).

[7] B. Cui, C. O. Audu, Yijun Liao, SonBinh T. Nguyen, Omar K. Farha, J. T. Hupp, and **M. Grayson,** "*Thermal Conductivity of ZIF-8 Thin-Film under Ambient Gas Pressure*," ACS Applied Materials & Interfaces **9**, 28139 (2017).

[8] Lintao Peng, PhD Thesis: "*Novel transport characterizations in layered two-dimensional materials and bulk chalcogenides*", Northwestern University (2017).

[9] Boya Cui, PhD Thesis: "*Thermal and Electrical Transport in Thin-Film Materials for Energy Management*", Northwestern University (2017).

List of manuscripts submitted or in preparation:
[10] Jiajun Luo, Stephan D. Kim, Woongkyu Lee, R.P.H. Chang, and M. Grayson, "*Dispersive Diffusion Limited Transient Photoresponse in a-IGZO Thin Films*," (in preparation for Phys. Rev.

Lett.).

[11] Lintao Peng, Jiajun Luo, Spencer A. Wells, Mark C. Hersam, Matthew Grayson, "*Parameterizing hysteresis dynamics in two-dimensional materials: "Heavy-tail switching transients in black phosphorous*," (in review for Phys. Rev. Lett.)

[12] Lintao Peng, Spencer A. Wells, Mark C. Hersam, and Matthew Grayson, "*Disorder scaling of conductivity versus density in two-dimensional black phosphorous*," (in preparation for Appl. Phys. Lett).

[13] M. Wang, R. Gurunathan, K. Imasato, A. Jakus, J. Peng, R. Shah, M. Grayson, J. G. Snyder "*Percolation Model for Piezoresistivity in Polymer-Conductor Composites*," (submitted to Advanced Theory and Simulations)

Students graduated:

Lintao Peng (2017) PhD Thesis: "*Novel transport characterizations in layered two-dimensional materials and bulk chalcogenides*"

Boya Cui (2017) PhD Thesis: "*Thermal and Electrical Transport in Thin-Film Materials for Energy Management*"

Awards won:

AT&T Research Professorship Chair in EECS Department, Northwestern University

Analyzing Longitudinal Magnetoresistance Asymmetry to Quantify Doping Gradients: Generalization of the van der Pauw Method

Wang Zhou,[1] H. M. Yoo,[1] S. Prabhu-Gaunkar,[1] L. Tiemann,[2] C. Reichl,[2] W. Wegscheider,[2] and M. Grayson[1,*]
[1]Electrical Engineering and Computer Science, Northwestern University, Evanston, Illinois 60208, USA
[2]Laboratory for Solid State Physics, ETH Zürich, 8093 Zürich, Switzerland
(Received 14 December 2014; published 28 October 2015)

A longitudinal magnetoresistance asymmetry (LMA) between a positive and negative magnetic field is known to occur in both the extreme quantum limit and the classical Drude limit in samples with a nonuniform doping density. By analyzing the current stream function in van der Pauw measurement geometry, it is shown that the electron density gradient can be quantitatively deduced from this LMA in the Drude regime. Results agree with gradients interpolated from local densities calibrated across an entire wafer, establishing a generalization of the van der Pauw method to quantify density gradients.

DOI: 10.1103/PhysRevLett.115.186804 PACS numbers: 73.43.-f, 72.20.My, 73.50.Jt

Experimental measurements of longitudinal magnetoresistance R_{xx} in semiconductor quantum wells (QWs) can show asymmetry with respect to a positive and negative magnetic field B. At large fields and low temperatures in the quantum Hall (QH) regime, larger R_{xx} peaks appear for one sign of the magnetic field, and smaller or vanishing R_{xx} peaks for the opposite field [1] obeying the Onsager-Casimir relations [2–4]. However, the underlying cause of the asymmetries remained unknown until more recent work by Pan *et al.* [5] in the fractional QH regime, whereby quantized R_{xx} maxima were explained by assuming an electron density difference across the sample. Motivated by this experiment, Ilan *et al.* [6] introduced a stream-function [7] model for current flow in the QH regime under an electron density gradient in the high-B limit $\rho_{xx} \ll \rho_{xy}$, and they were able to explain the key features observed by Pan, where ρ_{xx} and ρ_{xy} are the longitudinal and transverse resistivities, respectively.

Despite the relevance of the above work, the low-magnetic field Drude limit, whereby resistivity components $\rho_{xx} \sim \rho_{xy}$ are of the same order, has a much broader practical scope than the restricted QH regime considered above. The majority of semiconductor characterizations are in this low-B limit, such as room temperature characterizations of samples with any mobility, and moderate-mobility magnetotransport of samples at any temperature. The above analysis of Ilan *et al.* also suffers from the significant drawback that it is not able to deduce the two independent components of the density gradient from a single sample. Yet, density anisotropies are important to characterize since spurious effects in QH traces [1,5] can result from wafer-scale density variations inherent to epitaxial growth [8], and inaccurate estimates of the activation energies of the QH regime are shown to result from anisotropic current flow [9]. Thus, there remain significant challenges for magnetotransport characterization of inhomogeneously doped samples.

In this Letter, the longitudinal magnetoresistance asymmetry (LMA) is comprehensively studied for an *arbitrarily* oriented density gradient in the more broadly relevant low-magnetic field Drude limit, and a method to *quantitatively* measure both components of the density gradient is developed and calibrated against interpolated local densities of neighboring samples. Drastically asymmetric longitudinal resistance is observed in van der Pauw (vdP) samples [10] in both the QH and the Drude regime (Fig. 1). We find that upon entering the Drude regime at higher temperatures, the LMA can be quantitatively explained with a model that assumes a density gradient in a classical Drude conductor. This LMA analysis deduces the magnitude and direction of the density gradient ∇n as well as the local resistivity $\rho_0(B)$ from a consideration of four-point resistances at both positive and negative B fields. Such a technique promises to revolutionize magnetotransport characterization, allowing one to estimate density gradients with a simple extension of the vdP method [10]. We verify the validity and reproducibility of this LMA method on square samples cleaved from a high-mobility GaAs QW wafer. Both the angle and the magnitude of the density gradients from this method match those interpolated from local electron density measurements.

Our experiments were carried out on a two-inch wafer hosting a 30 nm-wide GaAs QW, with an average electron density $\bar{n} = 2.6 \times 10^{11}$ cm^{-2} and mobility $\bar{\mu} = 6.6 \times 10^6$ cm^2/V · s at $T = 1$ K. The wafer was grown by molecular beam epitaxy in a Gen II Varian chamber without any rotation during growth, leading to moderate density gradients as large as 20%/cm caused by the asymmetric positioning of the Ga, Al, and Si-dopant fluxes. The wafer was diced into 4×4 mm^2 square samples that were each contacted with four indium dots on the corners and four on the flats of each side, and then alloyed. Samples were measured in both a dilution refrigerator and ^{4}He flow

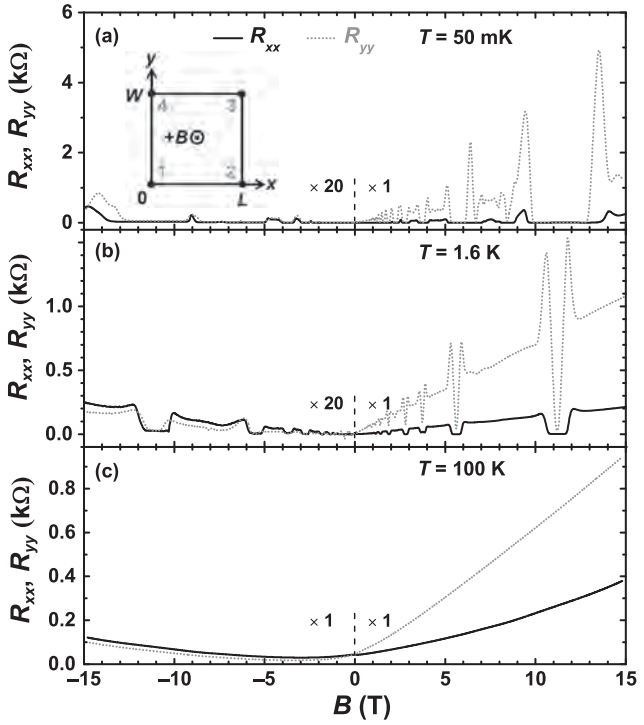

FIG. 1. Asymmetric longitudinal magnetoresistance $R_{xx} = R_{43,12}$ and $R_{yy} = R_{32,41}$ of sample D4 in the QH regime at (a) $T = 50$ mK, (b) 1.6 K, and in the Drude regime at (c) $T = 100$ K. The curves for $-B$ fields are magnified by 20 times for (a) and (b) in order to see subtle features. Note how the asymmetry exaggerates with decreasing temperature. (Inset) Sample layout for a square sample $L = W$.

cryostat ($T = 50$ mK–300 K) with standard lock-in techniques.

Figure 1 shows the two longitudinal resistances $R_{xx} = R_{43,12}$ and $R_{yy} = R_{32,41}$ of sample D4 measured at $\pm B$ fields at $T = 50$ mK, 1.6 K, and 100 K. The notation $R_{43,12}$ means current is sent from contact 4 to 3, and voltage is measured at contact 1 relative to 2 [10,11]. According to the symmetry of the measurement, one would expect a perfectly homogeneous sample to exhibit the same longitudinal resistances R_{xx} and R_{yy} for $+B$ and $-B$ fields. However, at the lowest temperatures, an extreme anisotropy is observed in the QH R_{xx} and R_{yy} traces [Fig. 1(a)], which decreases with increasing temperature [Fig. 1(b)], but still persists up to the Drude limit at $T = 100$ K [Fig. 1(c)]. The analysis below will focus on this high temperature Drude regime where quantum oscillations vanish. To stay within the Drude limit, the temperature was kept above $T \geq 30$ K to suppress quantum oscillations and below $T \leq 100$ K to avoid parallel conduction in the doping layers.

To theoretically model the observed LMA, a rectangular sample (Fig. 1 insert) with a local density gradient is considered. The resistivities obey the local Drude equations $\rho_{xx}(\mathbf{r}) = 1/[n(\mathbf{r})e\mu(\mathbf{r})]$ and $\rho_{xy}(\mathbf{r}) = \mp B/[n(\mathbf{r})e]$ for a B-field pointing out of the page in the $+z$-direction, and a stream function ψ describes the current density $\mathbf{j}(\mathbf{r}) = \hat{\mathbf{z}} \times \boldsymbol{\nabla}\psi(\mathbf{r})$ [7]. In this manuscript, wherever dual polarities are indicated $\pm$ or $\mp$, the upper polarity describes p-type samples, and the lower n-type. The local electric field $\mathbf{E}(\mathbf{r}) = \boldsymbol{\rho}(\mathbf{r})\mathbf{j}(\mathbf{r})$ must satisfy $\nabla \times \mathbf{E} = 0$ in steady state, leading to

$$\rho_{xx}\nabla^2\psi + \nabla\rho_{xx} \cdot \nabla\psi - \hat{\mathbf{z}} \cdot (\nabla\psi \times \nabla\rho_{xy}) = 0. \quad (1)$$

We then solve Eq. (1) under more general conditions than previously considered: whereas Ref. [6] neglects $\nabla\rho_{xx}$ in Eq. (1) for the high-mobility and high magnetic field limit, this term must be preserved for the general treatment derived here. And unlike Ref. [6], we consider a density gradient that can be oriented in an *arbitrary* direction.

The $\nabla\rho_{xx}$ and $\nabla\rho_{xy}$ gradients can be defined in terms of a normalized density gradient,

$$\boldsymbol{\eta} = (\eta_x, \eta_y) = \frac{\nabla n}{n_0}. \quad (2)$$

The local mobility is assumed to follow a power-law dependence on local density according to the standard screening assumption $\mu(\mathbf{r}) = \mu_0[n(\mathbf{r})/n_0]^\gamma$, typically $0.5 < \gamma < 1.5$ [12–14]. The subscript 0 identifies local values at the center of the sample, whereby n_0 is the density, $\mu_0(B)$ the B-dependent mobility, and $\rho_0(B) = 1/n_0 e\mu_0(B)$ the B-dependent Drude resistivity at the center of the sample. The resulting resistivity gradients to first order in $\boldsymbol{\eta}$ become

$$\nabla\rho_{xx} = -\rho_0(1+\gamma)\boldsymbol{\eta}, \qquad \nabla\rho_{xy} = \pm\rho_0\mu_0 B\boldsymbol{\eta}. \quad (3)$$

Equation (1) is now evaluated keeping all derivative terms up to first order, and the four-point longitudinal resistance at finite B becomes

$$R_{xx} = R_{43,12} = -\frac{\rho_0}{I}\int_{x_2}^{x_1}\left(-\frac{\partial\psi}{\partial y}\right)_{y=0} dx = e^{W/2\xi_x}\sum_{m=1}^{\infty}\frac{2m^2\pi^2 L\rho_0\lambda_m}{\sinh\left(\frac{1}{2}\lambda_m W\right)}\frac{[1-(-1)^m\cosh\left(L/2\xi_y\right)]}{[(L/2\xi_y)^2 + m^2\pi^2]^2}, \quad (4)$$

with length scale $\boldsymbol{\xi} = (\xi_x, \xi_y)$ defined in terms of the components of $\boldsymbol{\eta}$:

$$\frac{1}{\xi_x} = \pm\mu_0 B\eta_x - (1+\gamma)\eta_y, \qquad \frac{1}{\xi_y} = \pm\mu_0 B\eta_y + (1+\gamma)\eta_x, \quad (5)$$

where

$$\lambda_m = \sqrt{[B^2\mu_0^2 + (1+\gamma)^2]\eta^2 + 4m^2\pi^2/L^2}. \quad (6)$$

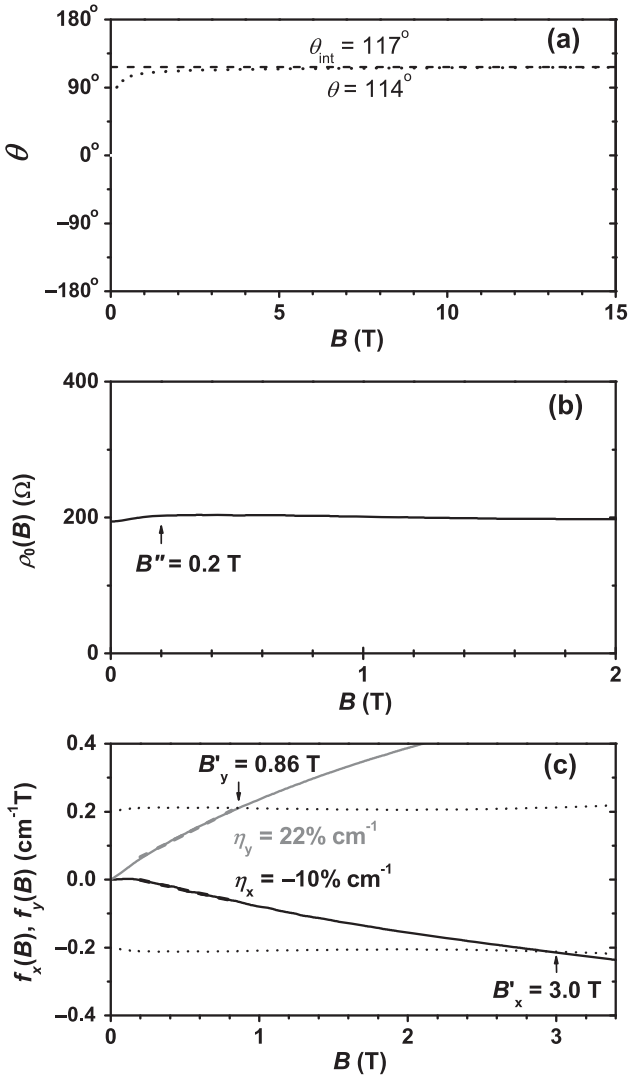

FIG. 2. Gradient angle θ, resistivity ρ_0, and gradient parameters f_x and f_y are plotted as a function of B for sample D4. (a) The dotted line θ is constant 114° except at the lowest B, and it compares favorably to the dashed line $\theta_{\rm int} = 117°$ interpolated from neighboring samples. (b) $\rho_0(B)$ exhibits flat Drude behavior everywhere except below $B'' = 0.2$ T. (c) Normalized density gradient components η_x and η_y determined from the slopes of the linear fitting lines of $f_x(B)$ (black) and $f_y(B)$ (grey) within $B'' < B < B'$. Intersection of solid lines with dotted lines indicate upper magnetic field range of Drude behavior B'_x and B'_y (see text).

The analogous expression for $R_{yy} = R_{32,41}$ follows from the simple rotation transformation $x \to -y$, $y \to x$, $\xi_x \to -\xi_y$, $\xi_y \to \xi_x$, and $L \rightleftharpoons W$.

In this Letter, we consider only physically reasonable density gradients across a roughly square sample ($W \sim L$), such that the percent of density variation δ across the sample defines a small parameter,

$$\delta = \frac{\Delta n}{n_0} = |\boldsymbol{\eta} \cdot (L\hat{x} + W\hat{y})|. \tag{7}$$

Here, Δn represents the maximum change in density across the sample, and the relative accuracy of all expressions below are specified in terms of δ.

The first task is to identify the angle of the density gradient θ over the full range of B. Upon evaluating the ratio $R_{xx}(+B)/R_{xx}(-B)$ from Eq. (4), the B-symmetric component of the exponential prefactor cancels, as does the summation term which is approximately symmetric in B for small δ, leaving

$$\ln \frac{R_{xx}(+B)}{R_{xx}(-B)} = \pm W \eta_x \mu_0(B) B. \tag{8}$$

The corresponding expression for R_{yy} follows from the rotation transformation, and combined with Eq. (8) the density gradient angle θ becomes

$$\tan\theta = \frac{\eta_y}{\eta_x} = -\frac{\ln \frac{R_{yy}(+B)}{R_{yy}(-B)}}{\ln \frac{R_{xx}(+B)}{R_{xx}(-B)}} \frac{W}{L}, \tag{9}$$

accurate to within an error of less than $\frac{1}{2}\delta$.

To test Eq. (9), we independently estimate a density gradient angle $\theta_{\rm int}$ interpolated from the densities of neighboring samples. Figure 2(a) compares the interpolated result $\theta_{\rm int} = 117°$ to θ from the LMA method of Eq. (9). The gradient angle θ compares favorably and is constant at 114° over the entire range except for the lowest magnetic fields.

The second task is to determine $\rho_0(B)$, the B-dependent local resistivity, in the low-B limit. From Eq. (6) and its rotation transform, λ_m is independent of the magnetic field below $B'_x = 1/(\mu_0|\eta_x|W)$ and $B'_y = 1/(\mu_0|\eta_y|L)$. Therefore, $B \le B' = \min\{B'_x, B'_y\}$ sets the range where the approximation $\lambda_m \approx 2m\pi/L$ is valid [15], simplifying Eq. (4),

$$R_{xx}(B) = e^{W/2\xi_x}\rho_0(B)\frac{16}{\pi}[\tanh^{-1}(e^{-\pi(W/L)}) + \sinh^2(L/4\xi_y)\ln(1+e^{-\pi(W/L)})]. \tag{10}$$

Equation (8) and its rotation transform along with Eq. (5) define $\boldsymbol{\eta}$ and $\boldsymbol{\xi}$, in turn. Substituting into Eq. (10) and solving for ρ_0 gives an expression for the resistivity which we label ρ_0^a,

$$\rho_0^a(B) = \sqrt{R_{xx}(+B)R_{xx}(-B)}\,\frac{\pi}{16}\left[\tanh^{-1}(e^{-\pi(W/L)}) + \sinh^2\left(\ln\frac{R_{yy}(+B)}{R_{yy}(-B)}/4\right)\ln(1+e^{-\pi(W/L)})\right]^{-1}. \tag{11}$$

The rotation transformed Eq. (11) is labeled ρ_0^b, and the most accurate estimate of $\rho_0(B)$ is their average,

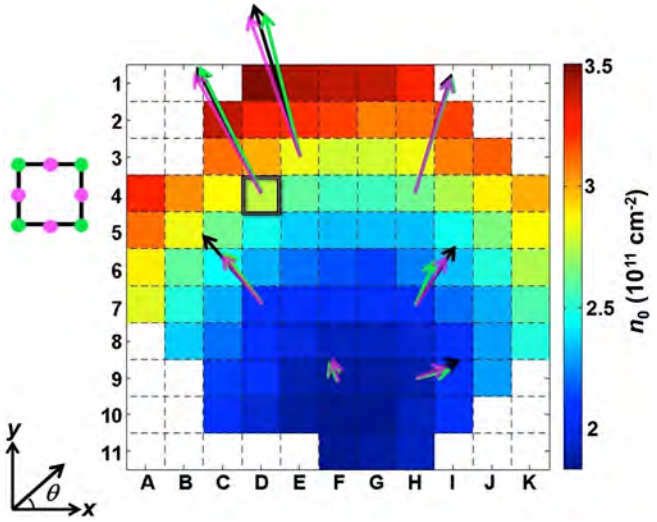

FIG. 3 (color online). Density color map of a two-inch GaAs QW wafer calibrated by dicing into 4×4 mm^2 samples and measuring the local density n_0 of various samples. Black arrows represent local density gradients $\nabla n_{\rm int} = n_0 \boldsymbol{\eta}_{\rm int}$ interpolated from this density map. Green (pink) arrows represent LMA method density gradients $\nabla n = n_0 \boldsymbol{\eta}$ using corner (flat) contacts, as shown in the inset, left. Sample D4 is presented in greater detail (Figs. 1 and 2).

$$\rho_0(B) = \frac{1}{2}[\rho_0^a(B) + \rho_0^b(B)], \tag{12}$$

accurate to within δ.

Equations (11) and (12) generalize the classic van der Pauw equations [10] for the case of a density gradient. The four contacted corners of the sample can all have different local resistivity and density, yet these equations can still estimate the local resistivity in the center of a sample $\rho_0(B)$. The result is plotted in Fig. 2(b) for sample D4, showing a Drude-like response with very little dependence on B except near $B = 0$ T, where quantum phase coherent effects such as weak localization [16–18] and memory effects [19–22] as well as electron-electron interactions [23,24] may play a role. We will, therefore, identify a lower limit for Drude-like behavior as B'', which for sample D4 is $B'' = 0.2$ T.

The final task is to deduce the components of the density gradient from the low-B data. Multiplying Eq. (8) and its rotated counterpart on both sides by $\rho_0(B)$ yields the functions

$$f_x(B) = \pm\frac{n_0 e}{W}\rho_0(B)\ln\frac{R_{xx}(+B)}{R_{xx}(-B)} = \eta_x B,$$
$$f_y(B) = \mp\frac{n_0 e}{L}\rho_0(B)\ln\frac{R_{yy}(+B)}{R_{yy}(-B)} = \eta_y B. \tag{13}$$

Their slopes in B give the normalized density gradient

$$\nabla n/n_0 = \boldsymbol{\eta} = \left(\frac{df_x}{dB}, \frac{df_y}{dB}\right). \tag{14}$$

In a perfect Drude model, these slopes would persist to $B = 0$ T, but since B'' sets the lower limit of the Drude behavior, we only expect a linear fit within the domain $B'' < B < B'$.

Figure 2(c) illustrates how the density gradient can be deduced graphically. The functions $f_x(B)$ and $f_y(B)$ are plotted as solid lines along with $\mathrm{sgn}[f_x(B)]/[\mu_0(B)W]$ and $\mathrm{sgn}[f_y(B)]/[\mu_0(B)L]$, respectively, as dotted lines, where the sign function is defined $\mathrm{sgn}(x) = +1$ for $x \geq 0$ and $\mathrm{sgn}(x) = -1$ for $x < 0$. The condition for $B'_x = 1/\mu_0|\eta_x|W$ and $B'_y = 1/\mu_0|\eta_y|L$ is graphically determined from their intersection, and the B-field range delimiter, B' is identified with the lesser of B'_x or B'_y. From Fig. 2(c), the density gradient components $\eta_x = -10\%$ cm^{-1} and $\eta_y = 22\%$ cm^{-1} are then extracted from the slopes of the linear fitting lines within the domain $B'' < B < B'$.

We can verify this LMA analysis across an entire wafer by creating an interpolated density map. The wafer is illustrated in Fig. 3 with various colored tiles designating the local measured densities. The interpolated normalized density gradients $\boldsymbol{\eta}_{\rm int} = \nabla n_{\rm int}/n_0$ were deduced by calculating the first derivative of the density map smoothed via the so-called QR algorithm [25]. In addition to D4, six other samples marked with origins of each arrow in Fig. 3 were selected, and density gradients $\nabla n_{\rm int}$ deduced from the interpolated data are plotted as black arrows. For comparison, the density gradient magnitudes and angles for these same samples were also determined with the LMA method, and $\nabla n = n_0 \boldsymbol{\eta}$ is plotted with green arrows. Conformal equivalence [26,27] also allows us to use the four flat contacts (pink, Fig. 3 inset) at the center of each side to measure the density gradient, provided we rotate the resulting angle by 45°, with the result plotted in Fig. 3 as pink arrows. In the limit of a weak uniform density gradient these results agree quantitatively [28]. The overlap of these gradient vectors verifies the consistency of the LMA method for calibrating density gradients.

As Fig. 3 demonstrates, the LMA analysis has the practical consequence of providing a quick and simple evaluation of density gradients of 2D conducting layers of single samples, in contrast to the cumbersome task of measuring the densities and mobilities of neighboring samples. To measure high-mobility samples such as those investigated here, higher temperatures are needed to increase the resistivity ρ_0 and thereby increase B' so that a wider range of B field can be used to extract the density gradient magnitude.

To summarize, we observed an asymmetry in the longitudinal resistance in the QH and Drude regimes, and we developed an analytical model to extract the density gradient. Equations (9) and (11)–(14) are unique to this work, and they allow one to calculate the angle and magnitude of the density gradient, as well as the local resistivity $\rho_0(B)$, from the longitudinal resistances R_{xx} and R_{yy} in both $+B$ and $-B$ fields. The physics discussed here allows one to quantify the uniformity of 2D materials such

as graphene [29,30], MoS_2 [31–33], WS_2 [34], β-metallic phosphorus [35], and topological insulators [36,37], where individual micron-sized exfoliated samples do not have the luxury of having "neighboring" pieces to deduce density gradients. This work generalizes the classic vdP analysis to handle the case of a density gradient.

This work was supported by a McCormick Catalyst Award from Northwestern University, the Department of Electrical Engineering and Computer Science Bridge Funding, and AFOSR FA9550-15-1-0247. The authors would like to thank Professor Dominik Zumbühl at the University of Basel for the motivational discussions.

*m-grayson@northwestern.edu

[1] F. Fischer, M. Grayson, E. Schuberth, D. Schuh, M. Bichler, and G. Abstreiter, Physica (Amsterdam) **22E**, 108 (2004).
[2] L. Onsager, Phys. Rev. **38**, 2265 (1931).
[3] H. B. G. Casimir, Rev. Mod. Phys. **17**, 343 (1945).
[4] H. H. Sample, W. J. Bruno, S. B. Sample, and E. K. Sichel, J. Appl. Phys. **61**, 1079 (1987).
[5] W. Pan, J. S. Xia, H. L. Stormer, D. C. Tsui, C. L. Vicente, E. D. Adams, N. S. Sullivan, L. N. Pfeiffer, K. W. Baldwin, and K. W. West, Phys. Rev. Lett. **95**, 066808 (2005).
[6] R. Ilan, N. R. Cooper, and A. Stern, Phys. Rev. B **73**, 235333 (2006).
[7] I. M. Ruzin, N. R. Cooper, and B. I. Halperin, Phys. Rev. B **53**, 1558 (1996).
[8] Y. Liu, L. N. Pfeiffer and K. W. West (private communication).
[9] J. P. Eisenstein (private communication).
[10] L. J. van der Pauw, Philips Res. Rep. **13**, 1 (1958).
[11] B. S. Kim, W. Zhou, Y. D. Shah, C. Zhou, N. Isik, and M. Grayson, Rev. Sci. Instrum. **83**, 024703 (2012).
[12] L. Pfeiffer, K. W. West, H. L. Stormer, and K. W. Baldwin, Appl. Phys. Lett. **55**, 1888 (1989).
[13] B. E. Kane, L. N. Pfeiffer, K. W. West, and C. K. Harnett, Appl. Phys. Lett. **63**, 2132 (1993).
[14] K. Hirakawa and H. Sakaki, Phys. Rev. B **33**, 8291 (1986).
[15] This case is more likely to occur in smaller samples or at higher resistivities ρ_0, which can be found at higher temperatures in high-mobility samples such as the ones studied here.
[16] E. McCann, K. Kechedzhi, V. I. Falko, H. Suzuura, T. Ando, and B. L. Altshuler, Phys. Rev. Lett. **97**, 146805 (2006).
[17] T. Hassenkam, S. Pedersen, K. Baklanov, A. Kristensen, C. B. Sorensen, P. E. Lindelof, F. G. Pikus, and G. E. Pikus, Phys. Rev. B **55**, 9298 (1997).
[18] L. Bockhorn, P. Barthold, D. Schuh, W. Wegscheider, and R. J. Haug, Phys. Rev. B **83**, 113301 (2011).
[19] E. M. Baskin and M. V. Entin, Physica (Amsterdam) **249B–251B**, 805 (1998).
[20] A. D. Mirlin, J. Wilke, F. Evers, D. G. Polyakov, and P. Wolfle, Phys. Rev. Lett. **83**, 2801 (1999).
[21] A. Dmitriev, M. Dyakonov, and R. Jullien, Phys. Rev. Lett. **89**, 266804 (2002).
[22] L. Bockhorn, I. V. Gornyi, D. Schuh, C. Reichl, W. Wegscheider, and R. J. Haug, Phys. Rev. B **90**, 165434 (2014).
[23] I. V. Gornyi and A. D. Mirlin, Phys. Rev. B **69**, 045313 (2004).
[24] E. A. Galaktionov, A. K. Savchenko, and D. A. Ritchie, Phys. Status Solidi C **3**, 304 (2006).
[25] J. G. F. Francis, Computer Journal (UK) **4**, 265 (1961).
[26] L. V. Bewley, *Two-Dimensional Fields in Electrical Engineering* (MacMillan, New York, 1948).
[27] N. Zeev, *Conformal Mapping* (Dove, New York, 1975).
[28] W. Zhou, L. Peng, M. Fouda, and M. Grayson (to be published).
[29] B. Ozyilmaz, P. Jarillo-Herrero, D. Efetov, D. A. Abanin, L. S. Levitov, and P. Kim, Phys. Rev. Lett. **99**, 166804 (2007).
[30] J. Jobst, D. Waldmann, I. V. Gornyi, A. D. Mirlin, and H. B. Weber, Phys. Rev. Lett. **108**, 106601 (2012).
[31] B. Radisavljevic, A. Radenovic, J. Brivio, V. Giacometti, and A. Kis, Nat. Nanotechnol. **6**, 147 (2011).
[32] K. F. Mak, C. Lee, J. Hone, J. Shan, and T. F. Heinz, Phys. Rev. Lett. **105**, 136805 (2010).
[33] D. Xiao, G.-B. Liu, W. Feng, X. Xu, and W. Yao, Phys. Rev. Lett. **108**, 196802 (2012).
[34] H. S. S. R. Matte, A. Gomathi, A. K. Manna, D. J. Late, R. Datta, S. K. Pati, and C. N. R. Rao, Angew. Chem., Int. Ed. Engl. **49**, 4059 (2010).
[35] L. Li, Y. Yu, G. J. Ye, Q. Ge, X. Ou, H. Wu, D. Feng, X. H. Chen, and Y. Zhang, Nat. Nanotechnol. **9**, 372 (2014).
[36] N. Bansal, Y. S. Kim, M. Brahlek, E. Edrey, and S. Oh, Phys. Rev. Lett. **109**, 116804 (2012).
[37] K. Nomura and N. Nagaosa, Phys. Rev. Lett. **106**, 166802 (2011).

Editors' Suggestion

All-Electrical Determination of Crystal Orientation in Anisotropic Two-Dimensional Materials

Lintao Peng,[1] Spencer A. Wells,[2] Christopher R. Ryder,[2] Mark C. Hersam,[1,2,3,4,*] and Matthew Grayson[1,3,†]
[1]Applied Physics Graduate Program, Northwestern University, Evanston, Illinois 60208, USA
[2]Department of Materials Science and Engineering, Northwestern University, Evanston, Illinois 60208, USA
[3]Department of Electrical Engineering and Computer Science, Northwestern University, Evanston, Illinois 60208, USA
[4]Department of Chemistry, Northwestern University, Evanston, Illinois 60208, USA

(Received 20 October 2017; revised manuscript received 7 December 2017; published 21 February 2018)

The crystal orientation of an exfoliated black phosphorous flake is determined by purely electrical means. A sequence of three resistance measurements on an arbitrarily shaped flake with five contacts determines the three independent components of the anisotropic in-plane resistivity tensor, thereby revealing the crystal axes. The resistivity anisotropy ratio decreases linearly with increasing temperature T and carrier density reaching a maximum ratio of 3.0 at low temperatures and densities, while mobility indicates impurity scattering at low T and acoustic phonon scattering at high T.

DOI: 10.1103/PhysRevLett.120.086801

Layered two-dimensional (2D) materials, also called van der Waals materials, have an anisotropic crystal structure, allowing micromechanical exfoliation into thin sheets. However, many important 2D materials including black phosphorus (BP), GaTe, ReS_2, SnS, and WTe_2 possess additional in-plane structural anisotropy that manifests as an anisotropic in-plane resistance [1–5]. For example, BP is a high mobility layered semiconductor with a band gap from 0.3 to 1.7 eV as its thickness is decreased from bulk to monolayer [1,6–8]. Its properties have been demonstrated in electronics as field-effect transistors [1,2,9] and optoelectronics as photodetectors [10,11]. Of particular importance are the anisotropic properties of BP, including quasi-1D excitons in the monolayer limit, a half-linear, half-parabolic dispersion under hydrostatic pressure, and anisotropic negative Poisson's ratio under compression [12–16]. All such anisotropic studies require identification of the crystallographic orientation of BP, which until now has required polarized Raman and optical reflection spectroscopy [2,7,11,17]. However, there currently exists no electrical method to accurately measure the crystal orientation in as-exfoliated BP. Prior electrical methods to quantify anisotropy have strict geometric constraints on the sample shape and/or crystallographic orientation, limiting their utility with exfoliated materials [18–21]. The radial starburst contact pattern commonly employed in 2D anisotropy characterization is only qualitatively accurate due to the two-point series contact resistances and the short circuiting of current through the many peripheral contacts [2,22].

Here, an all-electrical technique quantifies the anisotropic resistivity tensor of arbitrarily shaped few-layer flakes of BP, thereby revealing in-plane crystal orientation. Three or more four-point resistance measurements that use at least five contacts at the periphery of a thin flake can determine the three unknowns—the c- and a-axis resistivity, and anisotropy angle—via geometric transformations including conformal mapping. The crystallographic orientation deduced from this all-electrical conformal five-contact (C5C) method is confirmed with polarized Raman spectroscopy. For the first time, both temperature and carrier density dependence of the electrical anisotropy are reported in the same flake in an exfoliated 2D material.

Devices were fabricated using black phosphorus micromechanically exfoliated onto a degenerately doped Si wafer with a 300 nm thermal SiO_2 film. This served as the gate electrode and gate dielectric, respectively. Electron beam lithography was used to define device features, and the electrodes consisted of thermally evaporated Ni/Au 10/40 nm. In order to minimize oxidation during processing, the device was stored in a glovebox, and anhydrous 1-methyl-2-pyrrolidone was used for resist liftoff. After device fabrication, alumina was deposited *via* atomic layer deposition in order to encapsulate the device.

There are a total of three unknowns in the 2D anisotropy problem. Here we parametrize them as the anisotropy angle θ between the x-y lab basis and the c-a crystal basis, the sheet resistivity determinant $\rho_s^2 = \|\boldsymbol{\rho}\|$, and a geometric anisotropy scaling factor $\alpha = \sqrt[4]{\rho_{cc}/\rho_{aa}} \leq 1$. The c-a axes represent the right-handed coordinate system for the armchair and zigzag directions in black phosphorus, respectively, and θ subtends the angle between the laboratory x axis and the crystal c axis. Though, in general, no analytical expression can solve these three unknowns in terms of measured four-point resistances, it is nonetheless straightforward to compute the inverse problem, namely, to calculate the four-point resistance value R_k for a given sample shape and contact configuration k when the

parameters ρ_s, θ, and α are known. From such an expression, each four-point resistance measurement then constrains the space of possible ρ_s, θ, and α values, and the intersection of three such subspaces from three different measurements will define the unique solution for ρ_s, θ, and α.

The first step is therefore to calculate this 4-point resistance function R_k for the sample shape of interest in terms of prescribed ρ_s, θ, and α parameters. A photograph of the exfoliated flake will be used to define a polygon approximation to the sample shape, and three coordinate transformations will be performed that each preserve the resistivity determinant. As an example, consider the polygon-shaped sample in Fig. 1(a) with $V = 7$ geometric vertices. The anisotropic 2D resistivity direction set by θ is depicted graphically with rectangular cross-hatched lines, where the widely (closely) spaced green (blue) lines

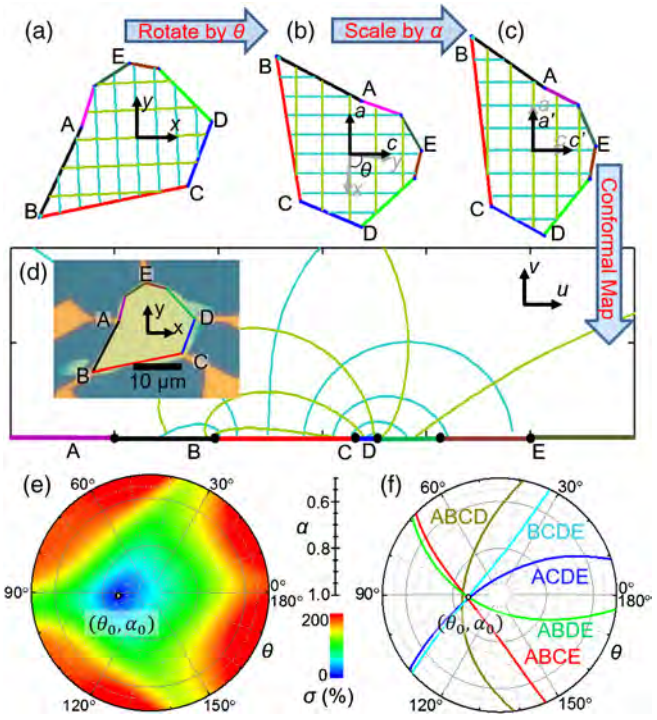

FIG. 1. Conformal five-contact method on *anisotropic* BP sample *A*. (a) Polygon approximation of the sample in the *x*-*y* lab frame. (b) Rotation by θ to the *c*-*a* crystal axes. (c) Anisotropic scaling of crystal axes by $1/\alpha$ and α, respectively, to equivalent *isotropic* resistivity sample in the c'-a' basis. (d) Conformal mapping to the semi-infinite *u*-*v* plane. Inset photo: sample *A* in the lab frame overlaid with polygon approximation. All four-point resistances of the original anisotropic sample are identical to those of the semi-infinite plane. (e) C5C Variance minimization method: color plot of normalized variance $\sigma(\alpha, \theta)$ from Eq. (3) on a 2θ polar plot with minimum variance at $\theta_0 = 93°$ and $\alpha_0 = 0.85$ ($r = 1.9$), where $\rho_{s,0} = 11$ kΩ. (f) C5C Parametric intersection method: shown are various $\alpha(\theta)$ curves on a 2θ polar plot. Variance minimization method results in (e) agree with parametric intersection results in (f).

represent the high- (low-) resistivity direction. Of these seven vertices, $N = 5$ represent contacts, labeled *A*–*E*. The contacts can also be located along flat edges using the same coordinate transformations and analysis. Because each transformation preserves the resistivity determinant, the sheet resistivity scale ρ_s can be factored out of the expression for the four-point resistance:

$$R_k(\rho_s, \theta, \alpha) = \rho_s f_k(\theta, \alpha). \tag{1}$$

The resulting geometric function $f_k(\theta, \alpha)$ for a given sample geometry and contact configuration k depends on the rotation and scale transformation variables θ and α, respectively. The first transformation [Fig. 1(b)] is a counterclockwise rotation by the anisotropy angle θ from the *x*-*y* lab basis to the *c*-*a* crystal basis. The second transformation [Fig. 1(c)] is an anisotropic scaling [23] where the new c'-a' axes are scaled by $1/\alpha$ and α, respectively, and the anisotropy scaling factor α maps the original *anisotropic* conductor to an equivalent *isotropic* conductor with the same sheet resistivity determinant:

$$\begin{pmatrix} c' \\ a' \end{pmatrix} = \begin{pmatrix} 1/\alpha & 0 \\ 0 & \alpha \end{pmatrix} \begin{pmatrix} \cos\theta & \sin\theta \\ -\sin\theta & \cos\theta \end{pmatrix} \begin{pmatrix} x \\ y \end{pmatrix}. \tag{2}$$

The third and final determinant-preserving step is the reverse Schwarz-Christoffel transformation. A *forward* Schwarz-Christoffel transformation [24] maps a coordinate $w = u + iv$ in the upper half *u*-*v* plane to a point $\zeta = c' + ia'$ within a polygon in the c'-a' plane according to the complex integral,

$$\zeta(w) = \int_0^w \frac{1}{(\zeta - u_1)^{1-\beta_1/\pi}(\zeta - u_2)^{1-\beta_2/\pi}(\zeta - u_3)^{1-\beta_3/\pi}\ldots} d\zeta, \tag{3}$$

where u_i are points along the *u* axis in the *u*-*v* plane, which map to vertices (c_i', a_i') of the polygon in the c'-a' plane with subtended vertex angles β_i. The *reverse* Schwarz-Christoffel transformation is simply the computational inverse of this one-to-one mapping, from the polygon to the upper half-plane [25]. The geometric function for any four-point resistance can now be calculated analytically from the point u_i along the boundary of the semi-infinite plane [26]:

$$f_{lm,np} = \frac{1}{\pi} \ln\left(\frac{(u_n - u_l)(u_p - u_m)}{(u_p - u_l)(u_n - u_m)}\right) \equiv f_k. \tag{4}$$

Here l, m label the $\pm$ current and n, p the $\pm$ voltage contact pairs, respectively, of the kth contact configuration,

where $k = \{1, ..., M\}$ for the total number of $M = 2\binom{N}{4}$ independent configurations.

In practice, the number Q of four-point resistances actually measured is typically more than 3, and the unknowns ρ_s, θ, and α are determined from a simple variance minimization based on Eq. (1). Solving Eq. (1) to define a parametric dependence of the sheet resistivity on the transformation parameters $\rho_{s,k}(\theta, \alpha) = R_k / f_k(\theta, \alpha)$, the normalized variance σ of the candidate sheet resistivities can be written as a function of θ and α,

$$\sigma(\theta, \alpha) = \frac{1}{\langle \rho_{s,k}(\theta, \alpha) \rangle} \sqrt{\frac{\sum_{k=1}^{Q} [\rho_{s,k}(\theta, \alpha) - \langle \rho_{s,k}(\theta, \alpha) \rangle]^2}{Q}}. \tag{5}$$

The coordinates (θ_0, α_0) that minimize this variance reveal the unique solution for the crystallographic orientation θ_0 and anisotropy scaling factor α_0. The sheet resistance is then the average value at the point of minimum variance $\rho_{s,0} = \langle \rho_{s,k}(\theta_0, \alpha_0) \rangle$. The final 2D anisotropic resistivity tensor becomes $\rho_{cc} = \alpha_0^2 \rho_{s,0}$ and $\rho_{aa} = \alpha_0^{-2} \rho_{s,0}$.

The variance minimization C5C method was applied to sample A [Fig. 1(d), inset], whose polygon approximation was introduced above. Sample A is a $d = 31$ nm thick micromechanically exfoliated BP flake with sheet carrier density $p = 1.77 \times 10^{12}$ cm^{-2} measured at 300 K. The resulting variance $\sigma(\theta, \alpha)$ of $Q = 10$ different measured contact configurations is shown in Fig. 1(e). Because the variance $\sigma(\theta, \alpha) = \sigma(\theta + 180°, \alpha)$ is periodic with period 180°, the minimum can be uniquely represented in a 2θ polar plot whereby the graphical angle is twice the anisotropy angle θ, and the isotropic condition $\alpha = 1$ is at the polar center. The global minimum is observed at $\theta_0 = 93°$ and $\alpha_0 = 0.85$ yielding $\rho_{s,0} = 11 \pm 1$ kΩ with anisotropy ratio $r = (\rho_{aa}/\rho_{cc}) = \alpha_0^{-4} = 1.9$. This result is consistent with previous reported values on both bulk [27] and thin flake BP devices [2,28].

Because sheet resistance in *isotropic* 2D samples is often measured with the van der Pauw (vdP) technique, we introduce a second, equivalent C5C method for measuring *anisotropic* resistivity, which we call the vdP parametric intersection method [Fig. 1(f)]. Consider two four-point resistances R_k and $R_{k'}$ chosen such that k and k' are vdP pairs of measurement contacts, whereby the same four contacts are used such as $ABCD$, but cyclically permuted among the current and voltage contacts, such as $k = \{AB, DC\}$ and $k' = \{BC, AD\}$ [26]. From the two resistance measurements R_k and $R_{k'}$, the standard vdP method gives the value for the isotropic sheet resistivity ρ_s, which for anisotropic samples represents the square-root-determinant resistivity [23] and sets a parametric constraint on $\alpha(\theta)$. For example, Fig. 1(f) shows $M = Q/2 = 5$ different parametric curves $\alpha(\theta)$ on a 2θ polar plot for the five possible sets of four contacts. Wherever any two curves intersect, a consistent solution of α and θ exists, and the final solution is the average of (ρ_s, θ, α) at all intersections. For sample A, the result is $\rho_{s,0} = 11 \pm 1$ kΩ, $\theta_0 = 93° \pm 3°$, and $\alpha_0 = 0.85 \pm 0.01$, such that $r = 1.9 \pm 0.1$ in excellent agreement with the C5C variance-minimization results. To confirm the conformal five-contact methods in Fig. 2, we investigated an MoS_2 device sample C with thickness $d = 8$ nm that is *not* expected to show anisotropy. The result confirms a very weak anisotropy of only $\alpha_0 = 0.99$ and $r = \alpha_0^{-4} = 1.05$, with the variance minimum in the center of the radial plot, with degenerate solutions of θ_0 and a sheet resistivity $\rho_{s,0} = 69$ kΩ.

The anisotropy angle θ_0 determined by the C5C method in BP sample A [Fig. 3(a)] was independently verified using polarized Raman spectroscopy [Fig. 3(b)]. Polarizing the incident 532 nm laser parallel to the detector polarization, the armchair (c axis) and zigzag (a axis) directions of BP can be determined [17]. Raman measurements of the BP flake were taken by rotating the material in 10° increments, generating polarization-dependent Raman spectra. By fitting intensities of the A_g^2 spectra, [29] the angle of minimum Raman intensity is $\theta_R = 97° \pm 5°$ [Fig. 3(c)], in agreement with the more accurate C5C measurement of $\theta_0 = 93° \pm 3°$ [Fig. 3(a)]. Note that the encapsulation of the BP flake with atomic layer deposited alumina protects against accelerated degradation due to laser irradiation, and that the laser wavelength was chosen to be transparent to the alumina [30].

The utility of this method is illustrated by studying temperature- and hole-density dependence on another BP

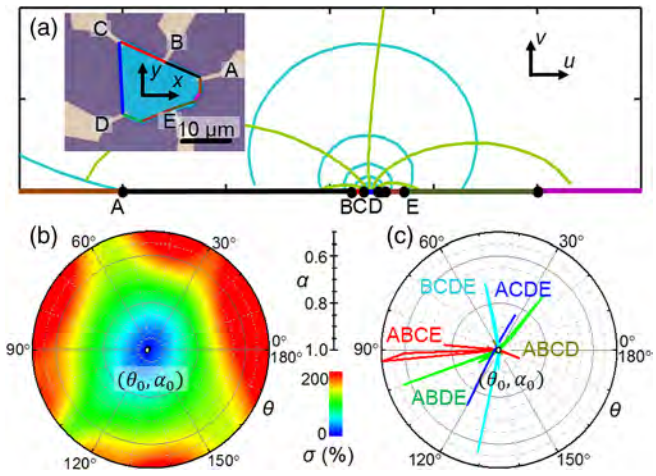

FIG. 2. Conformal five-contact method on the *isotropic* MoS_2 sample C. (a) Inset photo: sample C in the lab frame overlaid with polygon approximation; the main panel shows conformal mapping to the semi-infinite u-v plane. (b) C5C Variance minimization method: color plot of normalized variance $\sigma(\alpha, \theta)$ [Eq. (3)] on a 2θ polar plot with minimum variance at $\alpha_0 = 0.99$ ($r = 1.05$) at the center of polar plot, where $\rho_{s,0} = 69$ kΩ. (c) C5C Parametric intersection method: shown are various $\alpha(\theta)$ curves on a 2θ polar plot. Variance minimization results in (b) agree with parametric intersection results in (c).

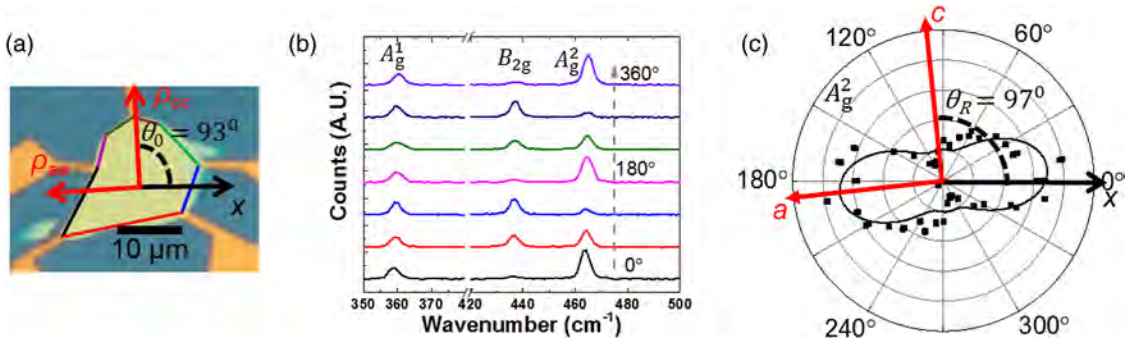

FIG. 3. Comparison between the anisotropy angle determined by the C5C method and polarized Raman spectrum on BP sample A. (a) Crystal orientation determined by the C5C method in Fig. 1 is $\theta_0 = 93° \pm 3°$. (b) Selected polarized Raman spectra on sample A with polarization angle rotating from 0° to 360°. (c) Radiii of black dots on the polar plot represent peak amplitudes for polarized Raman intensities of the A_g^2 peak, with the black curve representing a theoretical fit. Resulting Raman crystal orientation angle is $\theta_R = 97° \pm 5°$ in agreement with more accurate θ_0 from the C5C method.

sample (sample B) with thickness $d = 28$ nm that has $N = 6$ contacts. Here $Q = 14$ contact combination measurements were chosen, since more measurements allow greater redundancy in 4-point resistance measurements and greater accuracy in anisotropy calibration. From these measurements, the anisotropy angle is $\theta_0 = 68°$ at 300 K, agreeing again with Raman spectroscopy (results not shown) within ±5°, and the anisotropy ratio is $r = 2.5$ for sheet carrier density $p = 4.78 \times 10^{11}$ cm^{-2}.

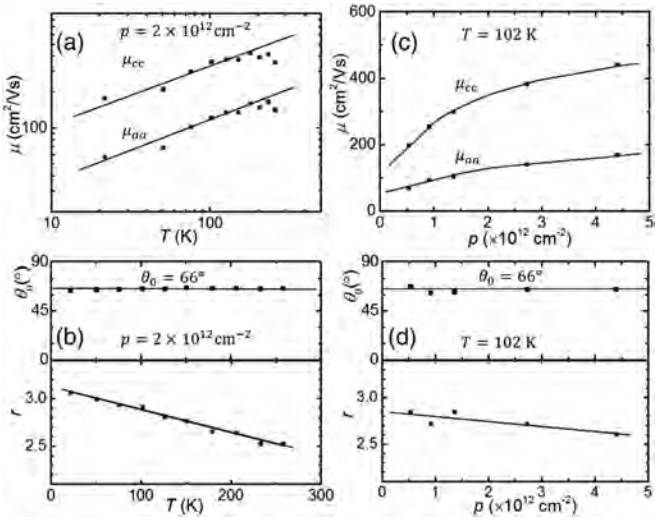

FIG. 4. Anisotropy analysis on BP sample B ($d = 28$ nm) as a function of density and temperature. Curves are guides to the eye. (a) Temperature dependence: at fixed density, carrier mobilities μ_{cc} and μ_{aa} along the armchair and zigzag directions, respectively, both increase with a power law in the low-temperature range, before saturating at high temperatures, indicating the onset of phonon scattering. (b) At fixed density, anisotropy angle θ_0 (top panel) remains constant, and ratio r (bottom panel) decreases linearly with temperature. (c) Density dependence: Carrier mobilities μ_{cc} and μ_{aa} increase with increasing carrier density. (d) Anisotropy angle θ_0 (top panel) remains constant while the anisotropy ratio r (bottom panel) decreases slightly with carrier density.

The temperature dependence of the anisotropy ratio was studied by holding the hole density of sample B fixed at $p = 2.0 \times 10^{12}$ cm^{-2} with gate bias. As shown in Fig. 4(a), both the a- and c-direction mobilities show positive power-law increase in the low-temperature range up to 180 K, saturating at high temperature. This behavior is consistent with strong impurity scattering at low temperatures and the onset of acoustic phonon scattering at high temperatures, as reported in BP [2,31] and other 2D materials [32,33]. These measurements reveal that the anisotropy ratio r increases linearly as T is decreased, while the anisotropy angle θ_0 remains constant [Fig. 4(d)]. The observed temperature trend of the anisotropy ratio matches the prediction for remote-ionized-impurity scattering (Ref. [34]). Interestingly, Fig. 4(b) shows that the linearly decreasing trend continues even as the experiment crosses over to the high-temperature phonon-limited regime that theoretical studies have yet to investigate.

Examining the gate-voltage dependence in sample B, the mobility along the a and c directions is measured as a function of sheet carrier density from $p = 5.3 \times 10^{11}$ to 4.4×10^{12} cm^{-2}, whereby mobilities in both directions increase with increasing carrier density [Fig. 4(c)] consistent with theoretical prediction [34,35]. The anisotropy ratio itself decreases slightly as density increases, while the angle of anisotropy θ_0 remains constant [Fig. 4(d)]. This observed decrease in anisotropy is consistent with theory for this charged impurity-dominated regime, and the weak dependence indicates that a prevailing number of the impurities are within or close to the BP layer itself [34,35].

In conclusion, the conformal five-contact method employs a conformal mapping method to enable all-electrical determination of the in-plane crystallographic orientation and full resistivity tensor in arbitrarily shaped anisotropic 2D materials. Testing exfoliated BP and MoS_2, both variance minimization and vdP parametric intersection methods are shown to yield consistent results. The utility of the C5C method is demonstrated with temperature and

carrier density dependence of the anisotropy in exfoliated BP. Since the C5C technique can be universally applied without the strict geometric restrictions of other electrical techniques or the material-specific knowledge required for optical spectra interpretation, it can advance fundamental studies and accelerate device development in the rapidly growing field of anisotropic 2D materials.

This research was supported by the Air Force Office of Scientific Research (FA95501510247 and FA05501510377) and the National Science Foundation Materials Research Science and Engineering Center (MRSEC) of Northwestern University (DMR-1121262 and DMR-1720139). This work made use of the EPIC facility of Northwestern University's NUANCE Center, which has received support from the Soft and Hybrid Nanotechnology Experimental (SHyNE) Resource (NSF ECCS-1542205); the MRSEC program (NSF DMR-1121262 and DMR-1720139) at the Materials Research Center; the International Institute for Nanotechnology (IIN); the Keck Foundation; and the State of Illinois, through the IIN.

L. P. and S. A. W. contributed equally to this work.

*Corresponding author.
m-hersam@northwestern.edu
†Corresponding author.
m-grayson@northwestern.edu

[1] H. Liu, A. T. Neal, Z. Zhu, Z. Luo, X. Xu, D. Tomanek, and P. D. Ye, ACS Nano **8**, 4033 (2014).
[2] F. Xia, H. Wang, and Y. Jia, Nat. Commun. **5**, 4458 (2014).
[3] S. Huang *et al.*, ACS Nano **10**, 8964 (2016).
[4] D. A. Chenet, O. B. Aslan, P. Y. Huang, C. Fan, A. M. van der Zande, T. F. Heinz, and J. C. Hone, Nano Lett. **15**, 5667 (2015).
[5] Z. Tian, C. Guo, M. Zhao, R. Li, and J. Xue, ACS Nano **11**, 2219 (2017).
[6] V. Tran, R. Soklaski, Y. Liang, and L. Yang, Phys. Rev. B **89**, 235319 (2014).
[7] J. Qiao, X. Kong, Z. X. Hu, F. Yang, and W. Ji, Nat. Commun. **5**, 4475 (2014).
[8] L. Li *et al.*, Nat. Nanotechnol. **12**, 21 (2017).
[9] L. Li, Y. Yu, G. J. Ye, Q. Ge, X. Ou, H. Wu, D. Feng, X. H. Chen, and Y. Zhang, Nat. Nanotechnol. **9**, 372 (2014).
[10] M. Buscema, D. J. Groenendijk, S. I. Blanter, G. A. Steele, H. S. van der Zant, and A. Castellanos-Gomez, Nano Lett. **14**, 3347 (2014).
[11] H. Yuan *et al.*, Nat. Nanotechnol. **10**, 707 (2015).
[12] X. Wang, A. M. Jones, K. L. Seyler, V. Tran, Y. Jia, H. Zhao, H. Wang, L. Yang, X. Xu, and F. Xia, Nat. Nanotechnol. **10**, 517 (2015).
[13] R. Fei, V. Tran, and L. Yang, Phys. Rev. B **91**, 195319 (2015).
[14] Z. J. Xiang *et al.*, Phys. Rev. Lett. **115**, 186403 (2015).
[15] Y. Du, J. Maassen, W. Wu, Z. Luo, X. Xu, and P. D. Ye, Nano Lett. **16**, 6701 (2016).
[16] X. Liu, C. R. Ryder, S. A. Wells, and M. C. Hersam, Small Methods **1**, 1700143 (2017).
[17] X. Ling *et al.*, Nano Lett. **16**, 2260 (2016).
[18] O. Bierwagen, R. Pomraenke, S. Eilers, and W. T. Masselink, Phys. Rev. B **70**, 165307 (2004).
[19] S. Asmontas, J. Kleiza, and V. Kleiza, Acta Phys. Pol. A **113**, 1559 (2008).
[20] C. A. M. dos Santos, A. de Campos, M. S. da Luz, B. D. White, J. J. Neumeier, B. S. de Lima, and C. Y. Shigue, J. Appl. Phys. **110**, 083703 (2011).
[21] K. A. Borup, K. F. F. Fischer, D. R. Brown, G. J. Snyder, and B. B. Iversen, Phys. Rev. B **92**, 045210 (2015).
[22] G. Qiu, Y. Du, A. Charnas, H. Zhou, S. Jin, Z. Luo, D. Y. Zemlyanov, X. Xu, G. J. Cheng, and P. D. Ye, Nano Lett. **16**, 7364 (2016).
[23] L. J. van der Pauw, Philips Res. Rep. **16**, 187 (1961).
[24] R. Schinzinger and Patricio A. A. Laura, Conformal Mapping Methods and Applications (Dover Publications, Mineola, 2003).
[25] T. A. Driscoll, Schwarz-Christoffel toolbox, http://www.math.udel.edu/~driscoll/SC/.
[26] L. J. Van der Pauw, Philips Res. Rep. **13**, 1 (1958).
[27] Y. Akahama, S. Endo, and S. Narita, J. Phys. Soc. Jpn. **52**, 2148 (1983).
[28] A. Mishchenko, Y. Cao, G. L. Yu, C. R. Woods, R. V. Gorbachev, K. S. Novoselov, A. K. Geim, and L. S. Levitov, Nano Lett. **15**, 6991 (2015).
[29] T. Low, A. S. Rodin, A. Carvalho, Y. Jiang, H. Wang, F. Xia, and A. H. Castro Neto,Phys. Rev. B **90**, 075434 (2014).
[30] J. D. Wood, S. A. Wells, D. Jariwala, K.-S. Chen, E. Cho, V. K. Sangwan, X. Liu, L. J. Lauhon, T. J. Marks, and M. C. Hersam, Nano Lett. **14**, 6964 (2014).
[31] N. Gillgren *et al.*, 2D Mater. **2**, 011001 (2014).
[32] J. H. Chen, C. Jang, S. Adam, M. S. Fuhrer, E. D. Williams, and M. Ishigami, Nat. Phys. **4**, 377 (2008).
[33] B. Radisavljevic and A. Kis, Nat. Mater. **12**, 815 (2013).
[34] Y. Liu and P. P. Ruden, Phys. Rev. B **95**, 165446 (2017).
[35] Y. Liu, T. Low, and P. P. Ruden, Phys. Rev. B **93**, 165402 (2016).

ACS APPLIED MATERIALS & INTERFACES

Letter

www.acsami.org

Thermal Conductivity of ZIF-8 Thin-Film under Ambient Gas Pressure

Boya Cui,[†,‡,§] Cornelius O. Audu,[†,⊥] Yijun Liao,[⊥] SonBinh T. Nguyen,[⊥] Omar K. Farha,[⊥,∥] Joseph T. Hupp,[⊥] and Matthew Grayson*[,‡,§]

[‡]Program in Applied Physics, [§]Department of Electrical Engineering and Computer Science, and [⊥]Department of Chemistry, Northwestern University, Evanston, Illinois 60208, United States

[∥]Department of Chemistry, Faculty of Science, King Abdulaziz University, Jeddah 21589, Saudi Arabia

Supporting Information

ABSTRACT: Thermal conductivity is a crucial parameter for managing exothermal gas adsorption in metal organic frameworks (MOFs), but experimental studies have been limited. In this work, the thermal conductivity of a zeolitic imidazolate framework ZIF-8 was experimentally determined on thin films using the 3ω technique at different partial pressures in perfluorohexane, nitrogen, air, and vacuum ambients at 300 K. In contrast to theoretical prediction, the thermal conductivity $\kappa = 0.326 \pm 0.002$ W/m K was approximately independent of ambient gas species and pressure from atmospheric pressure to vacuum. This work introduces a useful approach for probing MOF thermal conductivity under gas adsorption.

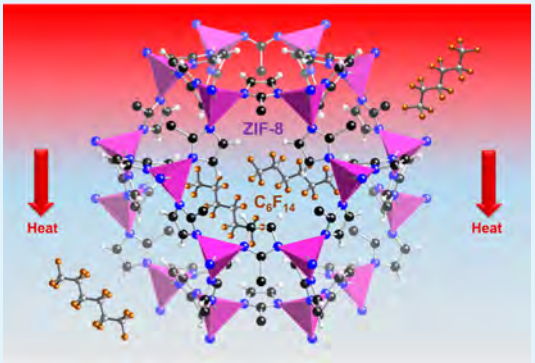

KEYWORDS: *metal organic framework, zeolitic imidazolate framework, ZIF-8, thin film, thermal conductivity, gas storage*

With the growing demand for greener sources of energy as well as the concurrent abundance of natural gas, vehicles fueled by natural gas (NG) in place of petroleum products are an attractive intermediate step toward the realization of a ground transportation fleet that is powered by renewable sources. Vehicles of this kind, however, require large, heavy, and expensive high-pressure fuel tanks in addition to a refill-station infrastructure equipped with high-pressure equipment. To overcome these challenges, researchers have proposed the use of fuel tanks loaded with adsorbed natural gas (ANG), as opposed to liquefied or compressed natural gas, as a strategy for storing large amounts of natural gas in smaller tanks at lower pressure and ambient temperature.[1] However, during the exothermic process of NG adsorption, fuel tanks and their contents undergo a significant temperature rise; depending on the rate of filling and the details tank design as well as sorbent packing and composition temperatures can rise to over 60 °C,[2] a change that could significantly lower a sorbent's gas storage capacity.[3] Similar challenges arise with cryosorption-based storage of molecular hydrogen, the energy source for fuel-cell powered vehicles. Thermal management in these adsorbents is critical for rapid and efficient storage and release of NG or H_2.[4]

Metal−organic frameworks (MOFs), a class of highly tailorable crystalline materials comprised of metal nodes and organic linkers,[5,6] are promising candidates as natural gas adsorbents. To date, there have been few studies on the thermal conductivity of MOFs. The thermal conductivity of the prototypical material, MOF-5, has been obtained from simulations,[7] and confirmed experimentally on large MOF-5 single cubic crystals.[8] Making large single crystals of MOFs can be synthetically challenging, and pelletization of MOF powders for measurements can be fraught with errors due to the presence of large interparticle spaces.[9] A zeolitic imidazolate MOF proposed for hydrogen storage,[10] ZIF-8 was predicted, via molecular dynamics simulations, to have a low thermal conductivity.[11] These studies were only for empty lattices without adsorbed gases, which limits our understanding on how or whether the adsorbed gas affects heat transport within the lattice of the MOFs. Recently, two computational studies predicted opposite trends for the effect of gas adsorption on the MOF thermal conductivity.[12,13] The discrepancies in these studies necessitate reliable experimental studies of thermal conductivity in the presence of gas adsorbents.

Herein, we demonstrate a thin-film based approach for measuring the thermal conductivities of MOFs (Figure 1). This approach has been applied successfully by our group on other thin-film systems[14−16] and avoids the growth challenge of large crystals. As a case study, ZIF-8 was selected because of its known chemical and thermal stability.[17] Thermal conductivity measurements were conducted on ZIF-8 thin films at room temperature in air or nitrogen, or in perfluorohexane (C_6F_{14}) vapor, at variable pressures. Considering the potential hazard of using flammable gases in the electrical circuit setup and in the air, the inert vapor perfluorohexane was used as a substitute for fuel gases such as methane, ethane, and propane. The results

Received: May 11, 2017
Accepted: August 9, 2017
Published: August 9, 2017

DOI: 10.1021/acsami.7b06662
ACS Appl. Mater. Interfaces 2017, 9, 28139−28143

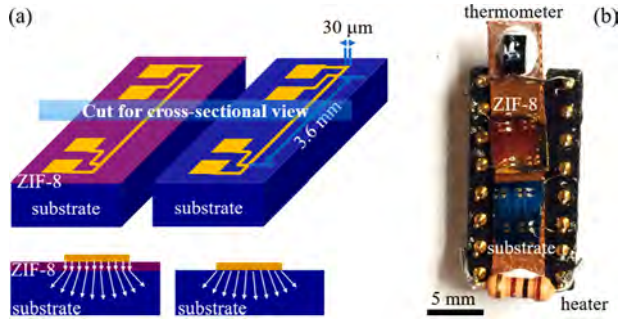

Figure 1. 3ω technique for thin-film thermal conductivity measurement. (a) Schematic illustration for differential measurement of cross-plane thermal conductivity. (b) Real measurement device where the thermometer and resistor heater are used to determine temperature coefficient dR/RdT of the filaments.

offer experimental insights toward the possible effects of guest gas molecules on the thermal conductivity of the ZIF-8 host.

ZIF-8 films were grown with well-controlled thickness on oxide-terminated silicon with an alumina adhesion layer (2 nm AlO_x/300 nm SiO_x/Si) by first quickly immersing the substrate in a beaker containing a freshly prepared methanolic solution of 2-methylimidazole (2-MeIm) and $Zn(NO_3)_2{\cdot}6H_2O$ at room temperature, as has been shown described elsewhere.[18] By replacing the fresh methanolic solution five times every 30 min, a final film of ZIF-8 was obtained with a thickness of t = 300 nm.

Cross-plane thermal conductivity measurements of ZIF-8 thin films were obtained using the differential 3ω method[14,19,20] where the thermal oscillations due to AC Joule heating were compared between samples with and without the film of interest. A gold filament, patterned onto the sample as illustrated in Figure 1a, acted as both heater and thermometer for AC temperature oscillation measurements. From the cross-sectional view in Figure 1a, the heat flow is predominantly in the cross-plane direction, as the filament width (w = 30 μm) is much larger than the film thickness (t = 300 nm). By measuring the difference between the substrate with film and the bare reference substrate (final measurement device in Figure 1b), the cross-plane thermal conductivity can be determined. The four-point metal filament was patterned onto the smooth and uniform film, as illustrated in the cross-sectional scanning electron microscope images (Figure 2a). Following photolithography (sample processing details in the Supporting Information, Section 2), a 100 nm thick gold layer was deposited by thermal evaporation atop an identically patterned 10 nm thick chromium adhesion layer. The filament on the sample looks as shown in Figure 2b after lifting off the photoresist. The sample was then baked in vacuum at 100 °C for 2 h to evacuate the ZIF-8 pores of any solvent molecules introduced during processing. Finally, gold wires were attached with indium onto the contact pads for measurement. Multiple filaments were usually made on each sample, in which sections with the best adhered filament were used for measurement.

X-ray diffraction (XRD, Cu Kα, λ = 1.54 Å) patterns on the thin films confirm the crystallinity of ZIF-8 thin films. The results are shown in Figure 2c, where the inset shows the rescaled peak amplitude for better visibility at $2\theta > 8°$. Except for the peak of Au contacts ($2\theta \approx 38.2°$, from Au [111] contacts) all the peaks are consistent with the simulation, and the highest-intensity peak occurs at $2\theta \approx 7.4°$ indicating the dominant crystal orientation of ZIF-8 [110]. Given the

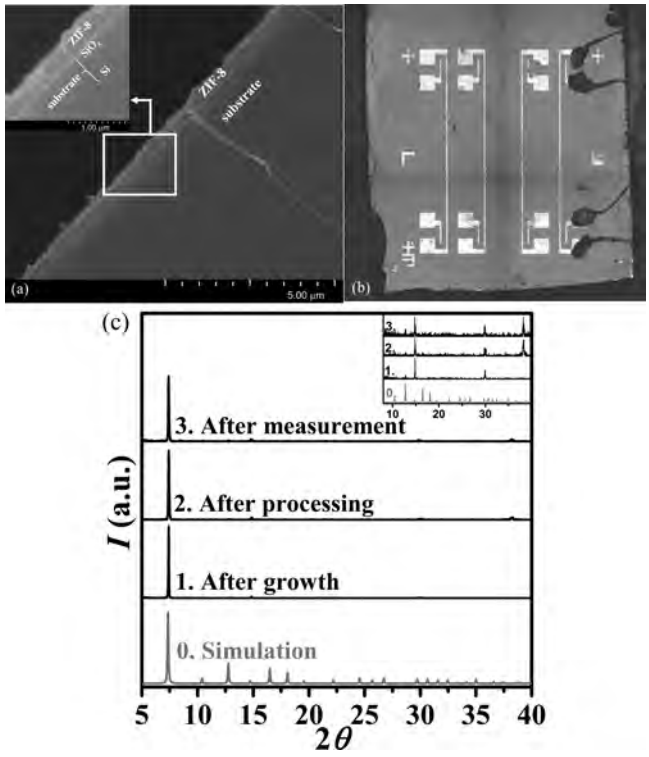

Figure 2. Morphology of ZIF-8 film. (a) Cross-sectional SEM images of as-grown ZIF-8 thin film. (b) Optical profiler image of the processed sample showing the photolithography pattern on ZIF-8 film with measurement contacts, where the filament with the best microscopic morphology is picked for gold-wire contact and final measurement. This image comprises four images stitched together. (c) X-ray diffraction patterns of ZIF-8 thin films during the study cycle (numbered 1−3 in black) compared with simulation result (numbered 0 in gray), where in the inset the peaks at $2\theta > 8°$ are rescaled in amplitude for better visibility. The peak at $2\theta \approx 38.2°$ comes from the gold contacts after photolithographic processing.

possibility of slow hydrothermal degradation[21,22] of ZIF-8, XRD measurements were conducted multiple times throughout this study over the course of several days (i.e., after synthesis, between processing steps, and after measurements), and it was ascertained that the crystallinity was maintained during the thermal conductivity study. A more complete time series of XRD results is shown in the Supporting Information, Section 3.

The thermal conductivity (κ) of ZIF-8 thin film was first measured in air at room temperature shown in Figure 3 (see the Supporting Information, Section 5, for κ derivation details). The in-air thermal conductivity is reproducible among three different thin film samples ($\kappa_{sample\ 1}$ = 0.33 W/(m K), $\kappa_{sample\ 2}$ = 0.29, and $\kappa_{sample\ 3}$ = 0.23 W/(m K)) and slightly higher than the predicted ZIF-8 value (κ = 0.165 W/(m K)),[11] confirming the expected order of magnitude. The error range for the 3 conductivity values from the three samples is representative of the differences from sample to sample, which were made/prepared from different batches and/or on different days, though it is possible that this variability could be due to the relative amounts/positions of grain boundaries and defects in polycrystalline films.

The effect of adsorbed gas analytes was then studied with the benefit of our controlled gas chamber setup. Thermal conductivity of the ZIF-8 film was observed to change by less than a percent in the presence and absence of different gas

DOI: 10.1021/acsami.7b06662
ACS Appl. Mater. Interfaces 2017, 9, 28139−28143

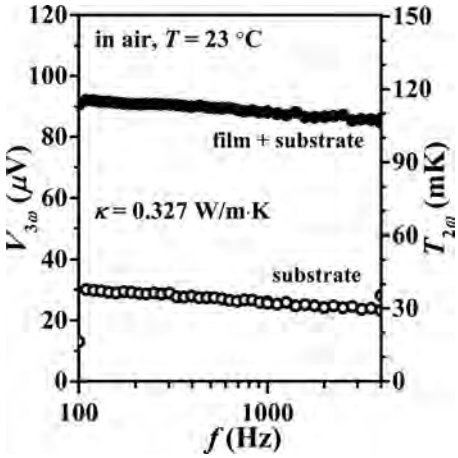

Figure 3. 3ω data of ZIF-8 thin film in air at room temperature.

analytes. The thermal conductivity results of ZIF-8 films are shown in Figure 4(a) for C_6F_{14} (blue) and N_2 (gray) environments as compared to ambient air (P_{gauge} = 1 atm) and house vacuum (P_{gauge} = 0.02 atm) measurements. As shown for the C_6F_{14} ambient pressure (Figure 4a, blue) the lowest thermal conductivity occurs in vacuum. As the gas pressure of C_6F_{14} increases to its vapor pressure the thermal conductivity of the ZIF-8 thin film only slightly increases by ~1% despite appreciable adsorption of C_6F_{14} to the MOF surface at these relative pressures as indicated by a C_6F_{14} isotherm. (See the Supporting Information, Section 4, for isotherm results.) Interestingly, when the thin films were re-exposed to nitrogen atmosphere (gray) from vacuum, the thermal conductivities exhibited a similar trend to the films that were exposed to perfluorohexane vapor (P_{gauge} = 0.28 atm, blue). Unlike C_6F_{14}, N_2 adsorption is rather negligible at room temperature (2.5 cm^3/g; ~0.6% total capacity). The observed shallow linear N_2 uptake (Supporting Information, Section 4) is consistent with the sorbate's miniscule molecular polarizability and, therefore, weak van der Waals interaction with the framework. (In contrast, at low temperature, significant physisorption of N_2 is possible. For a bulk ZIF-8 sample prepared in our lab, N_2 uptake at T = 77 K culminates in pore saturation at 437 cm^3/g. See the Supporting Information for isotherm.)

The pressure study can be modeled equivalently in terms of number of molecules per ZIF-8 unit cell. Figure 4b converts the pressure-dependent thermal conductivity result in Figure 4a to the molecule density scale using the isotherm results in Section 4 of the Supporting Information. In our measurement results (blue), C_6F_{14} has an approximate density of D = 1.4 C_6F_{14} molecules per ZIF-8 pore (or 2.8 per unit cell) as estimated from the corresponding isotherm data in the Supporting Information. However, this saturated amount of C_6F_{14} inside ZIF-8 seems to neither hinder heat transfer by phonon scattering with host lattice, nor enhance the thermal transport through gas molecules in voids, unlike the predicted decreasing[12] or increasing[13] trend in prior simulations on other MOFs with different adsorbed gases (black symbols and gray shaded guides to the eye in Figure 4b). While surprising, it is possible that the proposed[13] enhancement in lattice thermal conductivity due to the additional heat transfer channels provided from the adsorbed gas molecules, may be minimal for C_6F_{14}, which has a very low thermal conductivity (κ_{liquid} = 0.056 W/m·K)[23] in comparison to other fuel gases such as hydrogen[24] (κ_{gas} = 0.18 W/m·K). Note that even for hydrogen, the thermal conductivity of MOF with adsorbed hydrogen does not show significant increase below a certain uptake threshold (D = 4 molecules per unit cell) according to prior simulations.[12,13] On the other hand, in comparison to CH_4, the heavier gas molecule C_6F_{14} is more likely to induce phonon scattering effects than CH_4. However, in contrast to predictions in the Babei et al.'s simulations, any scattering effects from C_6F_{14} do not seem to affect the thermal conductivity of ZIF-8.

In conclusion, the thermal conductivity of ZIF-8 was measured experimentally for the first time with thin film studies. Additionally, we demonstrated a way to conduct in situ measurements at room temperature under different gases and pressures. The results show reproducibility among samples, and vacuum thermal conductivity compare favorably to prior simulation studies on MOFs. From the series of gas adsorption tests investigated, ZIF-8 thin-film thermal conductivity is slightly lower in vacuum than that in air by about 1%, but generally independent of the presence of gas molecules

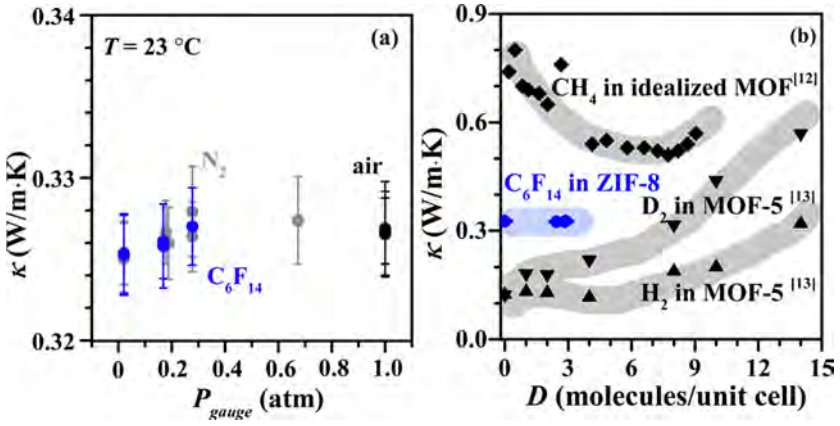

Figure 4. (a) Measured thermal conductivity of ZIF-8 thin film during the gas tests in N_2 and C_6F_{14}. The error bars are derived from the statistical standard deviation of 3ω voltage at various frequencies between f = 100 and 4000 Hz. The measurements were taken at least 3 min after stabilizing at each partial pressure to make sure that the adsorption amount was steady (see the Supporting Information, Section 4, for the figure of C_6F_{14} uptake kinetics in ZIF-8). (b) Comparison of the experimental pressure-dependent thermal conductivity of this work (blue) with prior simulation[12,13] (black), with guides to the eye (gray) to illustrate trends.

DOI: 10.1021/acsami.7b06662
ACS Appl. Mater. Interfaces 2017, 9, 28139−28143

regardless of the quantity adsorbed by the MOF up to atmospheric pressure. Although the thermal conductivity in ZIF-8 is relatively unaffected by adsorbed gases and vapors, it is possible that such an effect might be more pronounced at higher pressures and with more thermally conductive sorbates. This technique demonstrates a viable pathway for obtaining MOF thermal conductivities to probe these effects in future studies.

■ ASSOCIATED CONTENT

Supporting Information

The Supporting Information is available free of charge on the ACS Publications website at DOI: 10.1021/acsami.7b06662.

Thin-film characterization: XRD and SEM; thin-film processing; X-ray diffraction profiles of thin-film crystallinity; preparation and gas sorption analysis of ZIF-8; 3ω measurement setup and thermal conductivity derivation (PDF)

■ AUTHOR INFORMATION

Corresponding Author

*E-mail: mgrayson@eecs.northwestern.edu. Phone: +1 (847) 491-8137.

ORCID

Boya Cui: 0000-0001-7318-5761
SonBinh T. Nguyen: 0000-0002-6977-3445
Omar K. Farha: 0000-0002-9904-9845
Joseph T. Hupp: 0000-0003-3982-9812

Author Contributions

†B.C. and C.O.A. contributed equally to this work. The manuscript was written through contributions of all authors. All authors have given approval to the final version of the manuscript.

Notes

The authors declare no competing financial interest.

■ ACKNOWLEDGMENTS

This work was supported by AFOSR FA9550-15-1-0247, NSF CCF-1422489 and made use of Northwestern University Micro/Nano Fabrication Facility (NUFAB) and the J.B. Cohen X-ray Diffraction Facility, and the EPIC facility of Northwestern University's NUANCE Center, which are supported by the MRSEC program of the National Science Foundation (DMR-1121262) at the Materials Research Center of Northwestern University, the International Institute for Nanotechnology (IIN), the Keck Foundation, and the State of Illinois, and the Soft and Hybrid Nanotechnology Experimental (SHyNE) Resource (NSF NNCI-1542205). C.O.A. is an NSF Graduate Research Fellow (Grant DGE-1324585). J.T.H. and O.K.F. acknowledge support from the U.S. Department of Energy, Office of Science (Grant DE-FG02-08ER15967). S.T.N. acknowledges support from DTRA (HDTRA1-14-1-0014).

■ ABBREVIATIONS

MOF, metal organic framework
ZIF, zeolitic imidazolate framework
NG, natural gas
ANG, adsorbed natural gas
XRD, X-ray diffraction
SEM, scanning electron microscope

■ REFERENCES

(1) Simon, C. M.; Kim, J.; Gomez-Gualdron, D. A.; Camp, J. S.; Chung, Y. G.; Martin, R. L.; Mercado, R.; Deem, M. W.; Gunter, D.; Haranczyk, M.; Sholl, D. S.; Snurr, R. Q.; Smit, B. The Materials Genome in Action: Identifying the Performance Limits for Methane Storage. *Energy Environ. Sci.* **2015**, *8* (4), 1190−1199.

(2) Sáez, A.; Toledo, M. Thermal Effect of the Adsorption Heat on an Adsorbed Natural Gas Storage and Transportation Systems. *Appl. Therm. Eng.* **2009**, *29* (13), 2617−2623.

(3) Schmitz, B.; Müller, U.; Trukhan, N.; Schubert, M.; Férey, G.; Hirscher, M. Heat of Adsorption for Hydrogen in Microporous High-Surface-Area Materials. *ChemPhysChem* **2008**, *9* (15), 2181−2184.

(4) Zhang, J.; Ramachandran, P. V.; Gore, J. P.; Mudawar, I.; Fisher, T. S. A Review of Heat Transfer Issues in Hydrogen Storage Technologies. *J. Heat Transfer* **2005**, *127* (12), 1391−1399.

(5) Li, H.; Eddaoudi, M.; O'Keeffe, M.; Yaghi, O. M. Design and Synthesis of an Exceptionally Stable and Highly Porous Metal-Organic Framework. *Nature* **1999**, *402* (6759), 276−279.

(6) Suh, M. P.; Park, H. J.; Prasad, T. K.; Lim, D.-W. Hydrogen Storage in Metal-Organic Frameworks. *Chem. Rev.* **2012**, *112* (2), 782−835.

(7) Huang, B. L.; McGaughey, A. J. H.; Kaviany, M. Thermal Conductivity of Metal-Organic Framework 5 (MOF-5): Part I. Molecular Dynamics Smulations. *Int. J. Heat Mass Transfer* **2007**, *50* (3), 393−404.

(8) Huang, B. L.; Ni, Z.; Millward, A.; McGaughey, A. J. H.; Uher, C.; Kaviany, M.; Yaghi, O. Thermal Conductivity of a Metal-Organic Framework (MOF-5): Part II. Measurement. *Int. J. Heat Mass Transfer* **2007**, *50* (3), 405−411.

(9) Purewal, J.; Liu, D.; Sudik, A.; Veenstra, M.; Yang, J.; Maurer, S.; Muller, U.; Siegel, D. J. Improved Hydrogen Storage and Thermal Conductivity in High-Density MOF-5 Composites. *J. Phys. Chem. C* **2012**, *116* (38), 20199−20212.

(10) Wu, H.; Zhou, W.; Yildirim, T. Hydrogen Storage in a Prototypical Zeolitic Imidazolate Framework-8. *J. Am. Chem. Soc.* **2007**, *129* (17), 5314−5315.

(11) Zhang, X.; Jiang, J. Thermal Conductivity of Zeolitic Imidazolate Framework-8: A Molecular Simulation Study. *J. Phys. Chem. C* **2013**, *117* (36), 18441−18447.

(12) Babaei, H.; Wilmer, C. E. Mechanisms of Heat Transfer in Porous Crystals Containing Adsorbed Gases: Applications to Metal-Organic Frameworks. *Phys. Rev. Lett.* **2016**, *116* (2), 025902.

(13) Han, L.; Budge, M.; Alex Greaney, P. Relationship between Thermal Conductivity and Framework Architecture in MOF-5. *Comput. Mater. Sci.* **2014**, *94*, 292−297.

(14) Cui, B.; Zeng, L.; Keane, D.; Bedzyk, M. J.; Buchholz, D. B.; Chang, R. P. H.; Yu, X.; Smith, J.; Marks, T. J.; Xia, Y.; Facchetti, A. F.; Medvedeva, J. E.; Grayson, M. Thermal Conductivity Comparison of Indium Gallium Zinc Oxide Thin Films: Dependence on Temperature, Crystallinity, and Porosity. *J. Phys. Chem. C* **2016**, *120* (14), 7467−7475.

(15) Cui, B.; Buchholz, D. B.; Zeng, L.; Bedzyk, M.; Chang, R. P. H.; Grayson, M. Long-Term Room Temperature Instability in Thermal Conductivity of InGaZnO Thin Films. *MRS Adv.* **2016**, *1* (22), 1631−1636.

(16) Zhou, C.; Cui, B.; Vurgaftman, I.; Canedy, C. L.; Kim, C. S.; Kim, M.; Bewley, W. W.; Merritt, C. D.; Abell, J.; Meyer, J. R.; Grayson, M. Thermal Conductivity Tensors of the Cladding and Active Layers of Interband Cascade Lasers. *Appl. Phys. Lett.* **2014**, *105* (26), 261905.

(17) Park, K. S.; Ni, Z.; Cote, A. P.; Choi, J. Y.; Huang, R.; Uribe-romo, F. J.; Chae, H. K.; O'Keeffe, M.; Yaghi, O. M. Exceptional Chemical and Thermal Stability of Zeolitic Imidazolate Frameworks. *Proc. Natl. Acad. Sci. U. S. A.* **2006**, *103* (27), 10186−10191.

(18) Lu, G.; Hupp, J. T. Metal Organic Franeworks as Sensors: A ZIF-8 Based Fabry-Pérot Device as a Selective Sensor for Chemical Vapors and Gases. *J. Am. Chem. Soc.* **2010**, *132* (23), 7832−7833.

(19) Cahill, D. G. Thermal Conductivity Measurement from 30 to 750 K: 3w Method. *Rev. Sci. Instrum.* **1990**, *61* (2), 802−808.

DOI: 10.1021/acsami.7b06662
ACS Appl. Mater. Interfaces 2017, 9, 28139−28143

(20) Cahill, D. G.; Katiyar, M.; Abelson, J. R. Thermal Conductivity of a-Si:H Thin Films. *Phys. Rev. B: Condens. Matter Mater. Phys.* **1994**, *50* (9), 6077−6082.
(21) Zhang, H.; Liu, D.; Yao, Y.; Zhang, B.; Lin, Y. S. Stability of ZIF-8 Membranes and Crystalline Powders in Water at Room Temperature. *J. Membr. Sci.* **2015**, *485*, 103−111.
(22) Liu, X.; Li, Y.; Ban, Y.; Peng, Y.; Jin, H.; Bux, H.; Xu, L.; Caro, J.; Yang, W. Improvement of Hydrothermal Stability of Zeolitic Imidazolate Frameworks. *Chem. Commun.* **2013**, *49* (80), 9140−9142.
(23) Yang, B.; Han, Z. H. Thermal Conductivity Enhancement in Water-in-FC72 Nanoemulsion Fluids. *Appl. Phys. Lett.* **2006**, *88*, 261914.
(24) Saxena, S. C.; Saxena, V. K. Thermal Conductivity Data for Hydrogen and Deuterium in the Range 100−1100 °C. *J. Phys. A: Gen. Phys.* **1970**, *3* (3), 309−320.

DOI: 10.1021/acsami.7b06662
ACS Appl. Mater. Interfaces 2017, 9, 28139−28143

Journal of ELECTRONIC MATERIALS
https://doi.org/10.1007/s11664-018-6431-2

U.S. WORKSHOP ON PHYSICS AND CHEMISTRY OF II-VI MATERIALS 2017

Analysis of Carrier Transport in *n*-Type $Hg_{1-x}Cd_xTe$ with Ultra-Low Doping Concentration

JUSTIN EASLEY,[1,2,5] ERDEM ARKUN,[3] BOYA CUI,[4] MICHAEL CARMODY,[3] LINTAO PENG,[4] MATTHEW GRAYSON,[4] and JAMIE PHILLIPS[1]

1.—Department of Electrical Engineering and Computer Science, University of Michigan, Ann Arbor, MI 48109, USA. 2.—Applied Physics Program, University of Michigan, Ann Arbor, MI 48109, USA. 3.—Teledyne Imaging Sensors, Camarillo, CA 93012, USA. 4.—Department of Electrical Engineering and Computer Science, Northwestern University, Evanston, IL 60208, USA. 5.—e-mail: jleasley@umich.edu

Mercury cadmium telluride (HgCdTe, or MCT) with low *n*-type indium doping concentration offers a means for obtaining high performance infrared detectors. Characterizing carrier transport in materials with ultra low doping ($N_D = 10^{14}$ cm^{-3} and lower), and multi-layer material structures designed for infrared detector devices, is particularly challenging using traditional methods. In this work, Hall effect measurements with a swept *B*-field were used in conjunction with a multi-carrier fitting procedure and Fourier-domain mobility spectrum analysis to analyze multi-layered MCT samples. Low temperature measurements (77 K) were able to identify multiple carrier species, including an epitaxial layer ($x = 0.2195$) with *n*-type carrier concentration of $n = 1 \times 10^{14}$ cm^{-3} and electron mobility of $\mu = 280000$ cm^2/Vs. The extracted electron mobility matches or exceeds prior empirical models for MCT, illustrating the outstanding material quality achievable using current epitaxial growth methods, and motivating further study to revisit previously published material parameters for MCT carrier transport. The high material quality is further demonstrated via observation of the quantum Hall effect at low temperature (5 K and below).

Key words: Mercury cadmium telluride, HgCdTe, magnetotransport, multi-carrier fitting, low doping, Fourier-domain mobility spectrum analysis

INTRODUCTION

Mercury cadmium telluride (HgCdTe, or MCT) is an important material used in high-performance infrared (IR) detectors and devices.[1] The bandgap of MCT ranges from 0 eV to 1.5 eV, making it ideal for optical absorption at a wide range of IR wavelengths. A significant challenge for IR detection, especially at longer wavelengths and smaller bandgap energy, is the requirement to operate at cryogenic temperatures to suppress thermally generated dark current. For long wavelength IR (LWIR, 8–14 μm) detection in *n*-type MCT, the primary source of dark current is Auger 1 generation and recombination.[2] Achieving low carrier density in the absorber layer in a detector structure is therefore critical for minimizing Auger processes that limit dark current, which may be accomplished using ultra low doping (10^{14} cm^{-3} or lower) in both conventional *p*–*n* junction architectures and designs using a non-equilibrium operation to achieve Auger suppression.[3–5] In these detector structures, it is desirable to define absorber layers ($n \sim 10^{13}/10^{14}$ cm^{-3}) with doping concentration that is orders of magnitude lower than the surrounding layers in the device ($n \sim 10^{15}$ cm^{-3} or higher). The ability to

(Received December 30, 2017; accepted June 5, 2018)

Published online: 17 July 2018

measure and interpret carrier transport properties in multi-layer MCT structures containing ultra-low doping is important in the design and interpretation of advanced detector devices.[6]

The ability to extract carrier information from complex structures using the Hall effect method with swept B-field and the multi-carrier fit (MCF) procedure has been previously demonstrated.[7] The drawback to this procedure is that it requires an assumption of the number and type of carrier species present in the device. The concentration of carriers was estimated from a bulk-doping assumption of the layer structure of the device. The possibility of any surface/interface carriers or layers with multiple carriers was not considered. Mobility spectrum analysis has been previously demonstrated as an effective analysis technique in measuring multiple carrier species in MCT.[8–10] The mobility spectrum analysis technique was originally developed by Beck and Anderson,[11] who were able to calculate an envelope function that gave an upper bound to the mobility spectrum. Updated algorithms (such as i-QMSA) were developed that fit data using an iterative method designed to minimize overall error.[12,13] In this work, Fourier-domain mobility spectrum analysis (FMSA), developed by Cui et al. at Northwestern University,[14,15] was used. FMSA offers advantages over traditional QMSA by converging in fewer iteration steps with simpler code, more accurate linewidths and lower computational costs. This technique, used in conjunction with MCF, gives information about the carrier species, allowing for a more detailed understanding of the transport dynamics in complex material structures.

EXPERIMENT

High quality MCT layers were grown by molecular beam epitaxy (MBE) at Teledyne Imaging Sensors using the standard double-layer planar heterojunction (DLPH) structure depicted in Fig. 1. Epitaxial layers were doped in situ n-type with indium, followed by a Hg vapor anneal post-growth to remove Hg vacancies. Hall bar devices were fabricated using photolithography, wet etching, and Ti/Au electrical contacts. Hall effect parameters (longitudinal resistivity and Hall voltage) were measured using two systems: the Dynacool Physical Property Measurement System (PPMS) at the University of Michigan, and the Cryogenics Limited Cryogen-Free Measurement System (CFMS) at Northwestern University. Between the two systems, variable magnetic-field measurements were conducted at fields ranging from B = 0–16 T, and temperature measurements range from T = 500 mK to 300 K.

Conductivity tensor components were calculated by first measuring values for resistivity and Hall voltage. These were converted into sheet components (sheet resistance, R_S, and sheet Hall coefficient, R_H) using the sample thickness, d. Expressions for the conductivity tensor are given by Eqs. 1 and 2

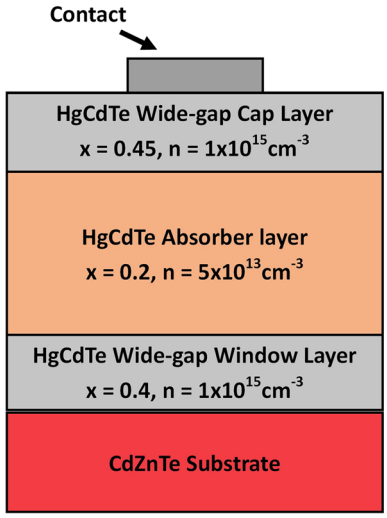

Fig. 1. Double layer planar heterojunction (DLPH) device structure. The cap layer was etched away in these experiments.

$$\sigma_{xx}(B) = \frac{R_S}{B^2R_H^2 + R_S^2}, \tag{1}$$

$$\sigma_{xy}(B) = \frac{BR_H}{B^2R_H^2 + R_S^2}, \tag{2}$$

where B is the magnetic field.

Multiple analysis techniques were employed to fit the conductivity tensor components and extract carrier transport information. Fourier-domain mobility spectrum analysis (FMSA) was used in conjunction with the multi-carrier fit (MCF) procedure to get a more complete picture of relevant carrier species. FMSA iterates to fit the conductivity tensor components to Eqs. 3 and 4

$$\sigma_{xx}(B_j) = \sum_i^m A_{xx}^{ij}\left[s_p(\mu_i) + s_n(\mu_i)\right], \tag{3}$$

$$\sigma_{xy}(B_j) = \sum_i^m A_{xy}^{ij}\left[s_p(\mu_i) - s_n(\mu_i)\right], \tag{4}$$

where B_j are the discrete magnetic field values, and μ_i are a series of mobility values used to create a mobility spectrum. The values A^{ij}, s_p, and s_n are given by Eqs. 5, 6, 7, and 8

$$A_{xx}^{ij} = \frac{1}{1 + (\mu_i B_j)^2}, \tag{5}$$

$$A_{xy}^{ij} = \frac{\mu_i B_j}{1 + (\mu_i B_j)^2}, \tag{6}$$

$$s_p(\mu_i) = p_i q \mu_i, \tag{7}$$

$$s_n(\mu_i) = n_i q \mu_i, \tag{8}$$

where p_i and n_i are electron and hole carrier densities at a given mobility value. The fitting procedure is outlined in detail in Ref. 14. The analysis results in a mobility spectrum with peaks in either s_p, or s_n that correspond to carrier species. MSA is robust in the fact that no prior knowledge of carrier species is needed for the analysis, and no trial function is required *a priori*.

The peaks in the mobility spectrum from FMSA are then used as an initial guess in the MCF procedure. MCF performs a least squares regression to Eqs. 9 and 10, extracting n_s (sheet carrier density) and μ (mobility) for the number of carriers provided. S_i is $\pm$ 1, for holes and electrons, and the traditional carrier density, n, is calculated by dividing the sheet density by the layer thickness, t.

$$\sigma_{xx}(B) = \sum_{i=1}^{m} \frac{q\mu_i}{1 + (\mu_i B)^2} \tag{9}$$

$$\sigma_{xy}(B) = \sum_{i=1}^{m} S_i \frac{q n_{s,i} \mu_i^2 B}{1 + (\mu_i B)^2} \tag{10}$$

RESULTS

Magnetotransport measurements were conducted on samples with two layers present: a buffer layer with a higher doping n-type level (target doping $N_D = 10^{15}$ cm^{-3}), and a low-doped n-type absorber layer (target doping $N_D = 5 \times 10^{13}$ cm^{-3}). FMSA was then applied to fit the measured σ_{xx} and σ_{xy} at 77 K (Fig. 2), where the computed mobility spectrum is displayed in Fig. 3. Conductivity peaks corresponding to the electron conduction in the buffer and absorber layers are observed as expected, while some contribution from hole conduction is also observed.

Several artifacts are evident in Fig. 3 that deserve explicit mention. A large peak is visible at 10^6 cm^2/Vs, present in all analyses regardless of temperature. This peak is considered to be a boundary-condition effect of the FMSA technique. Smaller electron peaks are observed at mobilities below 10^3 and around 10^5 cm^2/Vs, however all peaks below 10^{-6} S are ignored as they are orders of magnitude smaller than the primary carriers. There is also a low density/low mobility electron species visible as well, but due to its low mobility it does not contribute significantly to the overall conduction, nor is it visible at higher temperatures, and it will be disregarded for the MCF fits.

The carrier information gained from the FMSA analysis is used as an initial guess for the MCF

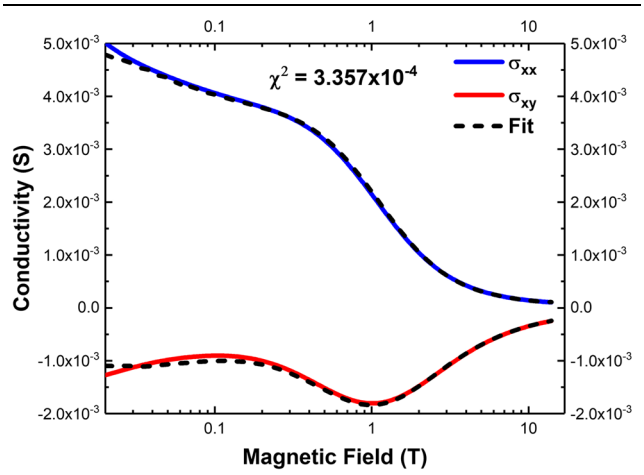

Fig. 2. Conductivity tensor versus magnetic field for a low doped sample. Dashed lines show fit from FMSA. The error is expressed in the inset as χ^2.

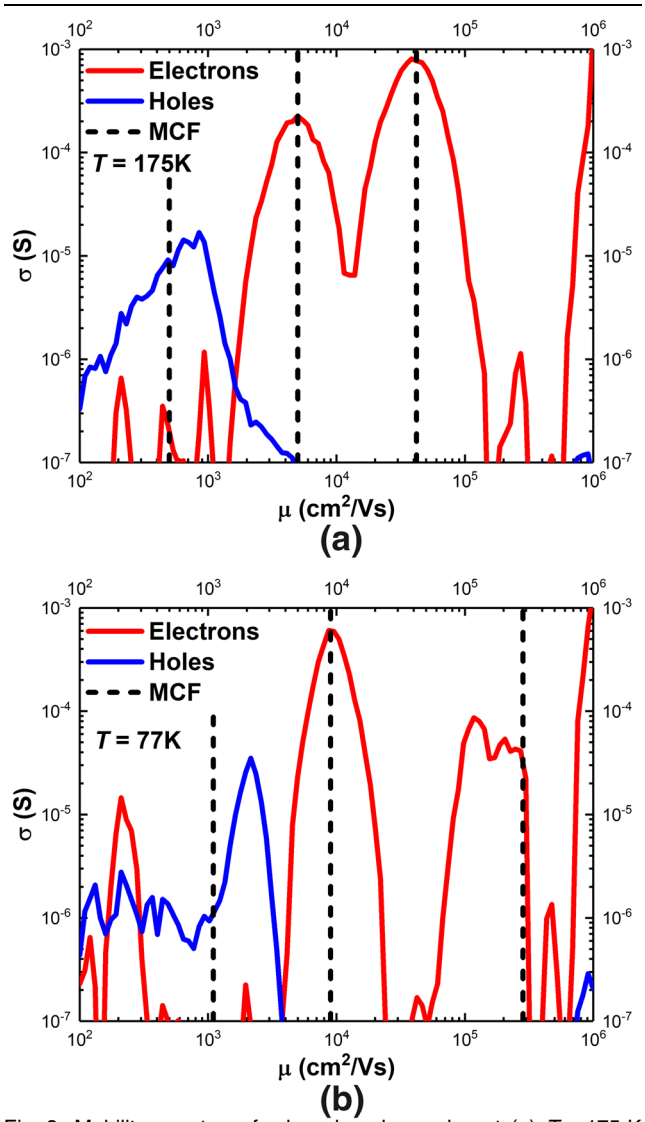

Fig. 3. Mobility spectrum for low doped samples at (a) T = 175 K and (b) T = 77 K. Dashed lines indicate mobility values extracted from the multi-carrier fitting procedure.

procedure. The results of that analysis are displayed in Table I. Carriers are identified by comparing 77 K concentrations with extrinsic doping densities, then correlating the temperature dependence of each species. The electron densities are displayed as volume densities, assuming uniform carrier distribution over the corresponding layer thickness. Layer thickness information is initially gathered from growth data and verified using FTIR. The hole density is reported as a sheet density, as there is uncertainty in the spatial location, or whether the holes are contained uniformly in a single layer. The temperature dependence of the carrier density and mobility are shown in Fig. 4a and b, respectively. The carrier density closely follows the intrinsic carrier concentration at 80 K and above, and approaches the extrinsic doping level (4×10^{13}) asymptotically for temperatures below 80 K.

The mobility values were compared against two mobility models, displayed in Fig. 5. The first is an empirical model developed by Rosbeck[16] (Eq. 11),

$$\mu = \frac{9 \times 10^8 \left(\frac{0.2}{x}\right)^{7.5}}{Z^{2\left(\frac{0.2}{x}\right)^{0.6}}} \text{ cm}^2/\text{Vs}, \tag{11}$$

$$Z = T \quad \text{if } T > 50\,\text{K}, \tag{12}$$

$$Z = \frac{1.18 \times 10^5}{2600 - |T - 35|^{2.07}} \quad \text{if } T < 50\,\text{K}, \tag{13}$$

where x is the cadmium fraction. The layers used to develop the first model are bulk grown via liquid phase epitaxy (LPE) with a variety of compositions, and all have a doping level of approximately $N_D = 10^{15}$ cm^{-3}. The measured mobility on the current layers was higher than this empirical model, so a comparison was also made between a first principles model based on scattering theory.[17] At 77 K, the primary scattering mechanism is polar optical phonon scattering (Eq. 14),

$$\mu_{POP} = \left(\frac{k_B\theta}{2m^*}\right)^{\frac{1}{2}} [\exp((\gamma_0) - 1]/F_0, \tag{14}$$

where $k_B\theta = 0.0176$ eV is the optical phonon energy, $\gamma_0 = \theta/T$, and $F_0 = [\varepsilon_{HF}^{-1} - \varepsilon_s^{-1}]\ m^* q k_B \theta \pi / \varepsilon_0 h^2$. Here, ε_{HF} is the high frequency relative dielectric constant, and ε_s is the static relative dielectric constant. Other relevant scattering mechanisms include alloy, ionized impurity, and neutral impurity scattering. Mobility values at 77 K (measured—2.8×10^5 cm^2/Vs) are shown to be approaching the predictions of this model (5.3×10^5 cm^2/Vs), indicating very high-quality material.

To further study material quality, Hall-effect measurements were conducted at very low temperatures (down to $T = 500$ mK) on a similar, low-

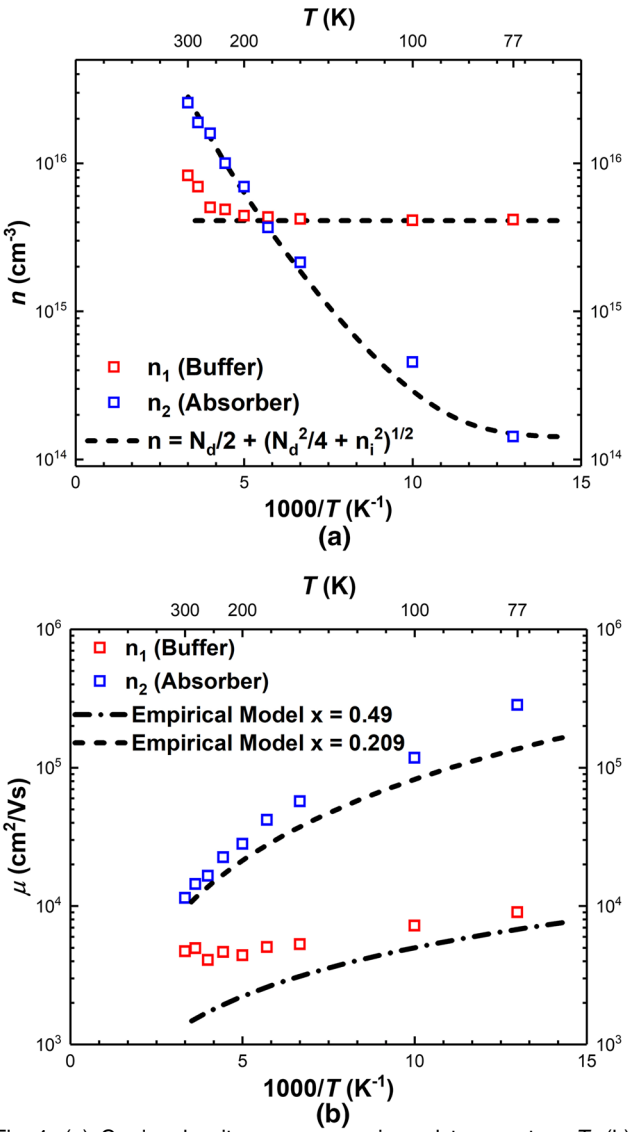

Fig. 4. (a) Carrier density n versus reciprocal temperature T. (b) Mobility μ versus reciprocal temperature T.

Table I. Carrier density and mobility values extracted using the Van der Pauw technique (vdP), MCF, and FMSA

77 K	n_1 (cm^{-3})	μ_1 (cm^2/Vs)	n_2 (cm^{-3})	μ_2 (cm^2/Vs)	p (cm^{-2})	μ_p (cm^2/Vs)
vdP	2×10^{15}	23400	n/a	n/a	n/a	n/a
FMSA	4×10^{15}	11000	1×10^{14}	150000	4.7×10^{11}	1800
FMSA + MCF	4.17×10^{15}	9000	1.43×10^{14}	284000	1.06×10^{12}	1100

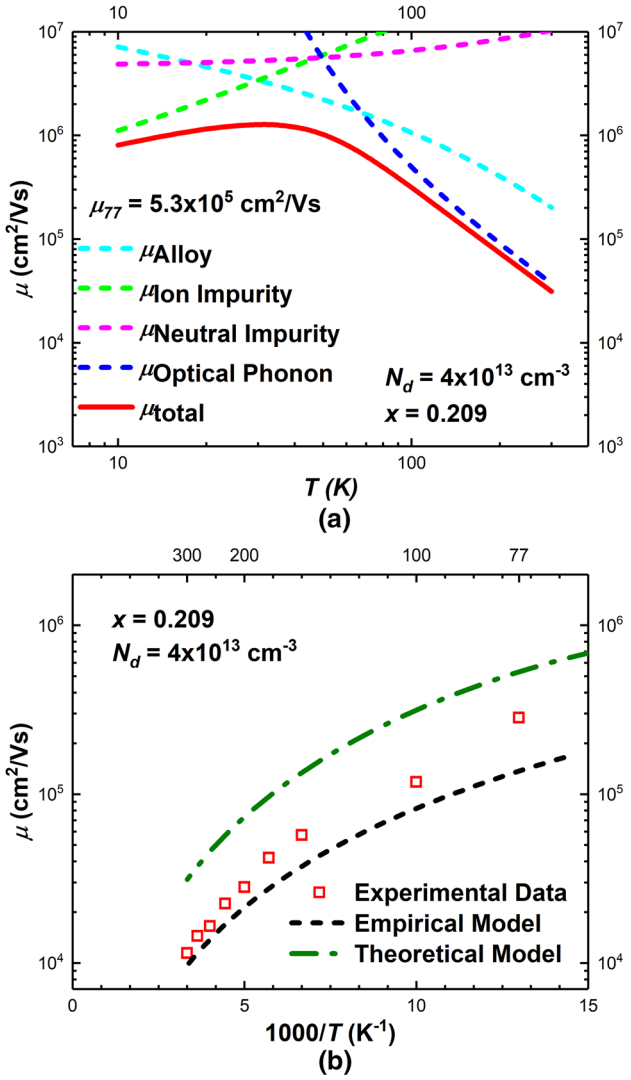

Fig. 5. (a) Theoretical electron mobility values due to scattering from polar optical phonons, alloy, and ionized impurities. (b) Comparison of measured mobility to empirical and theoretical models.

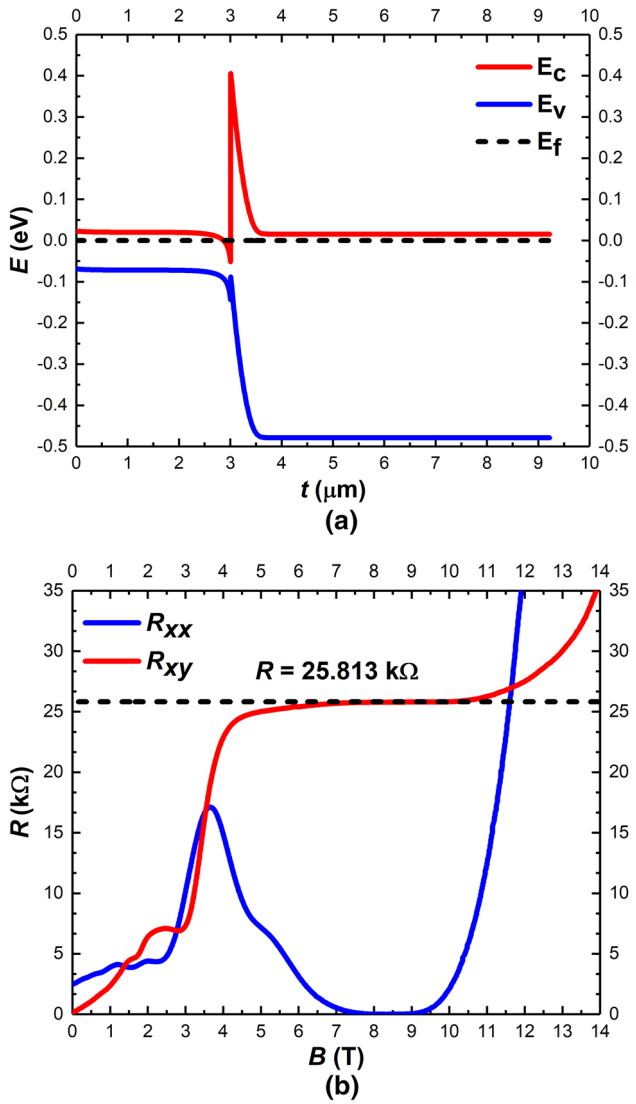

Fig. 6. (a) Calculated band structure at interface of buffer and absorber layers. (b) Measured resistance vs magnetic field at T = 500 mK.

doped ($N_D = 4 \times 10^{13}$ cm^{-3}, similar buffer and absorber layer thickness and composition) MCT sample. A calculated band diagram for the material structure is displayed in Fig. 6a, indicating electron confinement at the absorber/buffer interface. In the resulting two-dimensional electron gas (2DEG), the allowed energy levels for electrons are quantized in a magnetic field, indicating only certain allowed Hall resistance values. These allowed values correspond to plateaus in the Hall resistivity as a function of magnetic field, where the Hall resistance is quantized according to $\rho_{xy} = h/\nu e^2$ indexed by the Landau level, ν.[18] Measurements demonstrate quantization of the Hall resistivity indicative of the quantum Hall effect (Fig. 6b). This quantization was clearly observable at temperatures as high at 5 K, and although no explicit quantum well structure was intended and no gate voltage was applied, quantum confinement is inherent in the structure as calculated at the interfaces in Fig. 6a. The onset of quantum oscillations already around B = 1 T in Fig. 6b indicates a mobility of order at least $\mu \sim 1/B$ = 1 m^2/Vs = 10000 cm^2/Vs, and illustrates the excellent material quality and high crystalline integrity of the interfaces, as defects and disorder at the interface would degrade the mobility.

CONCLUSION

The carrier transport properties of MCT epilayers were extracted using Hall effect B sweeps, in conjunction with Fourier-domain mobility spectrum analysis and the multi-carrier fitting procedure. Low doping levels around $N_D = 10^{14}$ cm^{-3} are displayed, as well as carrier mobility values that exceed previous empirical calculations. Further study of carrier transport mechanisms in MCT

may be necessary to better understand these extracted mobilities. At very low temperatures, the quantum Hall effect is observed, indicating high quality material, and low interface defect densities. Future work will seek to correlate lower doping levels and higher mobility with other material parameters such as minority carrier lifetimes and diffusion length, and potentially use these techniques for analyzing *p*-type MCT.

ACKNOWLEDGEMENTS

The authors would like to thank Professor Lu Li for assistance with the PPMS Dynacool measurement system, Professor Cagliyan Kurdak for assistance with the quantum Hall measurements, and the National Science Foundation Major Research Instrumentation Award No. DMR-1428226 (supporting the equipment for electrical transport characterization). In addition, this work was supported by the Air Force Office of Scientific Research Awards FA9550-15-1-0247 and FA9550-15-1-0377.

REFERENCES

1. A. Rogalski, *Rep. Prog. Phys.* 68, 2267 (2005).
2. M.A. Kinch, *J. Electron. Mater.* 29, 809 (2000).
3. D. Lee, M. Carmody, E. Piquette, P. Dreiske, A. Chen, A. Yulius, D. Edwall, S. Bhargava, M. Zandian, and W.E. Tennant, *J. Electron. Mater.* 45, 4587 (2016).
4. T. Ashley, C.T. Elliott, and A.M. White, *Infrared Tech. XI* 572, 123 (1985).
5. T. Ashley, C.T. Elliott, and A.T. Harker, *Infrared Phys.* 26, 303 (1986).
6. P.Y. Emelie, S. Velicu, C.H. Grein, J.D. Phillips, P.S. Wijewarnasuriya, and N.K. Dhar, *J. Electron. Mater.* 37, 1362 (2008).
7. J. Easley, E. Arkun, M. Carmody, and J. Phillips, *J. Electron. Mater.* 46, 5479 (2017).
8. J. Wrobel, K. Gorczyca, G.A. Umana-Membreno, A. Kębłowski, J. Boguski, P. Martyniuk, and P. Madejczyk, in *Proceedings of SPIE*, vol. 10455 (2017), p. 104550T-1.
9. J. Antoszewski, L. Faraone, I. Vurgaftman, J.R. Meyer, and C.A. Hoffman, *J. Electron. Mater.* 33, 673 (2004).
10. J.R. Meyer, C.A. Hoffman, J. Antoszewski, and L. Faraone, *J. Appl. Phys.* 81, 709 (1997).
11. W.A. Beck and J.R. Anderson, *J. Appl. Phys.* 62, 541 (1987).
12. J. Antoszewski, D.J. Seymour, L. Faraone, J.R. Meyer, and C.A. Hoffman, *J. Electron. Mater.* 24, 1255 (1995).
13. I. Vurgaftman, J.R. Meyer, C.A. Hoffman, D. Redfern, J. Antoszewski, L. Faraone, and J.R. Lindemuth, *J. Appl. Phys.* 84, 4966 (1998).
14. B. Cui, Y. Tang, and M. Grayson, in *Proceedings of SPIE*, vol. 9370 (2015), p. 937030.
15. B. Cui and M. Grayson, In *Proceedings of SPIE*, vol. 10111 (2017), p. 101110N-1.
16. J.P. Rosbeck, R.E. Starr, S.L. Price, and K.J. Riley, *J. Appl. Phys.* 53, 6430 (1982).
17. M.A. Kinch, *Fundamentals of Infrared Detector Materials* (Washington: SPIE Press, 2007).
18. D. Tong, *Lectures on the Quantum Hall Effect* (2016). arXiv:1606.06687. Accessed 16 July 2018.

NANO LETTERS

Letter

pubs.acs.org/NanoLett

Quantum Transport and Sub-Band Structure of Modulation-Doped GaAs/AlAs Core−Superlattice Nanowires

Dominik M. Irber,[†] Jakob Seidl,[†] Damon J. Carrad,[†,⊥] Jonathan Becker,[†] Nari Jeon,[‡] Bernhard Loitsch,[†] Julia Winnerl,[†] Sonja Matich,[†] Markus Döblinger,[§] Yang Tang,[∥] Stefanie Morkötter,[†] Gerhard Abstreiter,[†] Jonathan J. Finley,[†] Matthew Grayson,[∥] Lincoln J. Lauhon,[‡] and Gregor Koblmüller*[,†]

[†]Walter Schottky Institut, Physik Department, and Center for Nanotechnology and Nanomaterials, Technical University of Munich, Garching, 85748, Germany

[‡]Department of Materials Science and Engineering, Northwestern University, Evanston, Illinois 60208, United States

[§]Department of Chemistry, Ludwig-Maximilians-Universität München, Munich 81377, Germany

[∥]Department of Electrical Engineering and Computer Science, Northwestern University, Evanston, Illinois 60208, United States

Supporting Information

ABSTRACT: Modulation-doped III−V semiconductor nanowire (NW) heterostructures have recently emerged as promising candidates to host high-mobility electron channels for future high-frequency, low-energy transistor technologies. The one-dimensional geometry of NWs also makes them attractive for studying quantum confinement effects. Here, we report correlated investigations into the discrete electronic sub-band structure of confined electrons in the channel of Si δ-doped GaAs−GaAs/AlAs core−superlattice NW heterostructures and the associated signatures in low-temperature transport. On the basis of accurate structural and dopant analysis using scanning transmission electron microscopy and atom probe tomography, we calculated the sub-band structure of electrons confined in the NW core and employ a labeling system inspired by atomic orbital notation. Electron transport measurements on top-gated NW transistors at cryogenic temperatures revealed signatures consistent with the depopulation of the quasi-one-dimensional sub-bands, as well as confinement in zero-dimensional-like states due to an impurity-defined background disorder potential. These findings are instructive toward reaching the ballistic transport regime in GaAs−AlGaAs based NW systems.

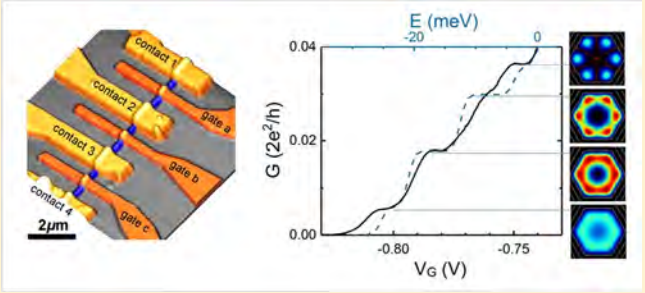

KEYWORDS: *Core−multishell heterostructure nanowires, modulation doping, low-dimensional electron transport, structural properties*

Semiconductor nanowires (NWs) are well established as an important platform for photonics and electronics research due to the ability to grow material combinations not possible in planar structures. In particular, the growth of complex radial and axial heterostructures[1,2] and the incorporation of III−V materials directly on Si substrates[3−5] has facilitated the realization of various novel NW-based devices, including high-performance lasers[6] and transistors,[7,8] as well as radial and axial Esaki diodes and tunneling devices.[9−11] In electronics, the morphology of NWs lends them to fabrication of gate-all-around and omega-gated field effect transistors (FETs) with close to optimal channel coupling.[12−16] This holds promise both for deployment in high-frequency, low-energy transistors for future technology[17] as well as for strongly tuning quantum confinement and studying quantum phenomena at cryogenic temperatures.[18−20] In this regard, there is significant interest in exploiting quantum-confined NWs, for example, for the generation and manipulation of Majorana Fermions,[21] realization of ballistic transport,[22−24] and enhancement of thermoelectric conversion efficiency by exploiting the discontinuity in the one-dimensional (1D) density of states.[25−28] These applications in general require high purity, high mobility conduction channels to ensure coherent 1D transport. Therefore, development and improvement of high-mobility quantum confined charge carrier systems in NWs is an important goal for ongoing quantum electronics research.

One of the most popular materials systems for high mobility quantum transport are modulation-doped GaAs−AlGaAs heterostructures.[29] The improved mobility brought by separating the two-dimensional conduction channel from the dopants has enabled many ground-breaking discoveries in low-dimensional condensed matter physics.[30,31] In conventional planar heterostructures, quantized conductance has been realized from high-mobility two-dimensional electron gases (2DEG) either by electrostatically defined quantum point contacts[32] or "T-shaped" quantum wells via cleaved-edge

Received: April 28, 2017
Revised: June 23, 2017
Published: July 21, 2017

DOI: 10.1021/acs.nanolett.7b01732
Nano Lett. 2017, 17, 4886−4893

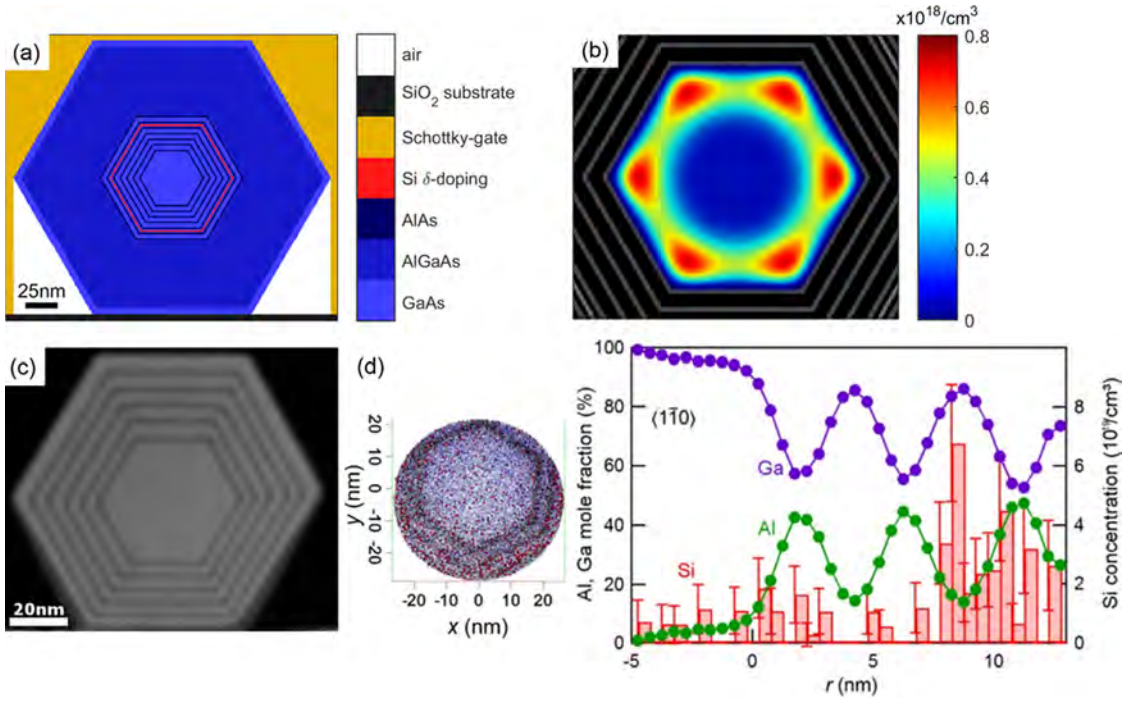

Figure 1. (a) Cross-sectional schematic of the gated Si δ-doped GaAs−GaAs/AlAs core−superlattice NW heterostructure in a field effect transistor geometry using omega-shaped Schottky-type gates. (b) Free electron density distribution in the NW core as obtained from self-consistent Schrödinger-Poisson solutions for T = 4.2K and zero gate bias. (c) STEM-HAADF image of the relevant inner NW-core/SL-shell region as obtained from a reference sample. (d) Corresponding APT elemental map (left) and proximity histogram (right) of the Al- and Ga-molar fractions and Si dopant distribution as recorded radially along one of the major {1-10} directions. The core−shell interface is at r = 0 nm. The color code in the APT elemental map correspond to those presented in the histogram (Ga, purple; Al, green; Si, red). To ensure that the Si dopants are within the finite field-of-view of the APT measurement, the Si-dopants were placed in the second innermost GaAs QW of an APT reference structure grown without the thick AlGaAs barrier and with a reduced number of superlattice layers.

overgrowth.[33] More recently, attention has turned to adapting the modulation-doping technique to core−shell GaAs−AlGaAs NWs due to the proposed formation of high mobility quasi-1D channels.[8,34−40] To date, most experimental efforts have aimed at demonstrating carrier mobility enhancement using modulation-doping schemes[8,38,40] as well as testing room-temperature transistor performance.[8,41] In contrast, exploration of low-temperature quantum transport and correlations with the electronic sub-band structure as necessary for the development of quasi-1D conduction channels has remained largely unexplored.

In this Letter, we report the low-temperature transport properties of novel Si δ-doped GaAs−AlAs core−superlattice NW heterostructures and correlate transport signatures with discrete electronic sub-bands in the conduction channel. In particular, we observed characteristic 1D-like conductance plateaus and show that the plateau heights directly correlate with single and double degenerate sub-band levels generated by the rotational hexagonal symmetry of the NW. Our investigations also provide insights into additional zero-dimensional (0D)-like confinement arising from disorder potentials due to background impurities. High-resolution structural analysis of the grown superlattice structure and Si δ-dopant incorporation (placement and density) using scanning transmission electron microscopy (STEM) combined with energy dispersive X-ray spectrometry (EDXS) and atom probe tomography (APT) enabled accurate simulations for comparison with experiments.

A representative cross-section of the investigated NW structure is illustrated in Figure 1a. The device design is similar to that of a previously reported GaAs−AlGaAs core−shell NW-FET structure[8] but here an improved shell structure and doping scheme were employed. In particular, we used a short-period GaAs-AlAs superlattice (SL) structure radially grown around the GaAs NW core where one single GaAs quantum well (QW) within the SL hosts the Si δ-doping layer. Similar to conventional modulation doping of ternary AlGaAs shell layers,[8] the ionized Si dopants induce a free electron gas confined in the NW core. The overall two-dimensional electron density distribution map is shown in Figure 1b, and details of the electron density calculations and associated conduction band profile are further described below and in the Supporting Information. The first advantage of selective doping of a narrow GaAs QW within short-period SLs is preventing the formation of deep trap states (so-called *DX* centers) that arise in ternary $Al_xGa_{1-x}As$ for x(Al) > 0.22.[42,43] *DX*-centers in planar modulation doped structures are thought to be responsible for undesired persistent photoconductivity effects, gate instability and charge noise. A second benefit is that the superlattice is expected to reduce alloy disorder scattering relative to the ternary $Al_xGa_{1-x}As$ and further smoothen potential fluctuations of proximal ionized Si dopants, thereby increasing electron mobility.[44,45]

The modified Si δ-doped GaAs-(AlAs/GaAs) core−shell NW heterostructures were grown on prepatterned SiO_2/Si(111) substrates via a two-step growth process using molecular beam epitaxy (MBE). In the first step, vertical [111]-oriented GaAs NWs were grown to a length of ~8 (±1) μm using a self-catalyzed vapor−liquid−solid (VLS) growth process at a temperature of 630 °C.[46] Under the given growth

DOI: 10.1021/acs.nanolett.7b01732
Nano Lett. 2017, 17, 4886−4893

process, the NWs are slightly tapered.[44] In the second growth step, we employed a lower growth temperature (490 °C) and higher V/III flux ratio to induce predominantly radial growth along the {1-10} sidewall facets.[47] The NW core was directly overgrown by a short-period GaAs-AlAs SL (seven periods) where the respective layer thicknesses were precisely tuned to eight monolayers (3.2 nm) of GaAs and three monolayers (1.2 nm) of AlAs. This specific SL structure provides miniband ground states in the Γ conduction band (CB) that closely mimic the band edges of a ternary AlGaAs layer with an Al-content of x(Al) = 0.15. Details on the miniband formation as obtained from band profile simulations using the nextnano++ device simulator[48] are given in the Supporting Information. The Si δ-doping layer was introduced in the center of the fifth GaAs QW away from the NW core by means of a growth interruption and a supply of Si dopants for 10 min. This yielded a spacer layer with effective thickness of 20 nm between the core−shell interface and the dopant layer. Surrounding the GaAs−AlAs SL, a 54 nm thick ternary $Al_xGa_{1-x}As$ barrier with x(Al) = 0.15 was grown to match the shell thicknesses of previous ternary-only NW core−shell heterostructures.[8] A 5 nm GaAs capping layer was added to prevent oxidation. We also grew a reference sample for correlated APT and STEM analysis in order to study the composition and dopant distribution in the relevant region of interest. The reference sample was grown without the thick AlGaAs barrier due to the limited field of view in APT. Similarly, the SL was reduced to five periods and the Si δ-doped layer was placed in the second innermost GaAs QW.

A representative STEM-high-angle annular dark-field (HAADF) image of a cross-sectional lamella fabricated from the NW reference sample is shown in Figure 1c. The Z-contrast of the STEM image appears to reproduce the nominal NW-core and radial SL structure fairly well with a core diameter of $d \sim 40-50$ nm and thicknesses of the alternating SL layers of (3.6 ± 0.7) nm for GaAs (bright layers) and (1.5 ± 0.1) nm for AlAs (dark layers), as measured along the major {1-10} sidewall orientations. EDXS measurements of the SL structure reveals that the individual layers are not completely pure GaAs and AlAs. In particular, the GaAs layers contain a low Al-molar fraction of x(Al) ∼ 0.07 ± 0.03, while the ultrathin AlAs layers exhibit much higher Ga-molar fraction up to 0.60 ± 0.05 representing rather Al(Ga)As barriers. The origin of the unexpectedly high Ga-molar fraction in these Al(Ga)As layers is not fully clear but may be due to intermixing effects, artifacts arising from sample preparation using a Ga^+ focused ion beam, and/or instabilities of the electron probe during spectrum acquisition. The SL structure and the deviations from the nominal composition are also observed in the end-view APT map and associated APT line scan of the Ga- and Al-molar fractions taken along the {1-10} orientation (Figure 1d). We note, however, that due to instrumental broadening in APT the actual variation of the Al-molar fraction in the Al(Ga)As barrier layers is likely to be larger than shown in Figure 1d. The broadening effects are also directly seen in the increased Al(Ga)As barrier thickness in APT as compared to the STEM data. Moreover, both the APT and STEM-HAADF-EDXS data show that the Al-molar fraction and the respective barrier thickness is increased in the six equivalent {11-2}-oriented corner facets of the Al(Ga)As layers (see Supporting Information). This observation is expected in Al-rich ternary III−V materials[8,47,49] due to different surface diffusivities of Al and Ga adatoms on the nonplanar sidewall surfaces. Importantly, Figure 1d plots the Si dopant distribution, showing that the intentional Si dopants are well confined within the second GaAs QW away from the core−shell interface. The peak Si concentration from δ-doping the {1-10} growth facets is $\sim 7 \times 10^{19}$ cm^{-3}. The measured Si concentration was directly used as an input parameter for the free electron density calculation shown in Figure 1b as well as for the following electronic structure calculations.

A Hartree solver (nextnano++)[48] was used to obtain self-consistent solutions of the Schrödinger-Poisson equation while fully modeling the hexagonal NW geometry under the measured doping density. Figure 2a shows simulations of the radial electron density distribution and energy level spacing for the discrete sub-bands that arise due to the confinement in the NW core. A total of five discrete occupied energies below the Fermi edge are observed for a NW diameter d = 42 nm. The existence of the 1D sub-bands and the shape of the electron density depends intimately on both the existence of the δ-doping layer as well as the confinement from the narrow core. This is evident from the fact that increasing either the diameter d or doping density[35] increases the number of occupied states and that increasing d also reduces the energetic spacing of the states. We show the diameter dependence of sub-band energies as well as a detailed study of electron distributions for NW diameter d = 53 nm under equivalent doping density in the Supporting Information. Our simulations using a realistic hexagonal NW geometry allow us to further comment on the wave functions in more detail. In particular, we can describe the levels in terms of the familiar atomic orbital notation because the wave function symmetry is essentially related to the angular momentum, l. With the angular momentum vector fixed to the nanowire axis, the total angular momentum l can have a z-component projected either along or opposite to the nanowire axis, $m_l = \pm l$. Thus, the degeneracy of the states is g = 1 for l = 0 and g = 2 for all $l \neq 0$. This result is consistent with the degenerate second/third and fourth/fifth sub-bands observed in previous simulations of cylindrical nanowires.[50−52] Note that because the Hartree solver generates purely real solutions to the 2D nanowire cross-section, the electron density maps plotted in Figure 2 are the symmetric and antisymmetric linear combinations $|S\rangle \sim |l, m\rangle + |l, -m\rangle$ and $|A\rangle \sim |l, +m\rangle - |l, -m\rangle$ of the angular momentum states. The corresponding amplitudes of the single-particle wave functions of these discrete states are shown in the Supporting Information, confirming that the nodal planes are sign changes of the wave function.

Under the atomic orbital convention the state lowest in energy at $E - E_F = -25.5$ meV is classified as an s-like state (l = 0) as it simply reproduces the underlying hexagonal NW confinement potential. The associated radial symmetry means this state has only one magnetic quantum number m_l = 0. The next states higher in energy are doubly degenerate and are classified as p-like states (l = 1) with even and odd reflection symmetry about the x-axis. Analyzing the angular nodal profile gives nodal planes at x = 0 ($|p_x\rangle = |1,1\rangle + |1,-1\rangle$), and at y = 0 ($|p_y\rangle = |1,1\rangle - |1,-1\rangle$). Further degenerate states are classified as d-like (l = 2) and f-like (l = 3) states. Although the degenerate states separately lack hexagonal symmetry, when the charge densities are added together, they reproduce nicely the hexagonal symmetry of the NW confinement potential. Importantly, we observe a lifted degeneracy for the f-like states. The fact that this would not be observed if modeling a cylinder[50] illustrates the importance of modeling the realistic

DOI: 10.1021/acs.nanolett.7b01732
Nano Lett. 2017, 17, 4886−4893

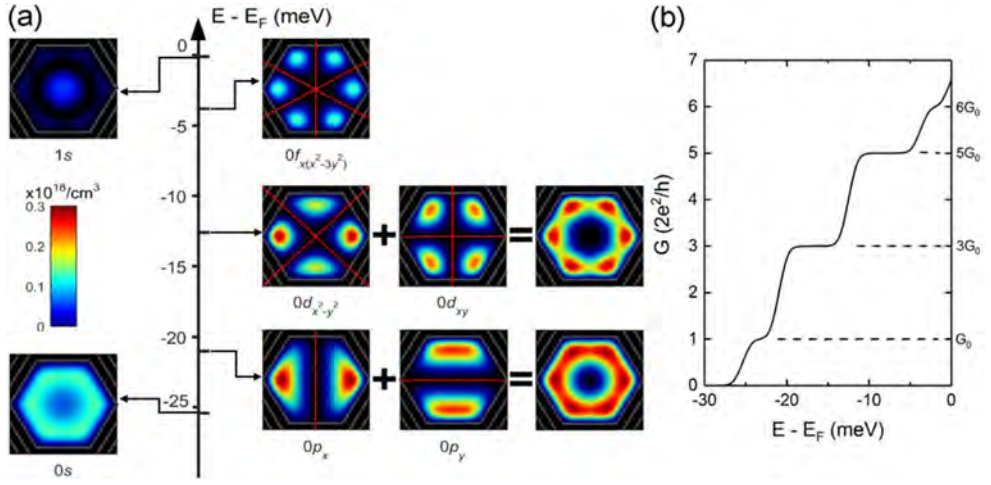

Figure 2. (a) Calculated energy spectrum of discrete electronic states of the confined electron gas within the radial Si δ-doped GaAs−GaAs/AlAs core−superlattice NW heterostructure. Each plot shows the 2D electron density distribution inside the NW core as obtained for T = 4.2 K and core-diameter d = 42 nm. The five individual states below the Fermi edge, E_F = 0 eV, are classified according to atomic orbital notation (labeled as $nl_{f(x,y)}$) due to their radial dependence and angular symmetry. The dotted red lines correspond to the angular nodal planes given by $f(x,y) = 0$ which can be related to magnetic quantum numbers $m_l = \pm l$ via the angular part of the spherical harmonics. Energetically degenerate states are added up to demonstrate that each energy level reproduces the underlying hexagonal symmetry of the NW confinement potential. (b) Simulated transport properties assuming ballistic transport in one-dimensional modes under a fixed source-drain voltage V_{SD} = 2 mV. An external electric field E reduces the conductance G in discrete steps in integer multiples of $G_0 = 2e^2/h$. The double degeneracy of the second and third state results in no plateaus at $G = 2 \times 2e^2/h$ and $4 \times 2e^2/h$.

hexagonal NW structure. Note that the second f-like state is unoccupied for the modeled core diameter of d = 42 nm and thus not shown in Figure 2, while it is occupied for larger diameter NWs (see Supporting Information).

Overall, each set of states produces a slightly different spatial confinement of the electron density in the NW. For example, comparing the sum of both d-like states to the sum of both p-like states shows that the electron density for the former is slightly more confined at the core−shell interface and in the corner facets. Higher energy discrete states are characterized by higher radial quantum number n. Such states with $n \geq 1$ can be assigned by counting the number of radial nodes at which the sign of the wave function changes between the center of the NW core and core−shell interface (see also amplitude profiles of single-particle wave functions in the Supporting Information). The n = 1 state with the lowest energy ($E - E_F$ slightly below 0) is the 1s-like state, which also exhibits the intrinsic hexagonal symmetry of the NW. Continuing higher in energy, the next possible states are not occupied, and therefore not shown here, because they lie above the Fermi edge. It is also interesting to note that the selection rule for atomic orbitals $l < n$ does not apply for the electronic NW states, because the first orbital shell (n = 0) already features occupied angular momentum states up to l = 3 (f-like states) and even higher l for larger core diameters (see the Supporting Information).

An important conceptual note is that each electron density cross-section plot represents a single, continuous wavefunction. The hexagonally symmetric confinement potential generated by the combination of the core radius and doping scheme has dimensions comparable to the electron wavelength, so each sub-band consists of a 1D mode that propagates in the direction of the NW axis. In particular, the presence of local maxima at the NW corners does *not* indicate the presence of six independent 1D channels. Rather, these are local maxima and minima of a single mode in the underlying hexagonal confinement potential. Prior to this work, the hexagonally distributed nature of these individual subbands had not bee considered.[22,27,50−52,55]

Figure 2b shows how these 1D-confined states influence electrical transport characteristics assuming an ideal ballistic conducting channel where the carrier density is modulated by an external electric field E. The applied source-drain bias V_{SD} = 2 mV was chosen to be smaller than the energetic separation between any two adjacent levels. Further details regarding the simulations are described in the Supporting Information. The conductance G consists of steps between constant plateaus as the Fermi level passes through each discrete 1D sub-band. The first plateau occurs at $G_0 = 2e^2/h$ as for traditional one-dimensional systems. Importantly, however, no plateaus exist at $2 \times 2e^2/h$ and $4 \times 2e^2/h$ due to the rotational hexagonal symmetry of the NW and the associated degeneracy of the second and third states. Instead, the plateaus at $3 \times 2e^2/h$ and $5 \times 2e^2/h$ have a plateau width roughly twice as wide as the singly degenerate plateaus, because the density of two sub-bands must be depleted. Below we directly confirm by experiment that plateaus associated with the two doubly degenerate levels indeed have step heights twice as high as the other plateaus.

We fabricated NW-FET devices to enable the gate-dependent study of quantum confinement features at cryogenic temperatures $T \sim 4.2$ K. Details regarding device fabrication are illustrated in the Supporting Information. The device shown in Figure 3a features four ohmic contacts (AuGe/Ni/Ti/Au) and three Schottky-type gates (Ti/Au with lengths ~350−400 nm) along the NW to enable spatially resolved correlation of structural and electronic properties.[8] This is particularly important because quantum confined electron transport in NWs is strongly dependent on structural factors such as stacking faults (SF), twin defects and other impurities.[53] Similarly, the proximity to the conduction channel makes electron transport highly sensitive to impurities at the surface, interfaces and in the substrate.[51,54−57] Taken together, this has long made experimentally observing robust ballistic one-

DOI: 10.1021/acs.nanolett.7b01732
Nano Lett. 2017, 17, 4886−4893

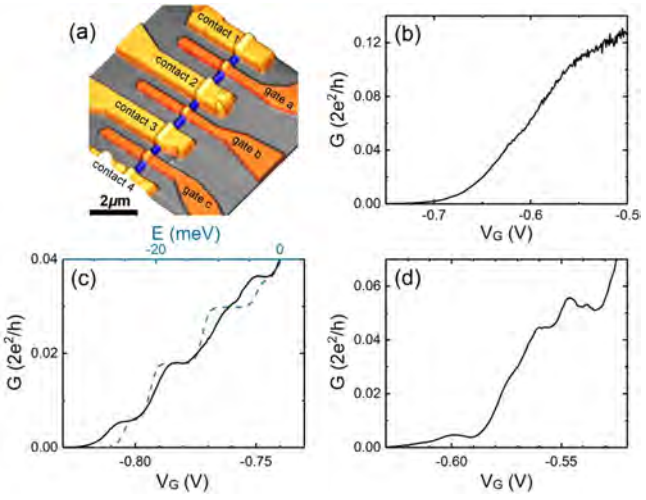

Figure 3. (a) Color-coded atomic force micrograph of representative NWFET used for (b,c) low-temperature measurements of conductance G versus gate voltage V_G conducted at T = 4.2 K and V_{SD} = 2 mV. The NWFET in (a) features four AuGe-based ohmic contacts (yellow) and three Ti/Au Schottky-type gates (orange) that were used to correlate structural/electronic properties along the NW length (blue). The scale bar represents 2 μm. (b) Applied V_G to gate "a" typically resulted in smooth depletion without quantum-confined features, likely due to the high stacking fault density and larger core diameter in this region. (c) The comparatively low defect density underneath gate "b" enabled diffusive 1D transport with the G reduced in discrete steps of $G'_0 = 0.006G_0$. Note the good agreement in plateau height between the experimental data (black solid trace) and simulated data (blue dashed trace). (d) Transport obtained from the same gate "b" under a separate cool-down. The data consist of Coulomb blockade resonances superposed on the trace, which suggests a strong influence from randomly positioned impurity charges.

dimensional transport in NW devices problematic[54,55] and typically requires extensive optimization of the surfaces/interfaces and short gate lengths.[51,52] We expect the influence of surface states to be limited due to the separation between the conduction channel and surface in our modulation doped devices. This assumption is reasonable given the near-ideal subthreshold swing with negligible gate hysteresis previously reported in similar NW-devices.[8] However, alloy fluctuations[58] and the inevitable random background charged impurities create random fluctuations in the scattering potential that become more influential upon cool-down to T = 4.2 K. The magnitude and spatial distribution of potential fluctuations change on each cool-down and can be made to evolve further under the influence of the gate electric field.[19]

Figure 3b–d outlines three distinct transport regimes typically observed in the G versus V_G characteristic at T = 4.2 K with applied alternating current (ac) excitation of amplitude V_{SD} = 2 mV (see Supporting Information for measurement techniques and details on estimating G). Each regime can be linked to a particular form of the background scattering potential, highlighting the decisive role this plays in nanowire transport properties. First, Figure 3b illustrates the "classical" regime whereby the electron density was smoothly depleted and G showed no quantum confinement features. This likely arose from a high density of scattering centers "washing out" 1D and 0D features. Indeed, this trace was taken on an end section of the NW under gate "a", where previous structural analysis of NWs grown under the same conditions identified a very high stacking fault density (~40 SF/μm).[8] The GaAs core diameter at this end section was $d \sim 42$ nm, as derived from height profiling using atomic force microscopy. While simulations in Figure 2 suggested that quantum confinement should be present at this diameter, the relatively high defect density likely prevented ballistic transport in quantum confined modes due to enhanced scattering.

By contrast, probing the central section of the NW under gate "b" indicated distinct quantum confinement features (Figure 3c,d), enabled by the much lower defect density[8] in this region and likely thinner core diameter due to slightly tapered NW core growth. Data obtained from two separate cool downs highlight the second and third characteristic transport regimes, as seen in Figure 3c,d, respectively. For the cooldown shown in Figure 3c, G versus V_G consisted of step/plateau features similar to those generated by the simulations in Figure 2b. Importantly, the data shows that plateaus associated with the two doubly degenerate levels feature step heights twice as high as the other plateaus. The major difference with respect to simulated data is that the G plateaus occurred at values less than integer multiples of $2e^2/h$. This is unsurprising because we expect significant scattering and the long gate lengths (~400 nm) to substantially lower the transmission probability and prevent ballistic transport.[50,51] Modifying the simulation to incorporate a lower transmission probability (~0.006) brings the simulated step-heights into excellent agreement with the experimental values. The observation of discrete steps with lower transmission probability suggests that electron transport for this measurement occurred via diffusive one-dimensional modes. Transport in diffusive 1D modes with a similar transmission probability has been also reported in InAs NW devices with long channel lengths.[50] A second contribution to the low G value may arise from our method used to subtract the contact resistance, which necessarily results in a low-bound estimate for the channel conductance (see Supporting Information). Furthermore, we observe a slight deviation between experiment and simulation in terms of the energy level spacing, that is, plateau width. This may be due to, for example, variations in the gate-channel coupling between different sub-bands, or a residual influence from quantum dot-like states that we describe below. Such uncertainties mean that direct comparisons between experiment and simulation in the nanowire literature have been limited mostly to the first two plateaus.[50,51,55]

The third transport regime (Figure 3d) highlights the strong influence of the random background potential has on the ability to resolve the one-dimensional modes. The trace in Figure 3d was taken on the same segment of the same NW as in Figure 3c but on a separate cool-down where statistical fluctuations in the occupation of nearby impurity states is expected to alter the charge background.[59] Rather than the stepwise sub-band depopulation observed in Figure 3c, Figure 3d shows additional superimposed Coulomb blockade-like resonances with most pronounced features occurring near V_G = −0.60 V and V_G = −0.55 V. This behavior is characteristic of transport consisting of 1D propagating modes weakly coupled to quantum dot-like states. It is typically observed for NWs when transport is dominated by a number of strong scattering centers[19,26,54] and is similar to the stochastic Coulomb blockade effect.[60,61] Given their random nature, these transport signatures likely do not arise from permanent structural features, such as stacking faults. Rather, we suggest a small number of charge traps in the vicinity of the conduction channel were responsible for the observed behavior. The randomized occupation of these traps

DOI: 10.1021/acs.nanolett.7b01732
Nano Lett. 2017, 17, 4886–4893

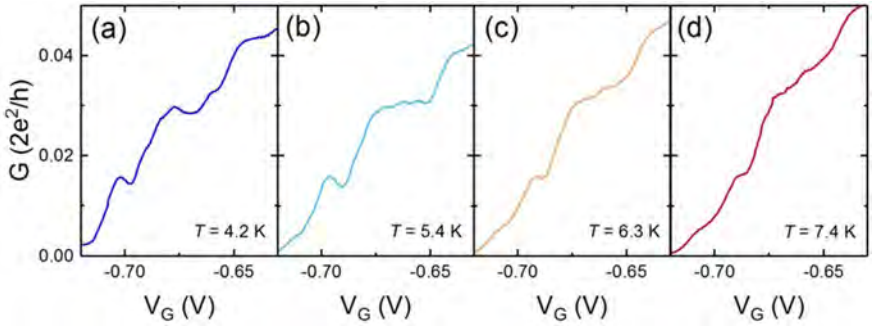

Figure 4. Evolution of electron transport under gate "b" on a different device from that in Figure 3 with increasing temperature for (a) T = 4.2 K, (b) T = 5.4 K, (c) T = 6.3 K, and (d) T = 7.4 K. At T = 4.2 K, prominent Coulomb blockade resonances are visible. However, at T = 7.4 K the transport resembles the stepwise depletion characteristic of 1D transport. Increasing the electron thermal energy k_BT above the quantum dot-like state confinement energy for $T \sim 6-7$ K enabled electrons to propagate through the nanowire in one-dimensional modes.

on each cool-down produced a background disorder potential that determined the resulting electron transport signatures.[19]

Finally, an instructive way to probe the relative influence of the 0D and 1D confinement is to use temperature, because the ability to observe the confinement depends on the magnitude of the confinement energy relative to the thermal energy $\sim k_BT$. We demonstrate this using a second device, again measuring the segment under gate "b". Figure 4a–d shows G vs V_G traces taken at T = 4.2, 5.4, 6.3, and 7.4 K, respectively. At T = 4.2 K, G versus V_G was dominated by Coulomb blockade resonances, similar to the second cool-down from the first device (i.e., Figure 3d). The effect of increased temperature was to raise the thermal energy of electrons so that confinement in the direction of transport was small by comparison. This enabled the free propagation of electrons in the 1D modes and the strong reduction of the quantum dot-like features. The evolution is especially evident between T = 5.4 and 6.3 K and best seen for the lowest state near V_G = −0.7 V (Figure 4b,c, respectively). This suggests a confinement energy of the 0D states on the order of 0.5 meV; much lower than the calculated confinement energy for 1D states of ∼5–10 meV. Note that the influence of the Coulomb blockade resonances is most prominent close to depletion, because the average kinetic energies of the charge carriers are lower and thus longitudinal confinement along the NW axis plays a more dominant role.[26] At T = 7.4 K, G was reduced in discrete steps with negative V_G, similar to Figure 3c. Note, however, that the plateau-like features are less distinct in Figure 4d due to temperature broadening of the Fermi functions in the leads. Additionally, the height of the third and fourth plateaus was increased compared to the expected value. We suggest that temperature assisted transport through higher sub-bands was responsible for this behavior, but could also have arisen as an artifact from the method used to estimate G (see Supporting Information). These features encourage further optimization of NW structure with less scattering centers (stacking defects, alloy fluctuations, random background impurities) as well as employment of fully wrapped gates with shorter gate-length to observe ultimate coherent 1D transport.

In conclusion, we demonstrated the growth and low-temperature transport properties of novel modulation-doped GaAs–GaAs/AlAs core–superlattice NW heterostructures. Structural analysis by scanning TEM and APT confirmed the precise short-period superlattice structure as well as the accurate radial incorporation of Si dopants into a single GaAs layer. We investigated electron transport in the core at T = 4.2 K by simulation of ideal one-dimensional transport using a hexagonal confinement potential and analyzed the modes with a simple model inspired by atomic orbital labeling. These modes were observed in electrical measurements at T = 4.2–7.4 K but were frequently obscured by charged impurities contributing to a background potential consisting of tunneling barriers along the NW length. Further optimization of the growth structure and gate lengths to reduce the influences by the main scattering sources may bring similar devices closer to the ballistic limit.

■ ASSOCIATED CONTENT

Supporting Information

The Supporting Information is available free of charge on the ACS Publications website at DOI: 10.1021/acs.nanolett.7b01732.

Details on compositional structure, electron density simulations, including conduction band-profile, single particle wave functions and simulations of energy level spectra for d = 53 nm, as well as fabrication and electrical measurement methods (PDF)

■ AUTHOR INFORMATION

Corresponding Author

*E-mail: gregor.koblmueller@wsi.tum.de.

ORCID

Lincoln J. Lauhon: 0000-0001-6046-3304

Gregor Koblmüller: 0000-0002-7228-0158

Present Address

⊥(D.J.C.) Center for Quantum Devices, Niels Bohr Institute, University of Copenhagen, Universitetsparken 5, DK-2100 Copenhagen, Denmark.

Author Contributions

The manuscript was written through contributions of all authors. All authors have given approval to the final version of the manuscript. D.M.I. and J. S. contributed equally.

Notes

The authors declare no competing financial interest.

■ ACKNOWLEDGMENTS

The authors thank H. Riedl for technical support as well as Stefan Ludwig (Paul Drude Institute, Berlin) and Stefan Birner (nextnano GmbH) for helpful discussions. This work was funded by the DFG excellence program Nanosystems Initiative

DOI: 10.1021/acs.nanolett.7b01732
Nano Lett. 2017, 17, 4886–4893

Munich (NIM), the collaborative research center SFB 631, and the Technische Universität München, Institute for Advanced Study. Further support was provided by the TUM University Foundation Fellowship, the TUM International Graduate School of Science and Engineering (IGSSE), and the IBM Ph.D. Fellowship Program. This effort was also supported by AFOSR Grant FA9550-15-1-0247 as well as the National Science Foundation (Grants NSF 1611341 and 1308654).

REFERENCES

(1) Björk, M. T.; Ohlsson, B. J.; Sass, T.; Persson, A. I.; Thelander, C.; Magnusson, M. H.; Deppert, K.; Wallenberg, L. R.; Samuelson, L. *Appl. Phys. Lett.* **2002**, *80* (6), 1058−1060.
(2) Lauhon, L. J.; Gudiksen, M. S.; Wang, D.; Lieber, C. M. *Nature* **2002**, *420*, 57−61.
(3) Tomioka, K.; Motohisa, J.; Hara, S.; Fukui, T. *Nano Lett.* **2008**, *8* (10), 3475−3480.
(4) Borg, M.; Schmid, H.; Moselund, K. E.; Signorello, G.; Gignac, L.; Bruley, J.; Breslin, C.; Das Kanungo, P.; Werner, P.; Riel, H. *Nano Lett.* **2014**, *14* (4), 1914−1920.
(5) Schmid, H.; Borg, M.; Moselund, K.; Gignac, L.; Breslin, C. M.; Bruley, J.; Cutaia, D.; Riel, H. *Appl. Phys. Lett.* **2015**, *106* (23), 233101.
(6) Mayer, B.; Rudolph, D.; Schnell, J.; Morkötter, S.; Winnerl, J.; Treu, J.; Müller, K.; Bracher, G.; Abstreiter, G.; Koblmüller, G.; Finley, J. J. *Nat. Commun.* **2013**, *4*, 2931.
(7) Tomioka, K.; Yoshimura, M.; Fukui, T. *Nature* **2012**, *488*, 189−192.
(8) Morkötter, S.; Jeon, N.; Rudolph, D.; Loitsch, B.; Spirkoska, D.; Hoffmann, E.; Döblinger, M.; Matich, S.; Finley, J. J.; Lauhon, L. J.; Abstreiter, G.; Koblmüller, G. *Nano Lett.* **2015**, *15* (5), 3295−3302.
(9) Dey, A. W.; Svensson, J.; Ek, M.; Lind, E.; Thelander, C.; Wernersson, L.-E. *Nano Lett.* **2013**, *13* (12), 5919−5924.
(10) Yang, T.; Hertenberger, S.; Morkötter, S.; Abstreiter, G.; Koblmüller, G. *Appl. Phys. Lett.* **2012**, *101*, 233102.
(11) Moselund, K. E.; Schmid, H.; Bessire, C.; Bjork, M. T.; Ghoneim, H.; Riel, H. *IEEE Electron Device Lett.* **2012**, *33* (10), 1453−1455.
(12) Storm, K.; Nylund, G.; Samuelson, L.; Micolich, A. P. *Nano Lett.* **2012**, *12* (1), 1−6.
(13) Burke, A. M.; Carrad, D. J.; Gluschke, J. G.; Storm, K.; Fahlvik Svensson, S.; Linke, H.; Samuelson, L.; Micolich, A. P. *Nano Lett.* **2015**, *15* (5), 2836−2843.
(14) Storm, K.; Nylund, G.; Borgström, M.; Wallentin, J.; Fasth, C.; Thelander, C.; Samuelson, L. *Nano Lett.* **2011**, *11* (3), 1127−1130.
(15) Carrad, D. J.; Burke, A. M.; Lyttleton, R. W.; Joyce, H. J.; Tan, H. H.; Jagadish, C.; Storm, K.; Linke, H.; Samuelson, L.; Micolich, A. P. *Nano Lett.* **2014**, *14* (1), 94−100.
(16) Liang, D.; Du, J.; Gao, X. P. A. *J. Mater. Sci. Technol.* **2015**, *31* (6), 542−555.
(17) Egard, M.; Johansson, S.; Johansson, A.-C.; Persson, K.-M.; Dey, A. W.; Borg, B. M.; Thelander, C.; Wernersson, L.-E.; Lind, E. *Nano Lett.* **2010**, *10* (3), 809−812.
(18) Liang, D.; Gao, X. P. A. *Nano Lett.* **2012**, *12* (6), 3263−3267.
(19) Svensson, S. F.; Burke, A. M.; Carrad, D. J.; Leijnse, M.; Linke, H.; Micolich, A. P. *Adv. Funct. Mater.* **2015**, *25* (2), 255−262.
(20) Hu, Y.; Churchill, H. O. H.; Reilly, D. J.; Xiang, J.; Lieber, C. M.; Marcus, C. M. *Nat. Nanotechnol.* **2007**, *2*, 622−625.
(21) Mourik, V.; Zuo, K.; Frolov, S. M.; Plissard, S. R.; Bakkers, E. P. A. M.; Kouwenhoven, L. P. *Science* **2012**, *336*, 1003−1007.
(22) Heedt, S.; Prost, W.; Schubert, J.; Grützmacher, D.; SchäPers, Th. *Nano Lett.* **2016**, *16* (5), 3116−3123.
(23) Gooth, J.; Borg, M.; Schmid, H.; Schaller, V.; Wirths, S.; Moselund, K.; Luisier, M.; Karg, S.; Riel, H. *Nano Lett.* **2017**, *17*, 2596.
(24) Gooth, J.; Schaller, V.; Wirths, S.; Schmid, H.; Borg, M.; Bologna, N.; Karg, S.; Riel, H. *Appl. Phys. Lett.* **2017**, *110*, 083105.
(25) Hicks, L. D.; Dresselhaus, M. S. *Phys. Rev. B: Condens. Matter Mater. Phys.* **1993**, *47* (24), 16631.
(26) Wu, P. M.; Gooth, J.; Zianni, X.; Svensson, S. F.; Gluschke, J. G.; Dick, K. A.; Thelander, C.; Nielsch, K.; Linke, H. *Nano Lett.* **2013**, *13* (9), 4080−4086.
(27) Mensch, P.; Karg, S.; Schmidt, V.; Gotsmann, B.; Schmid, H.; Riel, H. *Appl. Phys. Lett.* **2015**, *106* (9), 093101.
(28) Tian, Y.; Sakr, M. R.; Kinder, J. M.; Liang, D.; MacDonald, M. J.; Qiu, R. L. J.; Gao, H.-J.; Gao, X. P. A. *Nano Lett.* **2012**, *12* (12), 6492−6497.
(29) Dingle, R.; Störmer, H. L.; Gossard, A. C.; Wiegmann, W. *Appl. Phys. Lett.* **1978**, *33* (7), 665−667.
(30) Klitzing, K.; Dorda, G.; Pepper, M. *Phys. Rev. Lett.* **1980**, *45*, 494−497. (29) Tsui, D. C.; Störmer, H. L.; Gossard, A. C. *Phys. Rev. Lett.* **1982**, *48*, 1559−1562.
(31) Petta, J. R.; Johnson, A. C.; Taylor, J. M.; Laird, E. A.; Yacoby, A.; Lukin, M. D.; Marcus, C. M.; Hanson, M. P.; Gossard, A. C. *Science* **2005**, *309*, 2180−2184.
(32) van Wees, B. J.; van Houten, H.; Beenakker, C. W. J.; Williamson, J. G.; Kouwenhoven, P. P.; van der Marel, D.; Foxon, C. T. *Phys. Rev. Lett.* **1988**, *60*, 848.
(33) de Picciotto, R.; Stormer, H. L.; Pfeiffer, L. N.; Baldwin, K. W.; West, K. W. *Nature* **2001**, *411*, 51.
(34) Ferrari, G.; Goldoni, G.; Bertoni, A.; Cuoghi, G.; Molinari, E. *Nano Lett.* **2009**, *9* (4), 1631−1635.
(35) Bertoni, A.; Royo, M.; Mahawish, F.; Goldoni, G. *Phys. Rev. B: Condens. Matter Mater. Phys.* **2011**, *84*, 205323.
(36) Spirkoska, D.; Fontcuberta i Morral, A.; Dufouleur, J.; Xie, Q.; Abstreiter, G. *Phys. Status Solidi RRL* **2011**, *5*, 353−355.
(37) Lucot, D.; Jabeen, F.; Harmand, J.-C.; Patriarche, G.; Giraud, R.; Faini, G.; Mailly, D. *Appl. Phys. Lett.* **2011**, *98*, 142114.
(38) Funk, S.; Royo, M.; Zardo, I.; Rudolph, D.; Morkötter, S.; Mayer, B.; Becker, J.; Bechtold, A.; Matich, S.; Döblinger, M.; Bichler, M.; Koblmüller, G.; Finley, J. J.; Bertoni, A.; Goldoni, G.; Abstreiter, G. *Nano Lett.* **2013**, *13*, 6189.
(39) Jadczak, J.; Plochocka, P.; Mitioglu, A.; Breslavetz, I.; Royo, M.; Bertoni, A.; Goldoni, G.; Smolenski, T.; Kossaki, P.; Kretnin, A.; Shtrikman, H.; Maude, D. K. *Nano Lett.* **2014**, *14*, 2807.
(40) Boland, J. L.; Conesa-Boj, S.; Parkinson, P.; Tütüncüoglu, G.; Matteini, F.; Rüffer, D.; Casadei, A.; Amaduzzi, F.; Jabeen, F.; Davies, C. L.; Joyce, H. J.; Herz, L. M.; Fontcuberta i Morral, A.; Johnston, M. B. *Nano Lett.* **2015**, *15*, 1336−1342.
(41) Miao, X.; Chabak, K.; Zhang, C.; Mohseni, P. K.; Walker, D.; Li, X. *Nano Lett.* **2015**, *15* (5), 2780−2786.
(42) Mooney, P. M. *J. Appl. Phys.* **1990**, *67* (3), R1−R26.
(43) Chand, N.; Henderson, T.; Klem, J.; Masselink, W. T.; Fischer, R.; Chang, Y.-C.; Morkoĉ, H. *Phys. Rev. B: Condens. Matter Mater. Phys.* **1984**, *30* (8), 4481.
(44) Manfra, M. J. *Annu. Rev. Condens. Matter Phys.* **2014**, *5* (1), 347−373.
(45) Friedland, K.-J.; Hey, R.; Kostial, H.; Klann, R.; Ploog, K. *Phys. Rev. Lett.* **1996**, *77* (22), 4616−4619.
(46) Rudolph, D.; Hertenberger, S.; Bolte, S.; Paosangthong, W.; Spirkoska, D.; Döblinger, M.; Bichler, M.; Finley, J. J.; Abstreiter, G.; Koblmüller, G. *Nano Lett.* **2011**, *11* (9), 3848−3854.
(47) Rudolph, D.; Funk, S.; Döblinger, M.; Morkötter, S.; Hertenberger, S.; Schweickert, L.; Becker, J.; Matich, S.; Bichler, M.; Spirkoska, D.; Zardo, I.; Finley, J. J.; Abstreiter, G.; Koblmüller, G. *Nano Lett.* **2013**, *13* (4), 1522−1527.
(48) Birner, S.; Zibold, T.; Andlauer, T.; Kubis, T.; Sabathil, M.; Trellakis, A.; Vogl, P. *IEEE Trans. Electron Devices* **2007**, *54* (9), 2137−2142.
(49) Steinke, L.; Grayson, M. *Appl. Phys. Lett.* **2008**, *93* (19), 193117.
(50) Ford, A. C.; Kumar, S. B.; Kapadia, R.; Guo, J.; Javey, A. *Nano Lett.* **2012**, *12* (3), 1340−1343.
(51) Chuang, S.; Gao, Q.; Kapadia, R.; Ford, A. C.; Guo, J.; Javey, A. *Nano Lett.* **2013**, *13* (2), 555−558.
(52) Kammhuber, J.; Cassidy, M. C.; Zhang, H.; Gül, Ö.; Pei, F.; de Moor, M. W. A.; Nijholt, B.; Watanabe, K.; Taniguchi, T.; Car, D.; Plissard, S. R.; Bakkers, E. P. A. M.; Kouwenhoven, L. P. *Nano Lett.* **2016**, *16* (6), 3482−3486.

DOI: 10.1021/acs.nanolett.7b01732
Nano Lett. 2017, 17, 4886−4893

(53) Schroer, M. D.; Petta, J. R. *Nano Lett.* **2010**, *10* (5), 1618−1622.
(54) Thelander, C.; Björk, M. T.; Larsson, M. W.; Hansen, A. E.; Wallenberg, L. R.; Samuelson, L. *Solid State Commun.* **2004**, *131* (9−10), 573−579.
(55) van Weperen, I.; Plissard, S. R.; Bakkers, E. P. A. M.; Frolov, S. M.; Kouwenhoven, L. P. *Nano Lett.* **2013**, *13* (2), 387−391.
(56) Zhou, X.; Dayeh, S. A.; Aplin, D.; Wang, D.; Yu, E. T. *Appl. Phys. Lett.* **2006**, *89* (5), 053113.
(57) Kretinin, A. V.; Popovitz-Biro, R.; Mahalu, D.; Shtrikman, H. *Nano Lett.* **2010**, *10* (9), 3439−3445.
(58) Jeon, N.; Loitsch, B.; Morkoetter, S.; Abstreiter, G.; Finley, J.; Krenner, H. J.; Koblmueller, G.; Lauhon, L. J. *ACS Nano* **2015**, *9* (8), 8335−8343.
(59) See, A. M.; Pilgrim, I.; Scannell, B. C.; Montgomery, R. D.; Klochan, O.; Burke, A. M.; Aagesen, M.; Lindelof, P. E.; Farrer, I.; Ritchie, D. A.; Taylor, R. P.; Hamilton, A. R.; Micolich, A. P. *Phys. Rev. Lett.* **2012**, *108*, 196807.
(60) Ruzin, I. M.; Chandrasekhar, V.; Levin, E. I.; Glazman, L. I. *Phys. Rev. B: Condens. Matter Mater. Phys.* **1992**, *45*, 13469.
(61) Moser, J.; Roddardo, S.; Schuh, D.; Bichler, M.; Pellegrini, V.; Grayson, M. *Phys. Rev. B: Condens. Matter Mater. Phys.* **2006**, *74*, 193307.

DOI: 10.1021/acs.nanolett.7b01732
Nano Lett. 2017, 17, 4886−4893

CHEMISTRY OF MATERIALS
Cite This: Chem. Mater. 2018, 30, 3847−3853
Article
pubs.acs.org/cm

Conversion of Single Crystal $(NH_4)_2Mo_3S_{13}·H_2O$ to Isomorphic Pseudocrystals of MoS_2 Nanoparticles

Saiful M. Islam,[†,⊥] Jeffrey D. Cain,[‡,§] Fengyuan Shi,[‡] Yihui He,[†] Lintao Peng,[∥] Abhishek Banerjee,[†] Kota S. Subrahmanyam,[†] Yuan Li,[‡] Shulan Ma,[#] Vinayak P. Dravid,[‡,§] Matthew Grayson,[∥] and Mercouri G. Kanatzidis*[,†]

[†]Department of Chemistry, [‡]Materials Science and Engineering, [§]International Institute for Nanotechnology, and [∥]Applied Physics Graduate Program, Northwestern University, Evanston, Illinois 60208, United States

[⊥]Department of Chemistry, Physics, and Atmospheric Sciences, Jackson State University, Jackson, Mississippi 39217, United States

[#]College of Chemistry, Beijing Normal University, Beijing 100875, China

Supporting Information

ABSTRACT: We have prepared nanocrystals of MoS_2 across a range of length scales by heating single crystals of the molecular precursor $(NH_4)_2Mo_3S_{13}·H_2O$. Rod-shaped crystals of the polysulfide precursor retain their original morphology after heating at temperatures up to 1000 °C and undergo complete conversion to MoS_2 while acting as a template for the confined formation of MoS_2 nanocrystals. This solid state transformation proceeds with the release of gaseous species without blowing the crystals apart and leads to formation of pores embedded into a nanocrystalline assembly of the templated nano-MoS_2. The obtained assemblies of MoS_2 nanocrystals have the exact same shape of the original rod-shaped $(NH_4)_2Mo_3S_{13}·H_2O$ crystals indicative of a pseudomorphic shape-retentive process. Such crystal-shaped nanocrystal assemblies show electrical conductivity values similar to a bulk MoS_2 single crystal with electron carrier concentration of 1.5×10^{14} cm^{-3} and mobility of 7 $cm^2/(V\ s)$. The nanocrystals of MoS_2 were grown at temperatures ranging from 450 to 1000 °C, and the sizes, shapes, morphologies, and their orientations can be engineered as a function of heating rate, soaking time, and temperature. These findings suggest a unique process for constrained templated nanocrystal growth from an organized molecular precursor structure with control of bulk morphology, size distribution, and orientation of nanocrystallites.

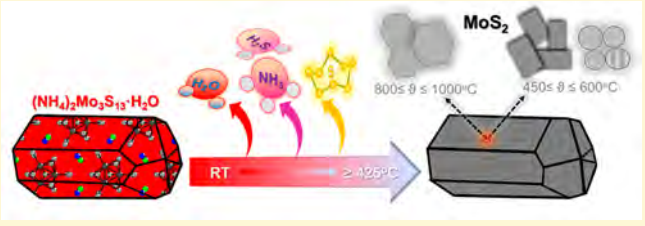

INTRODUCTION

Molybdenum disulfide (MoS_2) is of great interest for a wide variety of technological applications ranging from electronics to heterogeneous catalysis.[1−4] When the size of this material is reduced to the nanoscale, low-dimensional surface defects such as edges, corners, and kinks become dominant and define the electronic structure of the nanoparticles, which results in tunable optoelectronic properties and highly dense active catalytic sites.[1,5,6] For this reason, focus is centered on the synthesis of MoS_2 nanocrystals, with defined sizes, morphologies, stoichiometry, atomic ordering, and microstructures. A great variety of synthetic methods have been implemented including hydrothermal synthesis,[7,8] electrochemical deposition,[9] pulsed laser ablation,[10−12] microwave,[13,14] molten salt synthesis,[15,16] physical vapor deposition,[1,17] chemical vapor deposition (CVD),[18−22] thermal decomposition,[23,24,32,33] metal−organic chemical vapor deposition (MOCVD),[25] sol−gel methods,[26,27] sonochemical synthesis,[20,21] and chemical and mechanical exfoliation.[28,29] These methods yield MoS_2 nanocrystals with a variety of sizes and shapes such as hexagonal flakes, inorganic fullerene (IF)-like particles, nanotubes, nanorods, nanoflowers, nanowires, microspheres, hollow spheres, and porous irregularly shaped nanoparticle.[26,30−36] Despite such great advancements in the nanoscopic synthesis of MoS_2, up to now, solid state assembly of MoS_2 nanocrystals emerging from a single crystal molecular precursor as template to obtain porous isomorphic pseudocrystals of assembled MoS_2 nanoparticles is not known in the literature.

Herein, we report a direct high temperature (450 °C ≤ T ≤ 1000 °C) solid state reaction that leads to MoS_2 nanocrystals with controllable sizes, shapes, morphologies, and orientations. This is a unique solvent-free, scalable process that uses crystals of the molecular precursor $(NH_4)_2[Mo_3S(S_2)_6]·H_2O$ which features a trinuclear cluster[37] (see Figure 1A). Generally, high temperature conversion processes lead to large crystals and are not regarded as suitable routes toward nanomaterials synthesis. We show that the crystal structure of the chemically homogeneous solid precursor of hydrous $(NH_4)_2[Mo_3S(S_2)_6]·H_2O$ is unique in that upon heating it enables the rapid but orderly topotactic removal of H_2O molecules to give

Received: March 25, 2018
Revised: May 21, 2018
Published: May 21, 2018

DOI: 10.1021/acs.chemmater.8b01247
Chem. Mater. 2018, 30, 3847−3853

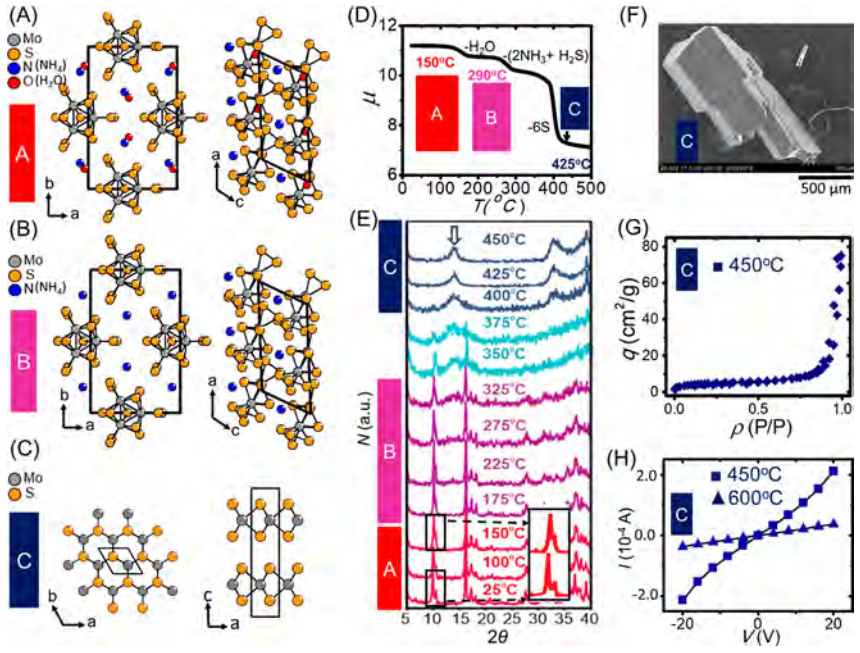

Figure 1. (A, B, C) Side by side comparison of the crystal structures of hydrous $(NH_4)_2Mo_3S_{13}\cdot H_2O$, anhydrous $(NH_4)_2Mo_3S_{13}$, and MoS_2, represented by A (red), B (pink), and C (blue) bars, respectively, for the successive figures. In (B), the absence of oxygen atoms depicted by the red circles corresponds to the absence of water molecules after heating to ~300 °C. (D) Thermogravimetric analysis of hydrous $(NH_4)_2Mo_3S_{13}\cdot H_2O$ shows fraction of mass loss, μ, by the release of H_2O, $2NH_3 + H_2S$, and S at temperatures, T, of 150, 290, and 425 °C, respectively. (E) In situ powder diffraction tracts the route of the conversion of $(NH_4)_2Mo_3S_{13}\cdot H_2O$ to MoS_2; (A, B, and C) bars represent the compounds corresponding to Figures A, B, and C. Inset in Figure E shows the shifting of the powder diffraction pattern with temperature; downward arrows indicate the formation of MoS_2. (F) Nanocrystalline assembly of MoS_2 single crystalline pseudomorph formed by heating in a templated fashion starting a single crystal of $(NH_4)_2Mo_3S_{13}\cdot H_2O$; see eq 1. (G) BET surface area of the molybdenum disulfides pseudomorph prepared at 450 °C as represented in Figure F. (H) Comparison of the $I-V$ curve of self-assembled nanocrystals into the isomorphic pseudocrystal of MoS_2 prepared at 450 and 600 °C.

anhydrous $(NH_4)_2[Mo_3S(S_2)_6]$ (Figure 1B) and the subsequent removal of NH_3, H_2S, and sulfur gas without destruction of the original crystal shape. The starting molecular crystals transform into crystals of identical shapes (pseudomorphs) but composed of porous assemblies of nanocrystalline layered MoS_2 (Figure 1C). In the present case we showed a spatially constrained solvent free process leading to a unique process for the synthesis of well-defined porous pseudomorphs. In addition, we showed that such high temperature solid state synthesis lead nanocrystals with fewer defect that can exhibit interesting optoelectronic properties.

RESULTS AND DISCUSSION

Red single crystals of the hydrous $(NH_4)_2[Mo_3S(S_2)_6]\cdot H_2O$ precursor, up to centimeter scales, were synthesized by heating an aqueous mixture of $(NH_4)_6Mo_7O_{24}\cdot 4H_2O$, $NH_2OH\cdot HCl$, and $(NH_4)_2S_x$ in an autoclave using a modified Mueller's method[37] (see Supporting Information for the detailed modified synthesis). Our study revealed that the compound can be synthesized at temperatures ranging from 90 to 220 °C. A yield of nearly ~100% (based on Mo content in $(NH_4)_6Mo_7O_{24}\cdot 4H_2O$) was obtained via a reaction at 220 °C over a period of 48 h, and thus this procedure is superior to Mueller's,[37] which yields ~20%.

The thermal behavior of hydrous $(NH_4)_2[Mo_3S(S_2)_6]\cdot H_2O$ with increasing temperature was studied by thermogravimetric analysis (TGA) (Figure 1D, fraction of mass, μ with temperature, T) and *in situ* X-ray powder diffraction (Figure 1E). The TGA curve reveals that this molecule transforms from the hydrous to anhydrous state at approximately 160 °C, which then remains steady until ~300 °C, signifying an impressive thermal stability of the anhydrous molecule, $(NH_4)_2[Mo_3S(S_2)_6]$. Subsequent heating above 300 °C decomposes the anhydrous $(NH_4)_2[Mo_3S(S_2)_6]$ to MoS_2 at ~425 °C through a gradual loss of volatile gaseous species like NH_3, H_2S, and sulfur or sulfur-containing species. This feature is in agreement with the observation of Mueller et al.[23]

In situ powder X-ray diffraction shows that at approximately 150 °C the diffraction pattern does not change, but the Bragg peaks shift to larger 2θ (inset in Figure E), demonstrating a contraction of the unit cell volume as a result of the hydrous to anhydrous $(NH_4)_2[Mo_3S(S_2)_6]$ transformation. From the *in situ* powder diffraction it can be seen that this polysulfide molecule, remarkably, is stable until 325 °C. This observation is consistent with the TGA, and the slight difference in the decomposition temperature is attributed to the different heating rate (see Supporting Information for a detailed experiment). In fact, this transformation is so orderly that when a single crystal of the hydrous $(NH_4)_2[Mo_3S(S_2)_6]\cdot H_2O$ material is used, a single crystal of the anhydrous version can be obtained which can be used to solve and refine the structure from single crystal X-ray diffraction data as will be presented below.

Subsequent heating at higher temperatures further decomposes the polysulfide molecule, and the crystalline $(NH_4)_2[Mo_3S(S_2)_6]$ converts to nanocrystalline MoS_2 at about 425 °C through a isomorphic transition occurring between ~350 and ~400 °C. By isomorphic we mean that the original crystals of the precursor retain their full shape even though the molecular compound no longer exists. The disappearance of the original X-ray diffraction pattern and appearance of broad diffraction peaks at 2θ ~14° along with

DOI: 10.1021/acs.chemmater.8b01247
Chem. Mater. 2018, 30, 3847−3853

others at 425 °C indicate the formation of nanocrystalline MoS_2.

The chemical environments and oxidation states of Mo, S atoms in the pristine hydrous $(NH_4)_2Mo_3S_{13}\cdot H_2O$, anhydrous $(NH_4)_2Mo_3S_{13}\cdot H_2O$ (300 °C heated sample), and the nanocrystalline MoS_2 (450 °C sample) were characterized with X-ray photoelectron spectroscopy (Figure S1). As synthesized, $(NH_4)_2Mo_3S_{13}\cdot H_2O$ exhibits the BEs of 228.86 and 232.06 eV for Mo^{4+} 3d and 164.39−161.86 eV for S 2p. The variability in the BEs of S 2p is attributed to two different oxidation states of as well as the splitting caused by the spin−orbit interaction in the sulfur atoms.[38] Within this range of BEs, the bands at 163.29 and 164.39 eV correspond to the S^{1-} $2p_{3/2}$ and $2p_{1/2}$, respectively while the bands centered at 161.86 and 162.96 eV correspond to the S^{2-} $2p_{3/2}$ and $2p_{1/2}$, respectively.[39] The change in the BEs of anhydrous $(NH_4)_2Mo_3S_{13}$ relative to pristine hydrous is insignificant, as expected. For the MoS_2 formed at 450 °C, the BEs at 230.16 and 233.30 eV correspond to Mo $3d_{5/2}$ and $3d_{3/2}$, respectively, while those at 163.26 and 164.36 eV represent the S $2p_{3/2}$ and $2p_{1/2}$, respectively, and are consistent with literature values. The Raman spectrum of the porous MoS_2 bulk pseudocrystal shows bands centered at ∼404 and ∼379 cm^{-1}, which represent the A_{1g} and E_{1g} vibrational modes of MoS_2, respectively (Figure S2).[40]

To validate hydrous to anhydrous single crystal transformation and its structural and compositional resilience, we determined the X-ray single crystal structure of the as-synthesized $(NH_4)_2[Mo_3S(S_2)_6]\cdot H_2O$ and annealed anhydrous crystal at 300 °C (Figure 1A,B). In agreement with Mueller et al.,[37] the hydrous $(NH_4)_2[Mo_3S(S_2)_6]\cdot H_2O$ consists of a Mo_3 triangle in which two molybdenum atoms are bridged by disulfide groups, $(S_2^{2-})_{bridge}$ so-called bridging sulfur, and an epical $(S^{2-})_{epical}$ (monosulfide group) in addition to a terminal $(S_2^{2-})_{term}$ group on each Mo. This molecular complex is stabilized by the $(NH_4)^+$ counterions besides the neutral crystal water. The crystal structure of the 300 °C annealed crystal is similar but shows a decreased unit cell size and the absence of H_2O molecules, which is in agreement with the TGA and *in situ* X-ray powder diffraction experiments. The unit cell parameters of the anhydrous $NH_4)_2[Mo_3S(S_2)_6]$ are a = 11.5136(23), b = 16.3569(33), c = 5.7209(11) Å, β = 117.746(30)°, and V = 953.52(42) Å^3, which are smaller than the hydrous version, with unit cell parameters a = 11.5673(23) Å, b = 16.4189(33) Å, c = 5.7049(11) Å, β = 117.366(30)°, and V = 962.23(42) Å^3.

When the single crystals of anhydrous $(NH_4)_2[Mo_3S(S_2)_6]$ are heated further, they convert to a rigid assembly of 2D MoS_2 nanocrystals, preserving the morphology of the original single crystals (Figure 1F and Figure S3). Despite severe compositional and structural differences between the 0D molecular polysulfide and the layered MoS_2 and the large amount of escaping gaseous species (H_2O, NH_3, H_2S, and sulfur), according to eq 1, it is truly remarkable that the conversion of hydrous $(NH_4)_2[Mo_3S(S_2)_6]\cdot H_2O$ to MoS_2 retains the bulk morphology inherited from the host crystal (Figure 1F).

$$(NH_4)_2Mo_3S_{13}H_2O \xrightarrow[\sim 170\ ^\circ C]{-H_2O} (NH_4)_2Mo_3S_{13} \xrightarrow[\sim 300\ ^\circ C]{-2NH_3+H_2S} [Mo_3S_{12}] \rightarrow 3MoS_2 \quad (1)$$

Thus, the single crystals of $(NH_4)_2[Mo_3S(S_2)_6]\cdot H_2O$ afford a robust template for the growth nanocrystalline MoS_2 without the crystal "exploding" from the violent expulsion of gases during the conversion (Figure S2). We could hypothesize the phenomena as the decomposition proceeds from hydrous to anhydrous $(NH_4)_2Mo_3S_{13}$ which subsequently can undergo further degradation by the liberation of NH_3 while the H^+ ion can act as counterions to charge balance and may from a one-dimensional chain. Further heating loses H_2S and S along with a simultaneous and very fast diffusion of the atoms Mo and S to form thermodynamically stable a two-dimensional structure of MoS_2. Therefore, the underlying reason may be the details of the parent crystal structure of $(NH_4)_2Mo_3S_{13}\cdot H_2O$ which may allow facile escape of gas molecule and thus reveal the isomorphic structure of the host crystal. SEM images show the presence of nanoscale cracks and pores which originate from the escape of gaseous species as indicated by eq 1. Despite these cracks and pores, the pseudocrystals of the MoS_2 ensembles are found to be nearly mechanically as stable and sustain upon general handling in the lab. Such mechanical stability could be the result of the formation of interlocking assembly of the aggregated nanocrystallites that themselves interact and define a 3D porous matrix. The porosity in the pseudocrystals was further validated with surface area measurements, giving ∼18 m^2/g, where the adsorption average pore width by BET is 264.5 Å and pore volume is 0.12 cm^3/g for the porous bulk crystals of MoS_2 prepared at 450 °C (heating rate 150 °C/h for ramp up and down and soaked for 2 h) (Figure 1G, quantity of absorbed gas, q, against relative pressure, ρ). This value is higher than the 13 m^2/g, which has been reported for the thermal decomposition of similar precursor at 400 °C.[41] However, ultrasonic pyrolysis of $(NH_4)_2MoS_4$ to MoS_2 without template led to BET surface area of 20−40 m^2/g, but in the presence of SiO_2 template this synthesis procedure led to a maximum surface area of 250 m^2/g.[42]

The rigidity of the nanocrystal assemblies allowed electrical resistivity measurements to be conducted on the entire porous pseudocrystals obtained at 450 and 600 °C (heating rate 15 °C/m, soaking time 1 h) (see Figure 1H). Relatively low resistivities, $\rho \sim 6.36 \times 10^3$ Ω·cm (conductivity, $\sigma \sim 1.58 \times 10^{-4}$ S cm^{-1}) and $\rho \sim 5.46 \times 10^4$ Ω·cm (conductivity, $\sigma \sim 1.83 \times 10^{-5}$ S cm^{-1}) were measured for the 450 and 600 °C MoS_2, respectively. These results show the electrical conductivity of 450 °C samples is approximately 1 order magnitude higher than that of the 600 °C samples. This is consistent with a smaller average particle size and better electrical connectivity of the particles. Higher temperature could also lead to directional diffusion of the atoms at certain grain boundaries, resulting in an increase of the density of pores in the bulk pseudocrystal. Interestingly, the electrical conductivities of such porous pseudosingle crystals exhibit very close to the value obtained for single bulk crystals of MoS_2 along the c-axis ($\sigma \sim 4.6 \times 10^{-4}$ S cm^{-1}).[43] This finding clearly suggests that despite the high density of pores the aggregated MoS_2 nanoparticles form a 3D network throughout the pseudosingle crystal. In addition, such solid-state conversion leads to high crystal quality of the MoS_2 nanocrystals, and their conjoining feature allows facile charge transport across the pseudomorph crystals. The Hall resistance of the porous bulk pseudomorph crystal obtained at 450 °C was measured at 300 K, showing n-type conduction (Figure S4). The nominal carrier density of electrons is $n = (1.5 \pm 0.2) \times 10^{14}$ cm^{-3} with carrier mobility of 7 ± 1 $cm^2/(V\ s)$.

The sizes, shapes, morphologies, and orientations of the MoS_2 nanocrystallites inside the pseudocrystals were studied as a function of processing temperature, ramp rate, and annealing duration. The nanocrystallites of MoS_2 were then studied by transmission electron microscopy (TEM), scanning electron

DOI: 10.1021/acs.chemmater.8b01247
Chem. Mater. 2018, 30, 3847−3853

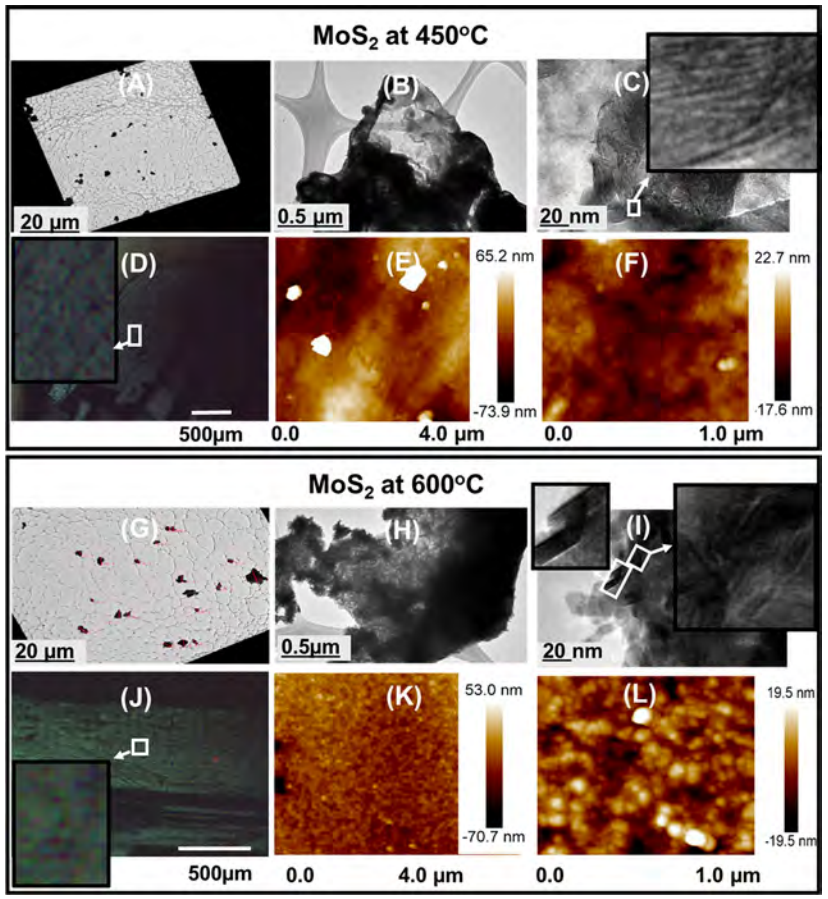

Figure 2. TEM and AFM images of the MoS_2 synthesized at 450 and 600 °C. (A) TEM shows chunky aggregated MoS_2 particles represented by black small objects, obtained from the sample synthesized at 450 °C after ultrasonication. (B) TEM image of MoS_2 does not show discrete grains. (C) TEM reveals "edge-on" view showing features of the aggregated nanocrystals; inset shows disordered stacking and presence of dislocation in the MoS_2. (D) Optical image of the pseudocrystal of MoS_2 obtained at 450 °C captured by AFM; inset shows rough and porous surface of the pseudocrystal. (E, F) AFM images at different magnification exhibiting the irregular morphology of MoS_2. (G) TEM image of aggregated MoS_2 nanoparticles represented by black small objects, obtained from the sample synthesized at 600 °C. (H) TEM image of MoS_2 shows evidence of the formation of individual grains. (I) Low-magnification TEM image shows disordered "edge-on" features in the MoS_2 with stacking of the 6−12 layer of basal planes with edge length up to ∼40 nm; inset show ordered (left) and disordered (right) features of the crystallites. (J) Optical images of the bulk MoS_2 crystal captured by AFM; inset shows rough and porous surface the pseudocrystal. (K, L) Different magnifications reveal the spherical-like morphology of MoS_2 with estimated particle size ∼30 to ∼50 nm.

microscopy (SEM), and atomic force microscopy (AFM) (Figures 2 and 3). Single crystals of $(NH_4)_2[Mo_3S(S_2)_6]\cdot H_2O$ were heated in an evacuated closed silica tube to 450, 600, 800, and 1000 °C with a ramp rate of 15 °C/m and soaked at the respective temperature for 1 h. Subsequently, the empty end of the tube was quenched in water in order to condense the evolved gaseous species and to minimize their adsorption on to the surface of the MoS_2 crystallites. For the TEM analysis, pseudocrystals of MoS_2 were sonicated in EtOH for 2 h to release the particles.

The TEM showed the presence of a highly disorderred aggregrate of nanocryatlline MoS_2 at 450 and 600 °C (Figures 2A−C and 2G−I). High-resolution TEM (HRTEM) images of the nanoaggregates show random 3D orientation and minimal stacking of the plate layers with no visible separation of the flakes. For the samples prepared at 450 °C, basal planes of the MoS_2 exhibit "edge on" features with occasional dislocations (Figure 2C, inset) which often result in surface curvature in the mesostructure of the crystallites. AFM clearly shows (Figure 2D−F) the irregular morphology of the MoS_2 nanoparticles which are aggregated. From AFM images (Figure 2F) the size of the nanoparticles can be estimated at ∼20 to ∼30 nm. Figure 2D shows the porous morphology of bulk pseudocrystals. The darker regions of the AFM images (Figure 2E,F) reveal the evidence of porosity created by the loss of volatile gaseous species during the transformation. At 600 °C, TEM images (Figure 2G,H) show no visual separation of MoS_2 flakes but reveal pronouced stacking featues of the layers along with disordered features of the lattices (Figure 2I, left inset). HRTEM estimates 6−12 layer stacking along the crystallographis *c*-axis with the edge length of crystallites being up to ∼40 nm. AFM images also show that the nanoparticles exhibit irregular morphologies with nanoparticles of diameter ranging from ∼30 to ∼50 nm (Figure 2K,L).

Higher processing temperatures (800 and 1000 °C) result in well-ordered stacking of the atoms extending along all the crystallographic directions with growth toward the thermodynamically preferable [002] planes becoming dominant (Figure 3A−D). TEM shows the presence of hexagonal plates which are easily separated upon sonication in EtOH. At 800 °C, the size of the hexagonal flakes range from ∼40 to ∼150 nm, with the majority of the particles exhibiting edge length between 50

DOI: 10.1021/acs.chemmater.8b01247
Chem. Mater. 2018, 30, 3847−3853

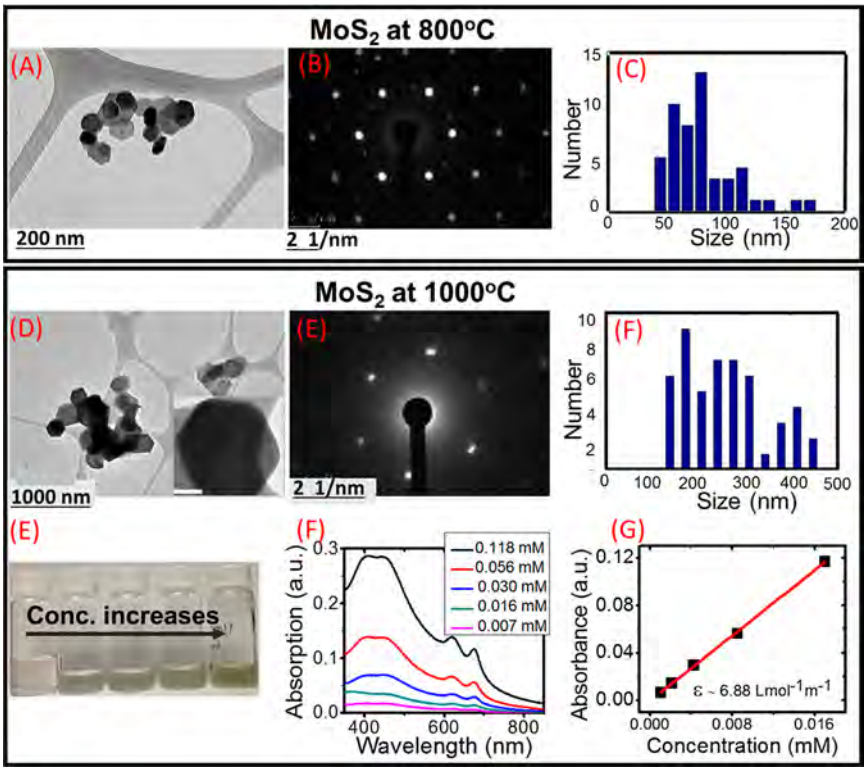

Figure 3. (A, D) TEM images of MoS_2 well-defined hexagonal flakes synthesized at 800 and 1000 °C. (B, E) Nanobeam diffraction pattern of the flakes; (E) obtained from inset flake of (D), white scale bar is 50 nm. (C, F) Statistical size distributions of the MoS_2 determined under TEM from the 800 and 1000 °C samples, respectively. (E) Solution-based exfoliated MoS_2 flakes obtained by centrifugation of the ultrasonicated products at various concentrations. (F) UV/vis absorption spectra of MoS_2 dispersed solutions, showing that intensity of the absorption spectra increases as a function of concentration. (G) Molar absorption coefficient, 6.88 L mol^{-1} m^{-1}, of MoS_2 solutions determined from absorption vs concentration plots.

and 100 nm (Figure 3C). The sizes of the particles become larger with increased temperature, and at 1000 °C the lateral size of the nanocrystals ranges from ~150 to ~500 nm (Figure 3E). This increase in size is the result of the merging of closely connected smaller crystallites which are fused by solid state diffusion of atoms at elevated temperature (Figure S5). The crystal pseudomorphs have mechanical integrity which supports the notion of sintered conjoining MoS_2 microcrystals. This is supported by the sharper PXRD patterns of the MoS_2 synthesized in the range 450−1000 °C at a heating rate 15 °C/m (Figure S6). It is important to mention that for Figure 1E the PXRD of MoS_2 was collected at high temperature (400−450 °C) during the *in situ* heating of $(NH_4)_2Mo_3S_{13}\cdot H_2O$, while the PXRD for the MoS_2 samples in Figure S6 were collected at room temperature. This accounts for the differences in intensity of the diffraction patterns between the two classes of samples; however, the probability of turbostratic stacking and differences in such based on different heating temperatures cannot be ruled out. The well-defined crystals obtained at 1000 °C can exfoliate in isopropanol by ultrasonication (Figure 3H−J). The UV/vis absorption spectra of the supernatant solution of the exfoliated MoS_2 nanosheets (Figure 3H) exhibit two pairs of bands: the first pair appears at 675 and 625 nm corresponding to the A and B excitons, while the second intense broad pair centered at 443 and 413 nm corresponds to the C and D excitonic transitions.[28,43,44] The molar extinction coefficient was calculated at ~6.8 L mol^{-1} m^{-1}. As expected, very similar absorption spectra were observed for the MoS_2 synthesized at 800 °C (Figure S7).

In addition to directing the morphology and size of the nanocrystals, the orientation of the crystallites within the template of the host polysulfide crystal can be controlled. For example, nanocrystals of MoS_2 from the host matrix of molybdenum polysulfides $(NH_4)_2Mo_3S_{13}\cdot H_2O$ were formed at 1000 °C with variable heating rates. A rate of 100 °C/h to 1000 °C with a soaking time of 1 h led to intact pseudocrystals composed of well-developed hexagonal plate-like crystallites orientated randomly (Figure 4A). The connectivity at the grain boundaries among the crystallites via fusion is the driving force behind the retention of the original crystal shape. In order to achieve a very slow escape of the gaseous species from the host structure, we heated the precursor crystals at a very slow heating rate, 20 °C/h, to 1000 °C and stayed at this temperature for 6 h. This experiment resulted in pseudocrystals of MoS_2 nanoparticles with different length scales (nanometers to micrometers scale) as well as highly oriented [002] lattice planes of MoS_2 extending along the surface of the host crystal (Figure 4B). This observation could suggest that slower heating rate allows for slower escape of the gaseous species from the host structure, probably creating a common channel to liberate gases, and this eventually could affect the orientation of the crystallites in the host crystal.

This new synthesis strategy for agglomerated assemblies of nanocrystals with specific bulk crystal shapes is a unique route toward nanoscale MoS_2 because it permits much higher processing temperatures and short times while limiting size growth. In addition to this unconventional synthetic technique for porous ensembles of MoS_2, meticulous control over the

DOI: 10.1021/acs.chemmater.8b01247
Chem. Mater. 2018, 30, 3847−3853

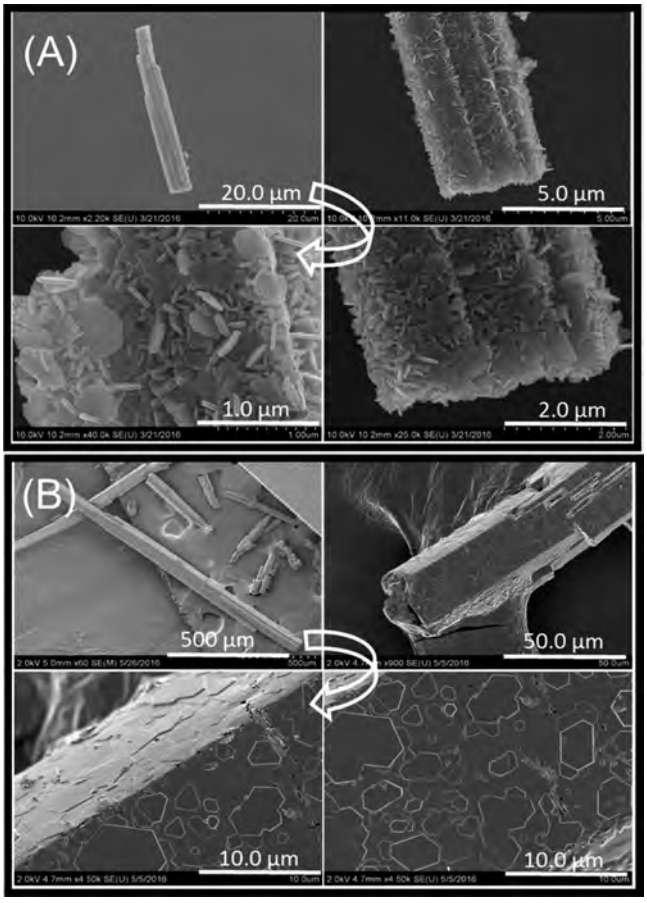

Figure 4. Orientation of the crystallites in the pseudocrystal of MoS_2 obtained 1000 °C. (A) Random orientations of the flakes of MoS_2 distributed in structure of host crystal acting as template, obtained at a heating rate of 100 °C/h; the curved arrows indicate different pictures of a same crystal at different magnification. (B) MoS_2 flakes cover the surface of the pseudomorphic crystals, obtained at a very slow heating rate of 20 °C/h.

hierarchical assemblies of the nanocrystals across a range length scales, morphologies, and orientations (within a predetermined template in the form of a starting crystal shape) has not been previously demonstrated.

CONCLUSION

In conclusion, crystals of the molecular compound $(NH_4)_2Mo_3S_{13}·H_2O$ are excellent precursors to nanocrystals of MoS_2 as they allow the orderly escape of gases during thermal decomposition to yield an ensemble of agglomerated nanocrystals that retain the shape of the original molecular crystal. Because of the constrained growth conditions in the solid state, the growth of particles is confined in space and can be controlled using the heating rate, soaking time, and temperature. These rigid nanocrystal assemblies show electrical conductivity similar to the bulk single crystal MoS_2 which exhibit n-type behavior with electron carrier concentration of 1.5×10^{14} cm^{-3} and mobility of 7 $cm^2/(V\ s)$. This work elucidates how a chemically homogeneous polysulfide precursor undergoes a transformation from single crystals to isomorphic pseudocrystals of assembled nanoparticles in a porous network. This may enable new opportunities for the synthesis of porous pseudo-single crystals with controllable sizes, shapes, and orientations of the constituent nanocrystals in constrained growth conditions from similar kinds of molecular precursors. This could be a powerful synthesis strategy for nanomaterials that could be rapidly prepared at higher temperatures and produce more perfect nanomaterials with fewer defects.

ASSOCIATED CONTENT

Supporting Information

The Supporting Information is available free of charge on the ACS Publications website at DOI: 10.1021/acs.chemmater.8b01247.

Experimental section and Figures S1−S7 (PDF)
Crystallographic files of $(NH_4)_2Mo_3S_{13}·H_2O$ and $(NH_4)_2Mo_3S_{13}$ (CIF)

AUTHOR INFORMATION

Corresponding Author

*E-mail: m-kanatzidis@northwestern.edu (M.G.K.).

ORCID

Saiful M. Islam: 0000-0001-8518-1856
Yihui He: 0000-0002-1057-6826
Abhishek Banerjee: 0000-0003-4552-4820
Yuan Li: 0000-0001-7452-1149
Shulan Ma: 0000-0002-8326-3134
Vinayak P. Dravid: 0000-0002-6007-3063
Mercouri G. Kanatzidis: 0000-0003-2037-4168

Notes

The authors declare no competing financial interest.

ACKNOWLEDGMENTS

S.M.I., M.G.K., V.P.D., and M.G. thank the National Science Foundation for Grant DMR-1720139 (MRSEC program at the Materials Research Center) and Grant 1708254. J.D.C. is supported by the Department of Defense through the National Defense Science and Engineering Fellowship (NDSEG) Program. J.D.C. also gratefully acknowledges support from the Ryan Fellowship and the IIN. SEM, EDS, TEM, Raman, and XPS analyses were performed at the EPIC facility of the NUANCE Center at Northwestern University, supported by NSF-NSEC, NSF-MRSEC, Keck Foundation, the State of Illinois, and Northwestern University. M.G. acknowledges support from AFOSR FA9550-15-1-0247.

REFERENCES

(1) Lauritsen, J. V.; Kibsgaard, J.; Helveg, S.; Topsoe, H.; Clausen, B. S.; Laegsgaard, E.; Besenbacher, F. Size-dependent structure of MoS_2 nanocrystals. *Nat. Nanotechnol.* **2007**, *2*, 53−58.

(2) Gong, Y.; Lin, J.; Wang, X.; Shi, G.; Lei, S.; Lin, Z.; Zou, X.; Ye, G.; Vajtai, R.; Yakobson, B. I.; Terrones, H.; Terrones, M.; Tay, B. K.; Lou, J.; Pantelides, S. T.; Liu, Z.; Zhou, W.; Ajayan, P. M. Vertical and in-plane heterostructures from WS_2/MoS_2 monolayers. *Nat. Mater.* **2014**, *13*, 1135−1142.

(3) Li, H.; Tsai, C.; Koh, A. L.; Cai, L.; Contryman, A. W.; Fragapane, A. H.; Zhao, J.; Han, H. S.; Manoharan, H. C.; Abild-Pedersen, F.; Norskov, J. K.; Zheng, X. Activating and optimizing MoS_2 basal planes for hydrogen evolution through the formation of strained sulphur vacancies. *Nat. Mater.* **2016**, *15*, 48−53.

(4) Sangwan, V. K.; Jariwala, D.; Kim, I. S.; Chen, K. S.; Marks, T. J.; Lauhon, L. J.; Hersam, M. C. Gate-tunable memristive phenomena mediated by grain boundaries in single-layer MoS_2. *Nat. Nanotechnol.* **2015**, *10*, 403−406.

(5) Goldstein, A. N.; Echer, C. M.; Alivisatos, A. P. Melting in semiconductor nanocrystals. *Science* **1992**, *256*, 1425−1427.

DOI: 10.1021/acs.chemmater.8b01247
Chem. Mater. 2018, 30, 3847−3853

(6) Wang, Y.; Herron, N. Nanometer-Sized Semiconductor Clusters - Materials Synthesis, Quantum Size Effects, and Photophysical Properties. *J. Phys. Chem.* **1991**, *95*, 525−532.
(7) Peng, Y. Y.; Meng, Z. Y.; Zhong, C.; Lu, J.; Yu, W. C.; Jia, Y. B.; Qian, Y. T. Hydrothermal synthesis and characterization of single-molecular-layer MoS_2 and $MoSe_2$. *Chem. Lett.* **2001**, *30*, 772−773.
(8) Matte, H. S. S. R.; Gomathi, A.; Manna, A. K.; Late, D. J.; Datta, R.; Pati, S. K.; Rao, C. N. R. MoS_2 and WS_2 Analogues of Graphene. *Angew. Chem., Int. Ed.* **2010**, *49*, 4059−4062.
(9) Li, Q.; Newberg, J. T.; Walter, E. C.; Hemminger, J. C.; Penner, R. M. Polycrystalline molybdenum disulfide (2H-MoS_2) nano- and microribbons by electrochemical/chemical synthesis. *Nano Lett.* **2004**, *4*, 277−281.
(10) Bar-Sadan, M.; Enyashin, A. N.; Gemming, S.; Popovitz-Biro, R.; Hong, S. Y.; Prior, Y.; Tenne, R.; Seifert, G. Structure and stability of molybdenum sulfide fullerenes. *J. Phys. Chem. B* **2006**, *110*, 25399−25410.
(11) Enyashin, A. N.; Gemming, S.; Bar-Sadan, M.; Popovitz-Biro, R.; Hong, S. Y.; Prior, Y.; Tenne, R.; Seifert, G. Structure and stability of molybdenum sulfide fullerenes. *Angew. Chem., Int. Ed.* **2007**, *46*, 623−627.
(12) Parilla, P. A.; Dillon, A. C.; Jones, K. M.; Riker, G.; Schulz, D. L.; Ginley, D. S.; Heben, M. J. The first true inorganic fullerenes? *Nature* **1999**, *397*, 114−114.
(13) Ouerfelli, J.; Srivastava, S. K.; Bernede, J. C.; Belgacem, S. Effect of microwaves on synthesis Of MoS_2 and WS_2. *Vacuum* **2008**, *83*, 308−312.
(14) Vollath, D.; Szabo, D. V. Synthesis of nanocrystalline MoS_2 and WS_2 in a microwave plasma. *Mater. Lett.* **1998**, *35*, 236−244.
(15) Vanchura, B. A.; He, P. G.; Antochshuk, V.; Jaroniec, M.; Ferryman, A.; Barbash, D.; Fulghum, J. E.; Huang, S. D. Direct synthesis of mesostructured lamellar molybdenum disulfides using a molten neutral n-alkylamine as the solvent and template. *J. Am. Chem. Soc.* **2002**, *124*, 12090−12091.
(16) Afanasiev, P.; Rawas, L.; Vrinat, M. Synthesis of dispersed Mo sulfides in the reactive fluxes containing liquid sulfur and alkali metal carbonates. *Mater. Chem. Phys.* **2002**, *73*, 295−300.
(17) Helveg, S.; Lauritsen, J. V.; Laegsgaard, E.; Stensgaard, I. I.; Norskov, J. K.; Clausen, B. S.; Topsoe, H.; Besenbacher, F. Atomic-scale structure of single-layer MoS_2 nanoclusters. *Phys. Rev. Lett.* **2000**, *84*, 951−954.
(18) Najmaei, S.; Liu, Z.; Zhou, W.; Zou, X.; Shi, G.; Lei, S.; Yakobson, B. I.; Idrobo, J. C.; Ajayan, P. M.; Lou, J. Vapour phase growth and grain boundary structure of molybdenum disulphide atomic layers. *Nat. Mater.* **2013**, *12*, 754−759.
(19) Lee, Y. H.; Zhang, X. Q.; Zhang, W.; Chang, M. T.; Lin, C. T.; Chang, K. D.; Yu, Y. C.; Wang, J. T.; Chang, C. S.; Li, L. J.; Lin, T. W. Synthesis of large-area MoS_2 atomic layers with chemical vapor deposition. *Adv. Mater.* **2012**, *24*, 2320−2325.
(20) Liu, K. K.; Zhang, W. J.; Lee, Y. H.; Lin, Y. C.; Chang, M. T.; Su, C.; Chang, C. S.; Li, H.; Shi, Y. M.; Zhang, H.; Lai, C. S.; Li, L. J. Growth of Large-Area and Highly Crystalline MoS_2 Thin Layers on Insulating Substrates. *Nano Lett.* **2012**, *12*, 1538−1544.
(21) Zhan, Y. J.; Liu, Z.; Najmaei, S.; Ajayan, P. M.; Lou, J. Large-Area Vapor-Phase Growth and Characterization of MoS_2 Atomic Layers on a SiO_2 Substrate. *Small* **2012**, *8*, 966−971.
(22) Cain, J. D.; Shi, F.; Wu, J.; Dravid, V. P. Growth Mechanism of Transition Metal Dichalcogenide Monolayers: The Role of Self-Seeding Fullerene Nuclei. *ACS Nano* **2016**, *10*, 5440−5445.
(23) Diemann, E.; Mueller, A.; Aymonino, P. J. The thermal decomposition of $(NH_4)_2Mo_3S_{13}.H_2O.nH_2O$. *Z. Anorg. Allg. Chem.* **1981**, *479*, 191−198.
(24) Prasad, T. P.; Diemann, E.; Mueller, A. Thermal Decomposition of $(NH_4)_2MoO_2S_2$, $(NH_4)_2MoS_4$, $(NH_4)_2WO_2S_2$ and $(NH_4)_2WS_4$. *J. Inorg. Nucl. Chem.* **1973**, *35*, 1895−1904.
(25) Kang, K.; Xie, S. E.; Huang, L. J.; Han, Y. M.; Huang, P. Y.; Mak, K. F.; Kim, C. J.; Muller, D.; Park, J. High-mobility three-atom-thick semiconducting films with wafer-scale homogeneity. *Nature* **2015**, *520*, 656−660.
(26) Shomalian, K.; Bagheri-Mohagheghi, M. M.; Ardyanian, M. Synthesis and characterization of porous nanoparticles of molybdenum sulfide (MoS_2) chalcogenide semiconductor prepared by polymerizing-complexing sol−gel method. *J. Mater. Sci.: Mater. Electron.* **2017**, *28*, 14331.
(27) Li, N.; Chai, Y.; Dong, B.; Liu, B.; Guo, H.; liu, C. Preparation of porous MoS_2 viasol-gel route using $(NH_4)_2Mo_3S_{13}$ as Precourosr. *Mater. Lett.* **2012**, *88*, 112−115.
(28) Coleman, J. N.; Lotya, M.; O'Neill, A.; Bergin, S. D.; King, P. J.; Khan, U.; Young, K.; Gaucher, A.; De, S.; Smith, R. J.; Shvets, I. V.; Arora, S. K.; Stanton, G.; Kim, H. Y.; Lee, K.; Kim, G. T.; Duesberg, G. S.; Hallam, T.; Boland, J. J.; Wang, J. J.; Donegan, J. F.; Grunlan, J. C.; Moriarty, G.; Shmeliov, A.; Nicholls, R. J.; Perkins, J. M.; Grieveson, E. M.; Theuwissen, K.; McComb, D. W.; Nellist, P. D.; Nicolosi, V. Two-Dimensional Nanosheets Produced by Liquid Exfoliation of Layered Materials. *Science* **2011**, *331*, 568−571.
(29) Zeng, Z. Y.; Yin, Z. Y.; Huang, X.; Li, H.; He, Q. Y.; Lu, G.; Boey, F.; Zhang, H. Single-Layer Semiconducting Nanosheets: High-Yield Preparation and Device Fabrication. *Angew. Chem., Int. Ed.* **2011**, *50*, 11093−11097.
(30) Wang, X.; Feng, H.; Wu, Y.; Jiao, L. Controlled synthesis of highly crystalline MoS_2 flakes by chemical vapor deposition. *J. Am. Chem. Soc.* **2013**, *135*, 5304−5307.
(31) Uzcanga, I.; Bezverkhyy, I.; Afanasiev, P.; Scott, C.; Vrinat, M. Sonochemical preparation of MoS_2 in aqueous solution: Replication of the cavitation bubbles in an inorganic material morphology. *Chem. Mater.* **2005**, *17*, 3575−3577.
(32) Tian, Y.; He, Y.; Zhu, Y. F.; Wang, W. Hydrothermal synthesis of MoS_2 and its lubricating properties. *Acta Phys-Chim. Sin.* **2003**, *19*, 1044−1048.
(33) Tian, Y. M.; Liu, Y. H.; Sheng, Y.; Zhao, J. Z.; Jiang, Y. Q.; Wang, Z. C. Facile route to synthesis of MoS_2 nanorods additive. *Abstr. Pap. Am. Chem. Soc.* **2005**, *229*, U913−U913.
(34) Guo, B.; Yu, K.; Li, H.; Song, H.; Zhang, Y.; Lei, X.; Fu, H.; Tan, Y.; Zhu, Z. Hollow Structured Micro/Nano MoS_2 Spheres for High Electrocatalytic Activity Hydrogen Evolution Reaction. *ACS Appl. Mater. Interfaces* **2016**, *8*, 5517−5525.
(35) Massey, A. T.; Gusain, R.; Kumari, S.; Khatri, O. P. Hierarchical Microspheres of MoS_2 Nanosheets: Efficient and Regenerative Adsorbent for Removal of Water-Soluble Dyes. *Ind. Eng. Chem. Res.* **2016**, *55*, 7124−7131.
(36) Zelenski, C. M.; Dorhout, P. K. Template synthesis of near-monodisperse microscale nanofibers and nanotubules of MoS_2. *J. Am. Chem. Soc.* **1998**, *120*, 734−742.
(37) Muller, A.; Sarkar, S.; Bhattacharyya, R. G.; Pohl, S.; Dartmann, M. Directed Synthesis of $[Mo_3S_{13}]^{2-}$, an Isolated Cluster Containing Sulfur-Atoms in 3 Different States of Bonding. *Angew. Chem., Int. Ed. Engl.* **1978**, *17*, 535−535.
(38) Moulder, J. F.; Stickle, W. F.; Sohol, P. E.; Bomben, K. D. *Handbook of X-ray Photoelectron Spectroscopy*; Physical Electronics, Inc.: Eden Prairie, MN, 1995.
(39) Kibsgaard, J.; Jaramillo, T. F. Molybdenum Phosphosulfide: An Active, Acid-Stable, Earth-Abundant Catalyst for the Hydrogen Evolution Reaction. *Angew. Chem., Int. Ed.* **2014**, *53*, 14433−14437.
(40) Li, H.; Zhang, Q.; Yap, C. C. R.; Tay, B. K.; Edwin, T. H. T.; Olivier, A.; Baillargeat, D. From Bulk to Monolayer MoS_2: Evolution of Raman Scattering. *Adv. Funct. Mater.* **2012**, *22*, 1385−1390.
(41) Li, N.; Chai, Y.; Dong, B.; Liu, B.; Guo, H.; Liu, C. Preparation of porous MoS_2 via a sol−gel route using $(NH_4)_2Mo_3S_{13}$ as precursor. *Mater. Lett.* **2012**, *88*, 112−115.
(42) Skrabalak, S. E.; Suslick, K. S. Porous MoS2 Synthesized by Ultrasonic Spray Pyrolysis. *J. Am. Chem. Soc.* **2005**, *127*, 9990−9991.
(43) Evans, B. L.; Young, P. A. Optical Absorption and Dispersion In Molybdenum Disulphide. *Proc. R. Soc. London, Ser. A* **1965**, *284*, 402−422.
(44) Wilcoxon, J. P.; Newcomer, P. P.; Samara, G. A. Synthesis and optical properties of MoS_2 and isomorphous nanoclusters in the quantum confinement regime. *J. Appl. Phys.* **1997**, *81*, 7934−7944.

DOI: 10.1021/acs.chemmater.8b01247
Chem. Mater. 2018, 30, 3847−3853

Modular time division multiplexer: Efficient simultaneous characterization of fast and slow transients in multiple samples

Stephan D. Kim,[1] Jiajun Luo,[1] D. Bruce Buchholz,[2] R. P. H. Chang,[2] and M. Grayson[1]
[1]*Department of Electrical Engineering and Computer Science, Northwestern University, Evanston, Illinois 60208, USA*
[2]*Department of Materials Science and Engineering, Northwestern University, Evanston, Illinois 60208, USA*

(Received 5 February 2016; accepted 29 August 2016; published online 30 September 2016)

A modular time division multiplexer (MTDM) device is introduced to enable parallel measurement of multiple samples with both fast and slow decay transients spanning from millisecond to month-long time scales. This is achieved by dedicating a single high-speed measurement instrument for rapid data collection at the start of a transient, and by multiplexing a second low-speed measurement instrument for slow data collection of several samples in parallel for the later transients. The MTDM is a high-level design concept that can in principle measure an arbitrary number of samples, and the low cost implementation here allows up to 16 samples to be measured in parallel over several months, reducing the total ensemble measurement duration and equipment usage by as much as an order of magnitude without sacrificing fidelity. The MTDM was successfully demonstrated by simultaneously measuring the photoconductivity of three amorphous indium-gallium-zinc-oxide thin films with 20 ms data resolution for fast transients and an uninterrupted parallel run time of over 20 days. The MTDM has potential applications in many areas of research that manifest response times spanning many orders of magnitude, such as photovoltaics, rechargeable batteries, amorphous semiconductors such as silicon and amorphous indium-gallium-zinc-oxide. *Published by AIP Publishing.* [http://dx.doi.org/10.1063/1.4962702]

I. INTRODUCTION

Experimental characterizations of systems with both long and short response times pose significant experimental challenges. Regarding the longer time scales, such systems typically require continuous measurement. And when comparison of several samples is necessary, the resulting measurement can become extremely time consuming and equipment intensive, requiring either continuous use of a large number of dedicated measurement instruments or prolonged sequential measurements with one instrument. For example, dye-sensitized solar cells (DSSCs) require long-term stability characterization over yearlong time scales before they can be implemented as low-cost photovoltaics.[1–3] Lithium-ion batteries (LIBs) suffer "calendar aging," or degradation during energy storage, requiring lengthy studies.[4–7]

In addition to measurement difficulties associated with long time scales, many such systems also exhibit fast transients that are equally important to characterize. The combined fast and slow time scales pose an additional measurement challenge: The measurement interval should be short at the start to accurately characterize the fast response, but it should be long thereafter to minimize the accumulation of redundant data. Relaxation of non-equilibrium defect concentrations in amorphous semiconductors is one example of a system which relaxes with rapid as well as slow time scales.[8,9] Moreover, amorphous indium-gallium-zinc-oxide (a-IGZO), a semiconductor already in use in industry with immense potential in flexible and transparent devices, exhibits rapid and slow photoconductivity transients during and after ultraviolet (UV) illumination, limiting device robustness and utility. Data from previous experiments show that this photoconductivity is characterized by time scales ranging from $\tau > 10^{-2}$ s to $\tau < 10^{6}$ s.[10–12]

The modular time division multiplexer (MTDM) is introduced to implement simultaneous measurements of multiple samples in parallel which exhibit transients with relaxation rates that span orders of magnitude. The multiplexing measurement strategy is already recognized as a method to increase data collection efficiency in several fields of study, such as nanoscale magnetic resonance imaging (nanoMRI).[14] The MTDM measures initially fast and eventually slow time scales, first in a time-sequenced and subsequently in a multiplexed manner that continuously increases the time interval for data collection in the dedicated mode in response to the sample behavior. The result significantly reduces the overall measurement duration for multiple samples and the overuse of redundant equipment. The MTDM is a high-level design concept that can be realized in multiple ways, including commercial switching systems. Using a low cost implementation of MTDM described here and a measurement computer, only two measurement instruments are initially needed to measure transients in up to 16 samples at once and only one measurement instrument is required for the majority of the measurement duration. This paper will explain both the circuit design of the MTDM and its low cost implementation as well as demonstrate the method for MTDM to measure transient photoconductivity. The transient photoconductivity of several a-IGZO thin films are studied as an example of parallel characterization of samples with both rapid and slow relaxation time scales.

II. SYSTEM DESIGN OF MTDM

Figure 1 shows the system design of the MTDM. It has two different modes, which are labeled as the dedicated mode and the multiplexed mode, respectively. The dedicated mode measures one sample with a fast transient using a single measurement instrument at short time-intervals. The multiplexed mode measures the remaining multiple samples during their slow response phase by multiplexing a second measurement instrument among these various samples at longer time intervals. Each mode uses one measurement instrument. Thus a total of two measurement instruments are required to measure an arbitrarily large number of samples with high fidelity.

While we will include a specific multiplexer circuit for completeness as well as to provide a cost-effective implementation of this method, one can also use commercial multiplexers in the fashion described to achieve the same MTDM operation. Commercially available units at the time of this publication include Keithley 3706A, Agilent 34901A, and Stanford Research Systems SIM925.

To summarize the overall method, multiple samples are first connected in the multiplexed mode before measurement. Then a single sample is switched to the dedicated mode in anticipation of measuring a fast transient, while other samples remain in the multiplexed mode. While measuring the fast transient of the sample, the dedicated mode calculates the measurement time interval based on the relaxation rate as measured from the most recent data points. The time interval will be increased with successive measurements as the rate of relaxation slows down. Once the measurement time interval of the sample exceeds a fixed threshold, the dedicated mode for that sample is terminated, and the sample is transferred to the multiplexed mode. The threshold measurement time interval for multiplexed mode is determined according to the number of total samples being multiplexed. Other samples follow the same procedure, one at a time. After the fast transients of all samples are measured, all samples will be measured in the multiplexed mode for the remainder of the transient, and the dedicated mode instrument can be removed from the system so that only one instrument is required for the remainder of the measurement.

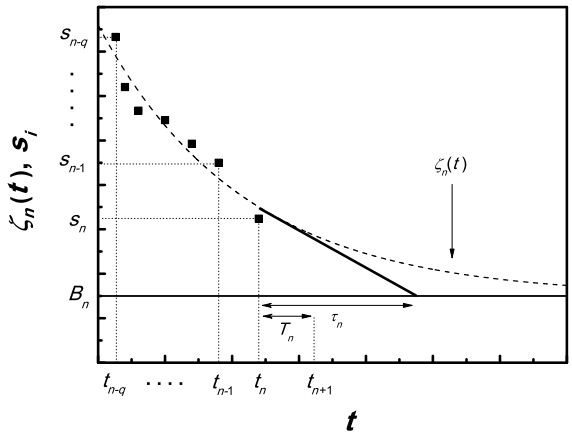

FIG. 2. Demonstration of least square fit method for determining the instantaneous decay constant τ_n. The dashed line represents the best fit $\xi_n(t) = A_n e^{-t/\tau_n} + B_n$ when $t = t_n$. The best fit line $\xi_n(t)$ was approximated from the most recent q data points. The black squares represent experimental data s_i. The decay time constant τ_n at the nth measurement is derived from minimizing the error in $\xi_n(t)$ in a fit to the data. The measurement interval at nth measurement event is set to $T_n = \tau_n / R$, where R is the time constant sub-resolution and is the number of measurements desired within the single τ_n. The next desired measurement event is set to $t_{n+1} = t_n + T_n$.

A. Dynamic measurement time interval for decaying signal

In order to determine crossover time scales while measuring sample transients, it is important to identify how rapidly the sample is decaying at any given instant. As shown in Fig. 2, within a brief interval the signal of a sample $s(t)$ can be approximated as an exponential decay $\xi(t) = Ae^{-t/\tau(t)} + B$

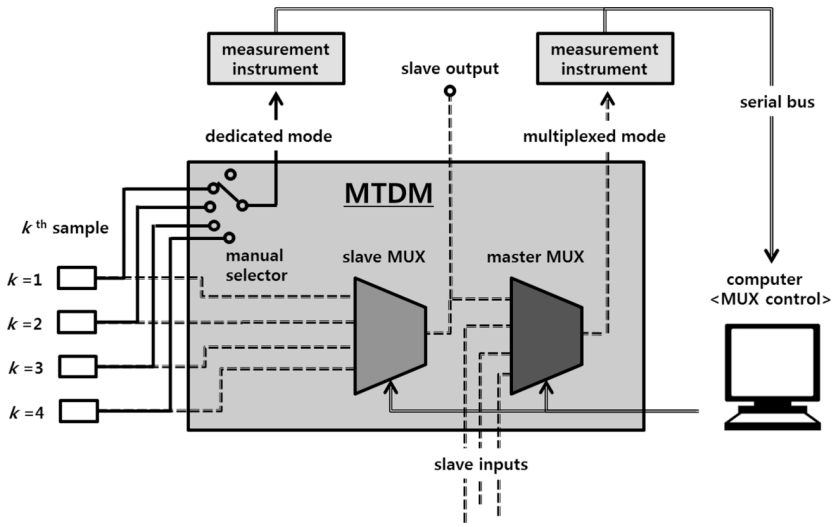

FIG. 1. System design of the modular time division multiplexer (MTDM) unit. Solid lines symbolize connections relevant to the dedicated mode. Dashed lines represent connections relevant to the multiplexed mode. The dedicated mode measures the fast transient of a single sample, here illustrated for sample index $k = 1$. The multiplexed mode measures the remaining multiple samples $k = 2$, 3, and 4 with slower transients. Two measurement instruments are used to measure four samples, one each for the dedicated mode and the multiplexed mode, respectively. The dedicated mode instrument can be removed, once all of the fast transient of all samples have been measured.

with a corresponding decay constant $\tau(t)$. The exponential decay approximation is good enough to provide a characteristic time scale for any generic decay that might be encountered. The experimental signal to be measured $s(t)$ is more appropriately expressed in discrete form to represent the discrete data set measured at times t_n, as indexed by n,

$$s_n = s(t_n). \tag{1}$$

The decay time constant $\tau(t)$ associated with each discrete data point is then,

$$\tau_n = \tau(t_n). \tag{2}$$

The discrete τ_n at nth measurement event is obtained from an exponential best fit line, $\xi_n(t) = A_n e^{-t/\tau_n} + B_n$, that is generated based on q previous data points. The users decide q at their discretion to average out noise in the signal. The recommended minimum value for q is $q = 10$, and the present experimental test was implemented with $q = 50$. The best fit is determined with a simple software algorithm on the computer that controls the multiplexers of the MTDM in Fig. 1.

In the present implementation, the best fit line $\xi_n(t)$ is derived using the least square fit method.[13] The sum of squared residuals L is defined as

$$L = \sum_{i=n-q}^{n} [(A_n e^{-t_i/\tau_n} + B_n) - s_i]^2, \tag{3}$$

whereby $i = \{n-q, n-q+1, \ldots, n\}$ indexes the q most recent data points before the time $t = t_n$. The best fit for the decay constant τ_n can be determined by minimizing L with respect to A_n, B_n, and τ_n and then using the resulting value for τ_n.

In order to most effectively characterize the decay response while minimizing redundancy in slowly varying transients, a measurement instrument needs to take multiple measurements within τ_n. The desired number of measurement events within a decay constant τ_n is defined as the time constant sub-resolution R. The minimum recommended value for R is $R = 20$, and the present data was collected with $R = 100$. The dynamic measurement interval T_n is then,

$$T_n = \frac{\tau_n}{R}. \tag{4}$$

On the other hand, estimating the local time constant using a linear fit requires a pre-assumption on the steady state value. A wrong assumption of the steady state value would cause a systematic overestimation or underestimation of the time constant.

As described in Secs. II B–II E, the MTDM will compare the continuously updated dynamic measurement interval T_n to several time scales and time constraints in the measurement system, and it will conduct measurements in the dedicated mode or multiplexed mode, accordingly.

B. Dedicated mode: Fast transients

The dedicated mode concentrates the measurement effort of one of the measurement instruments to a single sample for the sake of monitoring the fast part of the decay transient. As a result, the data flow from that sample measures the initial response at the fastest possible sampling rate which is subsequently slowed down in response to the sample's own behavior as set by the dynamic measurement time interval T_n (Section II A).

In a real experiment, the MTDM cannot accommodate arbitrarily short time intervals T_n due to limitations of the measurement instrument. The actual measurement interval of the MTDM is therefore defined as θ_n,

$$\theta_n = \max(T_n, \Theta_D), \tag{5}$$

where Θ_D is the shortest measurement interval possible, set by the slower of the measurement instrument speed or the communication protocol time between the computer and the instrument. Due to the decay characteristic, T_n increases over time. The time t_n when crossover from $\theta_n = \Theta_D$ to $\theta_n = T_n$ takes place, is called the dynamic interval crossover time,

$$t_n = t_D. \tag{6}$$

The manual selector in Fig. 1 shows a scenario where the sample with index $k = 1$ is connected to the dedicated mode in anticipation of measuring a rapid transient for that sample. Throughout measurements, all signals associated with the dedicated mode must be shielded with co-axial cables from the rest of the MTDM to prevent signal interference.

C. Multiplexed mode: Slow transients

The multiplexed mode utilizes the time division multiplexing technique (TDM) to measure multiple samples in parallel that all have sufficiently slow response times that their dynamic measurement time interval exceeds the multiplexing measurement cycle time required to measure all N samples under test. In the multiplexed mode, the actual measurement interval θ_n is set to $\theta_n = \Theta_M$, where Θ_M denotes the multiplexed mode time interval. This interval is set by the time it takes to cycle the multiplexed connection through all of the samples and return to the original sample as

$$\Theta_M = N \cdot \tau_s, \tag{7}$$

where N is the number of samples to be measured in parallel in the multiplexed mode. The stabilization time τ_s is the time that the measurement instrument takes to terminate the connection from the previous sample, establish a connection to the next sample of interest, and stabilize before making a reliable measurement. Each channel must be shielded to reduce interference with other channels. Using co-axial cables for signal transmission is one way to ensure shielding.

The multiplexed mode utilizes two designations of multiplexers — slave and master multiplexers — in anticipation of a hierarchical measurement of multiple MTDM units in parallel, as described in Section II D.

D. Multiplexer hierarchy: Integrated system of multiple MTDM units

The number of samples that can be measured with a single MTDM is limited by several factors, such as the number of throughputs of slave multiplexer IC and the space constraints of housing unit. Integrating multiple MTDM units modularly can overcome such limitations and allows parallel measurement of a scalable number of samples.

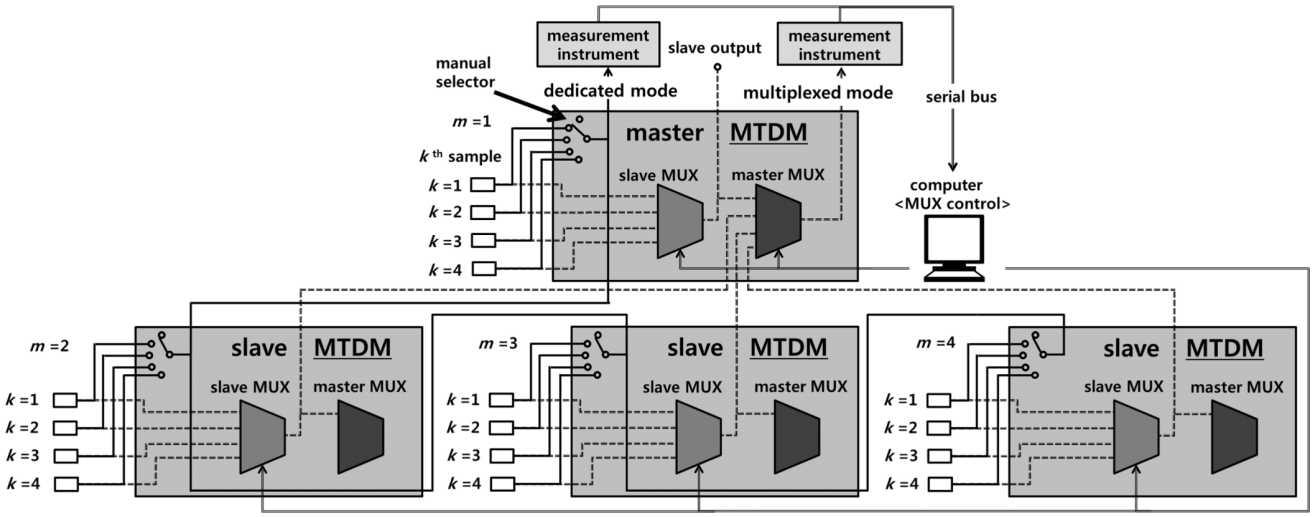

FIG. 3. Hierarchy of integrated modular time division multiplexer (MTDM) units. Multiple MTDM units can be integrated through the multiplexer hierarchy of several slave MTDM units and a single master MTDM unit. A MTDM unit containing a master multiplexer directly connected to the measurement device is called the master MTDM. Others are called slave MTDM units. This integration can scalably increase the number of measured samples. Note that all MTDM's have identical circuitry, so the master MUX's in the slave MTDM's remain unused.

Such integration also allows addition of new samples during ongoing measurements. In Fig. 3, multiple MTDM units are integrated by connecting the slave outputs of the slave MTDM units to the master multiplexer of the master MTDM. The measurement signal of a sample in the integrated system is indexed with superscripts,

$$s_n^{m,k}, \tag{8}$$

where the nth signal data point is from the kth sample of the mth MTDM unit in the integrated system of Fig. 3. When the measurement instrument needs to measure $s_n^{m,k}$ in the multiplexed mode, the computer commands the master multiplexer to index the signal from the slave multiplexer in the mth MTDM unit, and the computer commands the slave multiplexer to index the kth sample, ultimately connecting the measurement instrument to the desired sample.

The total number of samples that can be measured in the multiplexed mode, N in Eq. (7) is expressed as

$$N = M \cdot K \begin{cases} k = 1,2,\ldots,K \\ m = 1,2,\ldots,M \end{cases}, \tag{9}$$

where M is the total number of MTDM units in the integrated system and K is the total number of samples in one MTDM unit. $M = 4$ and $K = 4$ in the hierarchical example of Fig. 3.

E. Crossover from dedicated to multiplexed mode

A sample can be switched from the dedicated mode to the multiplexed mode any time after T_n exceeds $T_n > \Theta_M$ in Eq. (7). Note that Θ_M depends on the total number of samples and increases as the MTDM scales to accommodate more samples. The MTDM continues calculating the dynamic measurement interval T_n in the multiplexed mode for reference, but the actual measurement interval θ_n will be

$$\theta_n = \min(T_n, \Theta_M) = \Theta_M, \tag{10}$$

after crossover in the multiplexed mode. The time t_n when a sample can transition from the dedicated mode to the multiplexed mode is defined as

$$t_n = t_M, \tag{11}$$

where t_M is called the multiplexed mode crossover time.

III. DEMONSTRATION EXPERIMENT: AMORPHOUS In-Ga-Zn-O THIN FILMS

A. Experiment setup

The conductivities of $\sigma_n^{m,k}$ of three a-IGZO films were measured as a means of demonstrating the MTDM unit. In this experiment, only one MTDM unit was used, so $m = 1$, and this superscript will be suppressed, $\sigma_n^{m=1,k} = \sigma_n^k$. The conductivity was measured with the van der Pauw method[15,16] with a lock-in amplifier by supplying an ac current through 2 contacts and measuring the resultant 4-point in-phase ac voltage. In Fig. 4, two SR830 lock-in amplifiers were used as measurement devices, one for the dedicated mode and the other for the multiplexed mode. All test signals were shielded with co-axial cables to reduce signal cross talk. The dedicated mode signal was also modulated at a frequency different from that of the multiplexed mode to further reduce signal interference. Note that the circuit description of each element in the MTDM with electronic part numbers can be found in the Appendix.

Three a-IGZO thin films were deposited via pulsed laser deposition (PLD) at different oxygen pressures. For more details on the PLD deposition of such films, please see Ref. 12. Oxygen vacancies are expected to be responsible for n-doping such films, hence lower oxygen pressures yield higher conductivities. Sample 1, sample 2, and sample 3 were exposed to P_{O_2} = 5 mTorr, 15 mTorr, and 5 mTorr oxygen pressure during deposition, respectively. The three samples had different illumination histories prior to this experiment. Therefore, sample 1 and sample 3 were expected to exhibit different responses despite the same oxygen pressure during

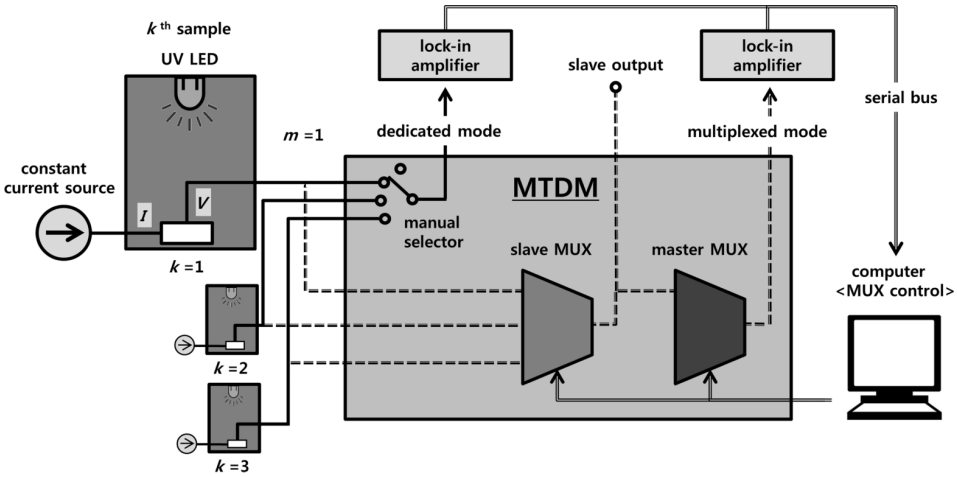

FIG. 4. Experimental setup for measuring the photoconductivity transients $\sigma^k(t)$ of three a-IGZO thin films after ultraviolet illumination for approximately 23 days. All of the samples were placed inside sealed metal chambers to prevent exposure to ambient light. Samples were measured in the dedicated mode immediately after the LED illumination was switched on or off, and in the multiplexed mode at longer times thereafter, according to the protocol described in Section II E.

fabrication. As indicated in Fig. 4, each sample was sealed inside a closed metal chamber to prevent exposure to ambient light during measurement. Each metal chamber contained an ultraviolet light emitting diode (UV LED) for illumination. One UV LED was turned on at a time. All UV LEDs were powered sequentially by a single power source with 3.6 V and 0.7 A to achieve full illumination power.

The resolution per time constant R in Eq. (4) was set to $R = 100$. The number of relaxation-fit data points q in Eq. (3) was set to $q = 50$. The number of samples N in Eq. (7) was $N = 3$. The shortest measurement interval possible was $\Theta_D = 20$ ms. The fastest measurement speed of the lock-in amplifier was larger than the communication protocol time between the computer and the lock-in amplifier, which became the limiting factor for the fastest measurement interval Θ_D. The stabilization time constant of the lock-in amplifier was $\tau_s = 3$ s. It is an order larger than the lock-in amplifier time constant, so that the switching transients can settle before new measurements. Although only three samples were measured, the total number of samples N was set to $N = 4$ for possible addition of sample. The multiplexed mode measurement interval Θ_M in Eq. (7) was then $\Theta_M = 12$ s. In the beginning of the measurement, all of the samples were connected to the multiplexed mode as designated in Fig. 5(d) where "none" are in the dedicated mode. Sample 1 was then switched to the dedicated mode first for the fast transient measurement during UV illumination. As per the previously described protocol, the lock-in amplifier started measuring the sample at the fastest possible rate with $\theta_n = \Theta_D$. After $q = 50$ points were measured, the MTDM was first able to estimate T_n based on the collected data. Once $T_n > \Theta_D$, the dedicated mode interval transitions to $\theta_n = T_n$. The data collection continued with θ_n increasing dynamically as the response time slowed down and T_n increased. Once $T_n > \Theta_D$, the sample was switched to the multiplexed mode and was measured at $\theta_n = \Theta_M$. This state was maintained for the remainder of the illuminated state for sample 1. Shortly before the end of the illumination, sample 1 was switched to the dedicated mode again in anticipation of the fast initial transient measurement expected during dark relaxation. The UV LED was then turned off, and the same cycle repeated. Sample 2 and sample 3 illumination transients and dark transients were subsequently measured with the same procedures. Fig. 5(d) shows which sample was in the dedicated mode during the measurement, namely at the beginning of the

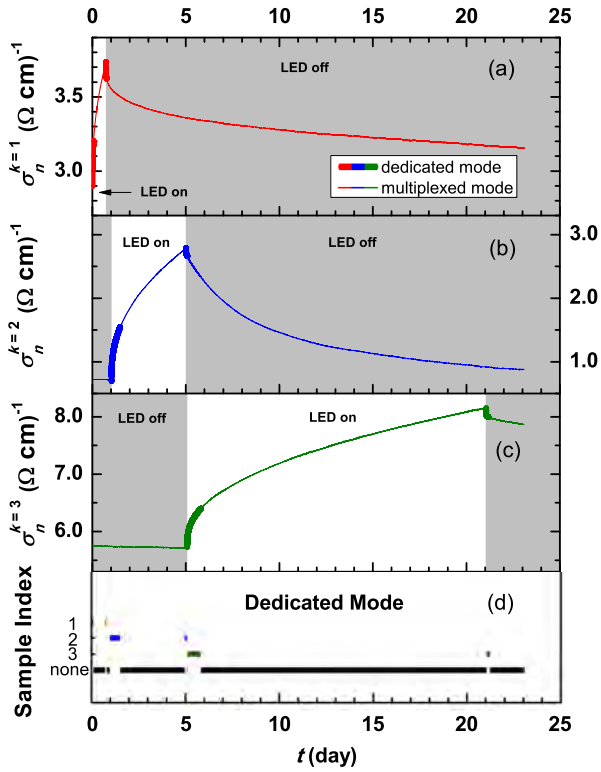

FIG. 5. Transient photoconductivity $\sigma^k(t)$ of three different a-IGZO thin films measured for approximately 23 days, (a) sample 1, (b) sample 2, and (c) sample 3. The samples were prepared at $P_{O_2} = 5$ mTorr, 15 mTorr, and 5 mTorr oxygen pressure, respectively. The samples also had different illumination histories, which differentiated the behaviors of the two 5 mTorr samples. The UV LED was turned off during the gray regions and was on during the white regions. (d) The timeline of samples measured in the dedicated mode. Multiplexed mode is active at all times. The colored lines represent which sample is being measured in the dedicated mode.

illumination, and immediately after the end of the illumination for each sample. Note that for the majority of the time, none of the samples were in dedicated mode, as designated by the black line, meaning that the dedicated mode measurement instrument was free to be removed from the measurement system for use elsewhere.

B. Performance analysis

Fig. 5 shows the conductivity measurement of three a-IGZO samples serving as a test for the MTDM operation. Transient photoconductivity σ_n^k of sample 1, sample 2, and sample 3 were measured for 23 days. If these three samples were measured in series, the total measurement duration would have been approximately 70 days. The same measurement could have been trivially expanded to measure 16 samples in parallel with equal ease without increasing the overall measurement time. This reduces a measurement time that would have lasted over a year to one that lasts just over 3 weeks. Note, also, that there are long stretches where the dedicated mode lock-in amplifier can be freed for other use, so that many days of experimentation require only a single lock-in as indicated by the black solid line in Fig. 5(d). The minimum usage of the lock-in amplifier for the dedicated mode is several hours by strictly following the crossover protocol from dedicated to multiplexed mode outlined here. The

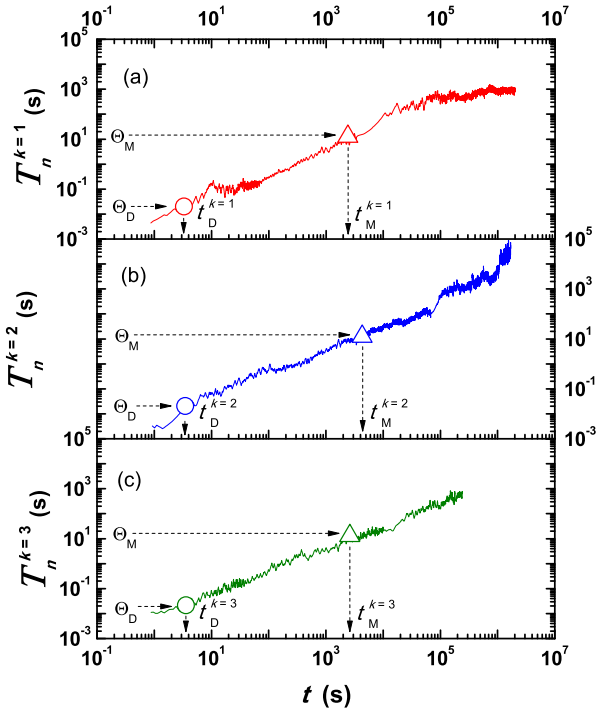

FIG. 6. Dynamic measurement interval T_n of three a-IGZO thin films after ultraviolet illumination, (a) sample 1, (b) sample 2, and (c) sample 3. According to the method described in Section II A, the first T_n value can only be reported after $q = 50$ data points have been measured, hence the time delay between the measurements of σ_n and T_n. Circles identify the minimum interval crossover time t_D when the actual measurement interval θ_n is switched from the shortest measurement possible $\theta_n = \Theta_D$ to the dynamic measurement time interval $\theta_n = T_n$. Triangles identify the multiplexed mode crossover time t_M where the sample response is slow enough that it can transition to the multiplexed mode, $T_n = \Theta_M$.

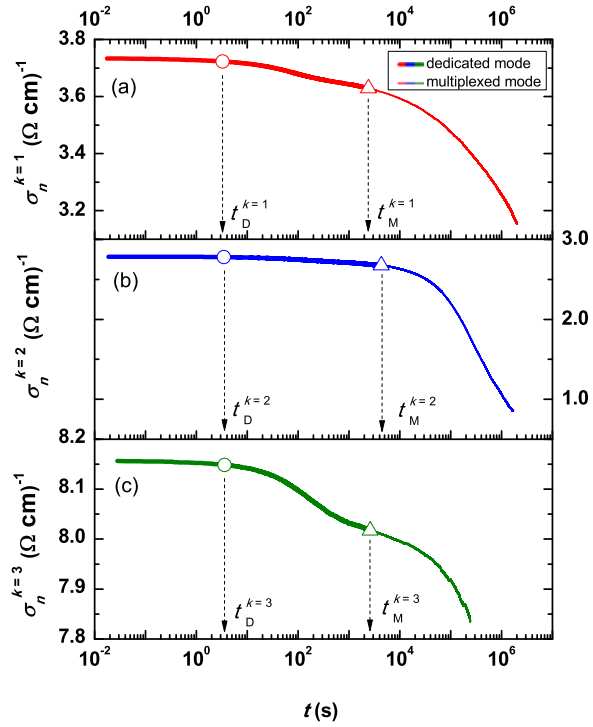

FIG. 7. A subset of the data of Fig. 5 showing the relaxation of photoconductivity $\sigma^k(t)$ of three a-IGZO thin films after ultraviolet illumination plotted in log time, (a) sample 1, (b) sample 2, and (c) sample 3. Circles and triangles designate the same important dedicated mode and multiplexed mode crossover time scales as identified in Fig. 6.

measurement duration of this particular measurement could be reduced even further if the three UV LEDs had independent power supplies and could be illuminated simultaneously.

In addition to the significant measurement time and resource savings, the MTDM was able to measure the rapid sample transients with a high resolution. Figure 6 shows the time dependence of the dynamic measurement interval T_n from the measurement data deduced using the least square fit method of Section II A. From the crossover scales Θ_D and Θ_M, one can determine the dedicated mode dynamic crossover time for each curve t_D^k, and the multiplexer mode crossover time t_M^k. In logarithmic scale, Fig. 7 shows the relaxation of the three a-IGZO samples after ultraviolet illumination. The dynamic measurement interval T_n ranged from $T_n = 10^{-3}$ s to 10^5 s. Using Eq. (4) and $R = 100$, the decay time scale for all three samples ranged from $\tau = 10^{-1}$ s to 10^7 s, covering 8 orders of magnitudes of time constants. The crossover times determined from Fig. 6 are also indicated as t_D^k and t_M^k.

IV. CONCLUSION

The modular time division multiplexer (MTDM) significantly reduces the measurement duration and equipment usage for continuous long term measurements of multiple samples that exhibit both fast and slow transients. The MTDM can measure the fast transients with high resolution and the slow transients with low resolution, and dynamically adjust the resolution with time to match to the natural response of the signal under study. Two crossover time scales are identified. The first time scale Θ_D is the time scale associated with the

fastest response time of the equipment. No meaningful data can be taken at time scales faster than Θ_D, so Θ_D sets the start of meaningful data in the dedicated mode. The second crossover time scale Θ_M is defined when the sample is switched to the multiplexed mode. The multiplexed mode measures multiple samples in parallel by cycling connections between individual samples and the measurement instrument. The MTDM can be used in a hierarchical modular setup with several slave units and one master MTDM unit. Such setup allows two advantages: Samples can be easily added without interrupting measurements and an increased number of samples can be measured per unit equipment usage time.

As an example, the MTDM was demonstrated with a study of a-IGZO transients. This measurement method can save up to a factor of N in measurement time, where N is the number of samples, without increasing measurement instrument usage by implementing higher level hierarchy schemes. Because measurements often last weeks or months, this factor of improvement makes many experiments on technologically relevant materials possible that would not previously have been feasible.

ACKNOWLEDGMENTS

This work was supported by Undergraduate Research Grant of Northwestern University, the NSF MRSEC Program No. DMR-1121262 at the Materials Research Center of Northwestern University, and the Air Force Office of Scientific Research Grant No. FA9550-15-1-0247.

APPENDIX: DETAILS FOR THE LOW-COST IMPLEMENTATION OF MTDM

Figure 8 shows the circuit schematic of the low-cost implementation of MTDM for measuring the transient photoconductivity of a-IGZO samples due to illumination. All circuit elements of MTDM in Fig. 8 were implemented on a PCB. Ultraviolet LED, multiplexers, and operational amplifier part numbers are listed in the schematic. The wavelength of the UV LED was centered at 385 nm. A single rotary switch with 6 parallel channels was used as the manual selector, allowing all six rotary switches above to be turned simultaneously. Figure 9 shows the picture of the low-cost implementation

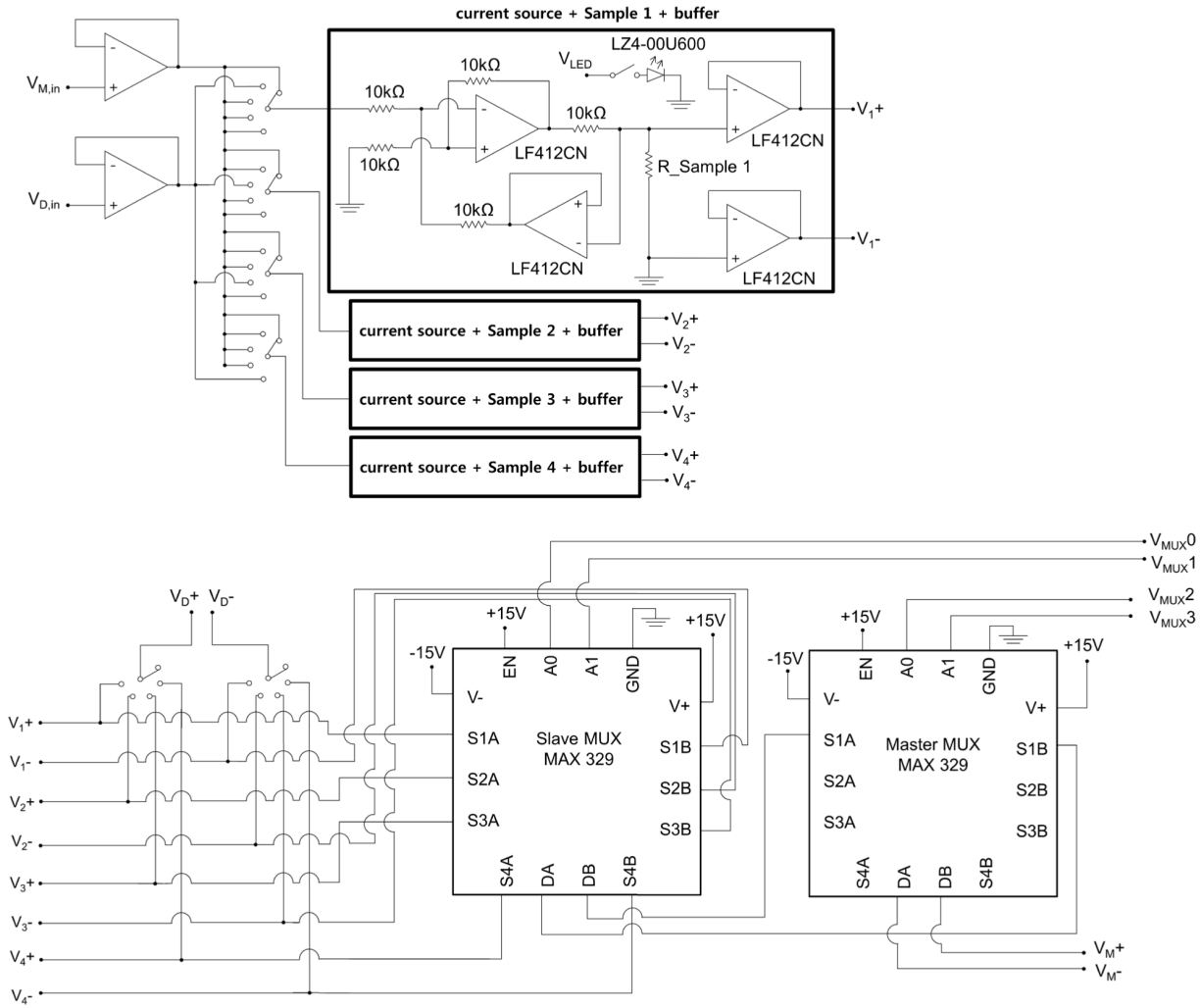

FIG. 8. The circuit schematic of a MTDM unit for measuring the transient photoconductivity of a-IGZO samples. $V_{D,in}$ and $V_{M,in}$ are voltage inputs to the current sources for the dedicated mode and the multiplexed mode, respectively. The difference between V_D+ and V_D− is the four-point voltage across the sample that is being measured in the dedicated mode. The difference between V_M+ and V_M− is the voltage across the sample in the multiplexed mode that is indexed by the two multiplexers. A computer program written in Python indexes the multiplexers using pins V_{MUX}0 through V_{MUX}3.

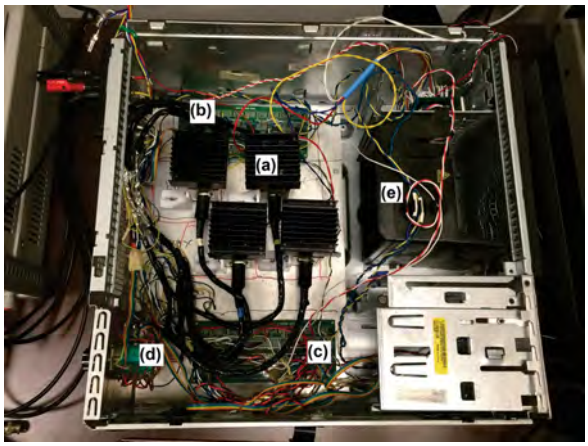

FIG. 9. The picture of the low-cost implementation of MTDM for measuring the transient photoconductivity of a-IGZO samples due to illumination, presented in Fig. 4. (a) Sample chambers which contain a-IGZO samples and the UV LEDs, (b) the constant current source circuit, (c) the slave and the master multiplexer circuit, (d) the manual selector, and (e) a fan used to dissipate heat generated from the UV LEDs.

of MTDM. The MTDM could fit inside a metal box that has dimensions of 80 cm × 80 cm × 40 cm. A fan and sample chambers occupied most of the space inside the metal box.

[1]L. Ciani, M. Catelani, E. A. Carnevale, L. Donati, and M. Bruzzi, IEEE Trans. Instrum. Meas. **64**, 1179 (2015).
[2]N. A. Ludin, A. Al-Alwani Mahmoud, A. Bakar Mohamad, A. A. H. Kadhum, K. Sopian, and N. S. Abdul Karim, Renewable Sustainable Energy Rev. **31**, 386 (2014).
[3]M. K. Nazeeruddin, E. Baranoff, and M. Grätzel, Sol. Energy **85**, 1172 (2011).
[4]S. Grolleau, A. Delaille, H. Gualous, P. Gyan, R. Revel, J. Bernard, E. Redondo-Iglesias, and J. Peter, J. Power Sources **255**, 450 (2014).
[5]A. Eddahech, O. Briat, and J.-M. Vinassa, Energy **84**, 542 (2015).
[6]B. Stiaszny, J. C. Ziegler, E. E. Krauß, M. Zhang, J. P. Schmidt, and E. Ivers-Tiffée, J. Power Sources **258**, 61 (2014).
[7]P. Röder, B. Stiaszny, J. C. Ziegler, N. Baba, P. Lagaly, and H. D. Wiemhöfer, J. Power Sources **268**, 315 (2014).
[8]R. H. Bube and D. Redfield, J. Appl. Phys. **66**, 820 (1989).
[9]R. Bube, L. Echeverria, and D. Redfield, Appl. Phys. Lett. **57**, 79 (1990).
[10]K. Nomura, H. Ohta, A. Takagi, T. Kamiya, M. Hirano, and H. Hosono, Nature **432**, 488 (2004).
[11]T.-Y. Hsieh, T.-C. Chang, T.-C. Chen, and M.-Y. Tsai, ECS J. Solid State Sci. Technol. **3**, Q3058 (2014).
[12]J. Luo, A. U. Adler, T. O. Mason, D. Bruce Buchholz, R. P. H. Chang, and M. Grayson, J. Appl. Phys. **113**, 153709 (2013).
[13]D. P. Bertsekas and J. N. Tsitsiklis, *Introduction to Probability*, 2nd ed. (Athena Scientific, 2008), pp. 462–466 and 478–479.
[14]B. A. Moores, A. Eichler, Y. Tao, H. Takahashi, P. Navaretti, and C. L. Degen, Appl. Phys. Lett. **106**, 213101 (2015).
[15]L. J. van der Pauw, Philips Res. Rep. **13**, 1 (1958).
[16]G. T. Kim, J. G. Park, Y. W. Park, C. Muller-Schwanneke, M. Wagenhals, and S. Roth, Rev. Sci. Instrum. **70**, 2177 (1999).

Polycrystalline $ZrTe_5$ Parametrized as a Narrow-Band-Gap Semiconductor for Thermoelectric Performance

Samuel A. Miller,[1] Ian Witting,[1] Umut Aydemir,[1,2] Lintao Peng,[3] Alexander J. E. Rettie,[4] Prashun Gorai,[5,6] Duck Young Chung,[4] Mercouri G. Kanatzidis,[4,7] Matthew Grayson,[3,8] Vladan Stevanović,[5,6] Eric S. Toberer,[5,9] and G. Jeffrey Snyder[1,*]

[1]*Department of Materials Science and Engineering, Northwestern University, Evanston, Illinois 60208, USA*
[2]*Department of Chemistry, Koç University, Sariyer, Istanbul 34450, Turkey*
[3]*Applied Physics Graduate Program, Northwestern University, Evanston, Illinois 60208, USA*
[4]*Materials Science Division, Argonne National Laboratory, Argonne, Illinois 60439, USA*
[5]*National Renewable Energy Laboratory, Golden, Colorado 80401, USA*
[6]*Department of Metallurgical and Materials Engineering, Colorado School of Mines, Golden, Colorado 80401 USA*
[7]*Department of Chemistry, Northwestern University, Evanston, Illinois 60208, USA*
[8]*Department of Electrical Engineering and Computer Science, Northwestern University, Evanston, Illinois 60208, USA*
[9]*Department of Physics, Colorado School of Mines, Golden, Colorado 80401 USA*

(Received 25 August 2017; revised manuscript received 22 November 2017; published 24 January 2018)

The transition-metal pentatellurides $HfTe_5$ and $ZrTe_5$ have been studied for their exotic transport properties with much debate over the transport mechanism, band gap, and cause of the resistivity behavior, including a large low-temperature resistivity peak. Single crystals grown by the chemical-vapor-transport method have shown an n-p transition of the Seebeck coefficient at the same temperature as a peak in the resistivity. We show that behavior similar to that of single crystals can be observed in iodine-doped polycrystalline samples but that undoped polycrystalline samples exhibit drastically different properties: they are p type over the entire temperature range. Additionally, the thermal conductivity for polycrystalline samples is much lower, 1.5 Wm^{-1} K^{-1}, than previously reported for single crystals. It is found that the polycrystalline $ZrTe_5$ system can be modeled as a simple semiconductor with conduction and valence bands both contributing to transport, separated by a band gap of 20 meV. This model demonstrates to first order that a simple two-band model can explain the transition from n- to p-type behavior and the cause of the anomalous resistivity peak. Combined with the experimental data, the two-band model shows that carrier concentration variation is responsible for differences in behavior between samples. Using the two-band model, the thermoelectric performance at different doping levels is predicted, finding $zT = 0.2$ and 0.1 for p and n type, respectively, at 300 K, and $zT = 0.23$ and 0.32 for p and n type at 600 K. Given the reasonably high zT that is comparable in magnitude for both n and p type, a thermoelectric device with a single compound used for both legs is feasible.

DOI: 10.1103/PhysRevApplied.9.014025

I. INTRODUCTION

Thermoelectric (TE) materials are those that convert a temperature gradient to a voltage or an electrical current flow into a heat flow, with applications in power generation and Peltier cooling. This thermoelectric conversion of heat energy into electrical energy, the Seebeck effect, has been well studied, with compounds optimized for use in various temperature ranges and applications. Mid- and high-temperature thermoelectrics have been well investigated, including PbTe, SiGe, and Zintl compounds [1–5]. However, there is a dearth of materials for applications at lower temperatures. To date, TE materials for cooling applications fall into one of three families: $Bi_{1-x}Sb_x$ [6,7], $CsBi_4Te_6$ [8,9], or $(Bi,Sb)_2(Te,Se)_3$ [10,11]. Furthermore, construction of thermoelectric generators requires thermal and chemical stability and matching between the n and p legs of the device [12]. Recently, there has been interest in the use of layered transition-metal pentatellurides for low-temperature thermoelectric applications. $ZrTe_5$ and $HfTe_5$ have demonstrated high power factors, though the thermal conductivity is relatively high [13,14]. Measurement of needlelike single

*Corresponding author.
jeff.snyder@northwestern.edu

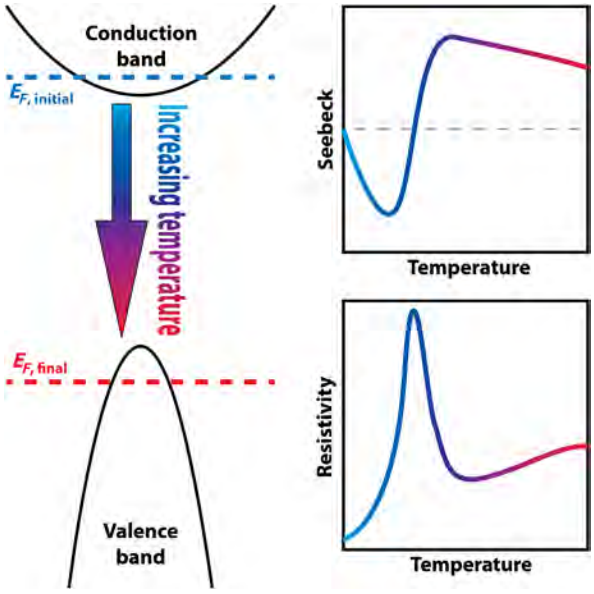

FIG. 1. Schematic of the two-band model for the iodine-doped polycrystalline sample (or vapor-grown single crystals) showing movement of the Fermi level with increasing temperature and the resulting properties.

crystals showed the thermal conductivity to be in the range of approximately 4–8 Wm^{-1} K^{-1} at room temperature [15]. In contrast, recent calculations indicated that the lattice thermal conductivity should be much lower [16–18], and, thus, the zT higher than initially thought, warranting further study [19].

However, the optimization of thermoelectric performance through compositional tuning of the pentatelluride materials has been difficult due to a poor understanding of the underlying transport. Chemical-vapor-grown single crystals of $ZrTe_5$ exhibit a peak in resistivity (ρ) as a function of the temperature and a change in sign of the Seebeck coefficient (α) at approximately 130 K. There have been many explanations for this behavior over the years. Researchers first believed this was due to charge-density waves [20], but diffraction, magnetic field, and compositional data indicated this was not likely the cause of the peaked resistivity [21,22]. Other explanations have since been advanced, but there has not been consensus on the cause of the transport phenomena [23,24]. The temperature-induced Lifshitz transition has been studied as well as the quantum Hall effect and chiral magnetic effect [25–30], but there remains a debate over whether pentatellurides are topological insulators with a small band gap or whether they are Dirac semimetals [31–36].

To more specifically investigate the promise of $ZrTe_5$ as a thermoelectric material, we produce bulk polycrystalline $ZrTe_5$ samples. Our undoped samples are p type over the entire temperature range, though substitution of iodine for tellurium causes a transition to n type at low temperatures, in agreement with previous reports. Using the experimental Seebeck coefficient, thermal conductivity (κ), and Hall data, we find that in the polycrystalline form, these pentatellurides can be modeled as a narrow-band-gap semiconductor with effective contributions from a single n-type conduction band and a single p-type valence band. We then use our model to explain previous property observations in the literature and are able to explain the resistivity peak in terms of an n-type to p-type thermally induced crossover shown schematically in Fig 1. We also investigate predicted thermoelectric properties from this model and show how to optimize the zT for these polycrystalline materials, as well as note their potential use for both n- and p-type legs in the same device.

II. METHODS

Bulk polycrystalline $ZrTe_{5-x}I_x$ samples are produced by solid-state reaction of Zr (Alfa Aesar, 99.95%), Te (Alfa Aesar, 99.999%), and TeI_4 (Strem Chemical, 99.9%) followed by hot pressing. Zr is mixed in a stoichiometric ratio with Te and TeI_4, placed in a quartz ampule, evacuated to 10^{-5} mbar, and torch sealed. Using a vertical single-zone furnace, the heating profile is 90 K/h from room temperature to 923 K, dwell time of 12 h, furnace quench (300 K/h) to 748 K, dwell for 72 h, and finally cooling to room temperature at 90 K/h. The resulting material is ground in an agate mortar and pestle into a fine powder. The powder is hot pressed in a half-inch graphite die using a maximum temperature of 723 K for 2 h under flowing argon followed by ambient cooling. A series of grit papers ending in 1200 grit is used to polish residual graphite foils and produce samples of uniform thickness.

X-ray diffraction is used to monitor the sample purity by a Rigaku D/Max diffractometer. A Netzsch LFA 457 is used to measure the thermal diffusivity at high temperatures, and the Dulong-Petit approximation is applied for the heat capacity. The Hall coefficient and ρ are measured using a four-point van der Pauw technique with a 2-T magnet under high vacuum, while a light-pipe method utilizing chromel-niobium thermocouples is used to measure the Seebeck coefficient [37,38]. For the low-temperature measurements, a number of instruments are used to measure the various properties. A Physical Property Measurement System (PPMS, Quantum Design) is used in the van der Pauw configuration as well as with the Thermal Transport Option (TTO). For all PPMS measurements, the contacts are made out of silver paste, air dried, and are Ohmic in the temperature range considered. Additional low-temperature magnetotransport and Hall measurements are done on square planar devices with four-corner contacts applying the van der Pauw method. The experiment is conducted in a Cryogenic Ltd. cryogen-free 5-T magnet system with a helium flow cryostat using ac lock-in techniques (SR830).

To model and analyze the thermoelectric transport data, the effective mass model is used [39]. This model is frequently employed to guide the understanding and

optimization of thermoelectrics. However, there are cases where the effective mass model breaks down, namely, due to nonparabolic bands or multiband effects [40–42]. We consider two bands contributing to transport and restrict the use of the model to higher temperatures where any possible topological and phase-coherent effects are suppressed. One valence and one conduction band are used, both with a rigid band shape that does not change with the temperature or doping level. In this model, the effective mass and initial doping level for each band are fixed along with the band gap. To calculate the Fermi level at each temperature, the charge neutrality condition is used for the chemical potential relationship between two bands with known gap. The charge neutrality is given by

$$N_d^+ + p = n + N_a^-, \tag{1}$$

where N_d^+ and N_a^- are the number of ionized donors and acceptors, respectively, and p and n are the concentrations of holes and electrons. For a given band gap E_g, the relationship between the reduced chemical potentials of the two bands is given by the expression

$$\eta_1 = -\eta_2 - \frac{E_g}{k_B T}. \tag{2}$$

Once the masses, dopant level, and band gap are set and the Fermi level at each temperature is calculated, the properties of each band according to the effective mass model can be determined. These properties are given below for a two-band system, though they can be generalized to multiband with the appropriate summations:

$$\alpha_{\text{tot}} = \frac{\alpha_1\sigma_1 + \alpha_2\sigma_2}{\sigma_1 + \sigma_2}, \tag{3}$$

$$\sigma_{\text{tot}} = \sigma_1 + \sigma_2, \tag{4}$$

$$R_{H,\text{tot}} = \frac{R_{H,1}\sigma_1^2 + R_{H,2}\sigma_2^2}{\sigma_{\text{tot}}^2}, \tag{5}$$

where α, σ, and R_H are the Seebeck coefficient, electrical conductivity, and Hall coefficient, respectively. The subscripts 1 and 2 denote the contribution from each of the two bands (in this case, one conduction and one valence, though this analysis can be applied to two bands of the same type). The total thermal conductivity (κ_{tot}) is then given by

$$\kappa_{\text{tot}} = \kappa_L + T(L_1\sigma_1 + L_2\sigma_2) + T\left((\sigma_1\alpha_1^2 + \sigma_2\alpha_2^2) - \frac{(\sigma_1\alpha_1 + \sigma_2\alpha_2)^2}{\sigma_1 + \sigma_2}\right). \tag{6}$$

Here, the first term, the lattice thermal conductivity (κ_L), is set in the model to have some temperature dependence. At high temperature, Umklapp scattering dominates, which has a T^{-1} dependence. The second term is the electronic thermal conductivity, which depends on the temperature, electrical conductivity, and Lorentz number (L). The third term is bipolar thermal conductivity.

III. RESULTS AND DISCUSSION

A. Synthesis and characterization

Most previous reports of $ZrTe_5$ properties have been for single crystals grown by a chemical-vapor-transport method. For these crystals, the Seebeck coefficient is linear at low temperature, changes from n to p type near 130 K, and has an absolute value of approximately 100–200 μV K^{-1}, while the temperature-dependent resistivity has a peak around 130 K, which is a few times higher than the room-temperature value [13,14,43–49]. Recently, a tellurium self-flux-growth technique was used to synthesize single crystals, an alternative to the traditional vapor-transport growth [25]. These flux-grown crystals exhibit similar behavior as chemical-vapor-transport single crystals in general, though there are some key differences when compared with vapor-grown crystals. For example, ρ does not trend toward zero at 0 K, the n-type α is significantly larger in magnitude, and most important, the temperature is much lower for the n-p transition and resistivity peak, around 60 K. These differences indicate that synthesis techniques are very important in determining the properties of $ZrTe_5$. In addition to the influence on differences in the TE properties, both the vapor-growth and self-flux techniques produce needlelike single crystals which are small and can present challenges for property measurement and sample loading. Finally, there are seldom reports of the thermoelectric properties above 300 K [13], which would provide a more complete understanding of the transport. To resolve these issues, we synthesize the $ZrTe_5$ samples by solid-state reaction and hot pressing, producing large, bulk, polycrystalline samples for study across the entire temperature range, approximately 0 to 700 K.

$ZrTe_{5-x}I_x$ samples are prepared by solid-state reaction and hot pressing with powder XRD used to monitor the sample purity at room temperature (see Fig. S1 in the Supplemental Material [50]). Rietveld refinement is performed by the WinCSD program package [51] on the hot pressed undoped sample [52], and the result is shown in Fig. S2. All compositions labeled in the text and figures are the nominal composition. Additional details on x-ray diffraction, Rietveld refinement, and raw transport data can be found in the Supplemental Material [50]. The samples are nearly phase pure after solid-state reaction as well as following hot pressing. The geometric density of the hot-pressed samples is greater than 98% of the theoretical density for $ZrTe_5$. The Seebeck coefficient and resistivity for the polycrystalline $ZrTe_{5-x}I_x$ samples are shown in Fig. 2. While the $ZrTe_{4.85}I_{0.15}$ sample exhibits properties largely similar to previous reports on chemical-vapor-grown single-crystal samples, the behavior of

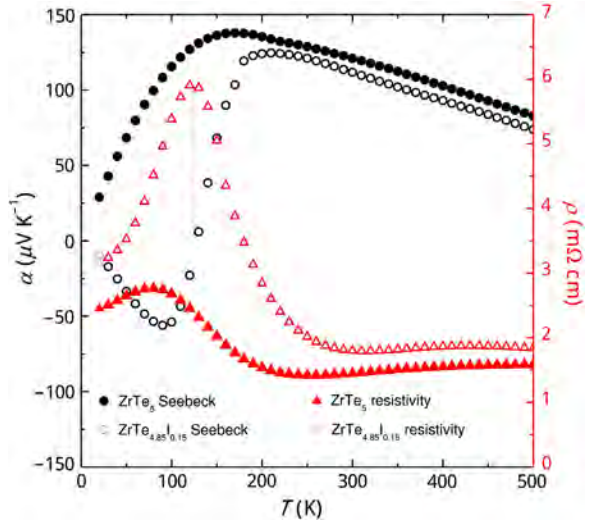

FIG. 2. Seebeck coefficient and resistivity for polycrystalline $ZrTe_5$ and $ZrTe_{4.85}I_{0.15}$. Dashed line at 130 K indicating resistivity peak and Seebeck coefficient crossing zero for $ZrTe_{4.85}I_{0.15}$. Undoped $ZrTe_5$, by contrast, has a lower temperature resistivity peak and stays p type over the full temperature range.

undoped polycrystalline $ZrTe_5$ is quite different (Fig. 2). The Seebeck coefficient for the latter is always positive, and the resistivity peak is shifted to a lower temperature, closer to 60 K, in addition to being smaller in magnitude relative to $\rho_{300\ \mathrm{K}}$.

The resistivity (ρ_{xx}) and Hall resistance (R_{xy}) as a function of magnetic field are shown in Fig. 3 for these polycrystalline samples. At low temperatures, $\rho_{xx}(B)$ shows an antilocalization minimum at $B = 0$ typically associated with strong spin-orbit coupling typical to the valence band and also the conduction band for narrow-gap materials [53]. This behavior could also be attributed to topological surface states, possibly at grain-boundary interfaces. Numerous unconventional effects have previously been observed in single crystals at low temperatures, including the chiral magnetic effect [28,29], Lifshitz transition [25,54], van Hove singularity [55,56], Zeeman splitting [57,58], and topological effects [31,33,34,53,54,59]. This measurement demonstrates that some of the unconventional effects previously observed at low temperatures in single crystals persist in polycrystalline samples as well. However, at higher temperatures, these effects are less important in their contributions to the transport behavior. As the temperature increases, $\rho_{xx}(B)$ in Fig. 3(a) is less dependent on magnetic field over the relevant magnetic field range, deviating at most $\pm 25\%$ around the mean value, with a sharp curvature only at the lowest temperature. Thus, we define an arbitrary cutoff of 150 K, above which we argue that a Drude-like model with no consideration of phase-coherent effects can approximate the observed behavior but below which a more careful model including weak antilocalization is needed. The Hall resistance for $ZrTe_{4.85}I_{0.15}$ is consistent with previous measurements [25]

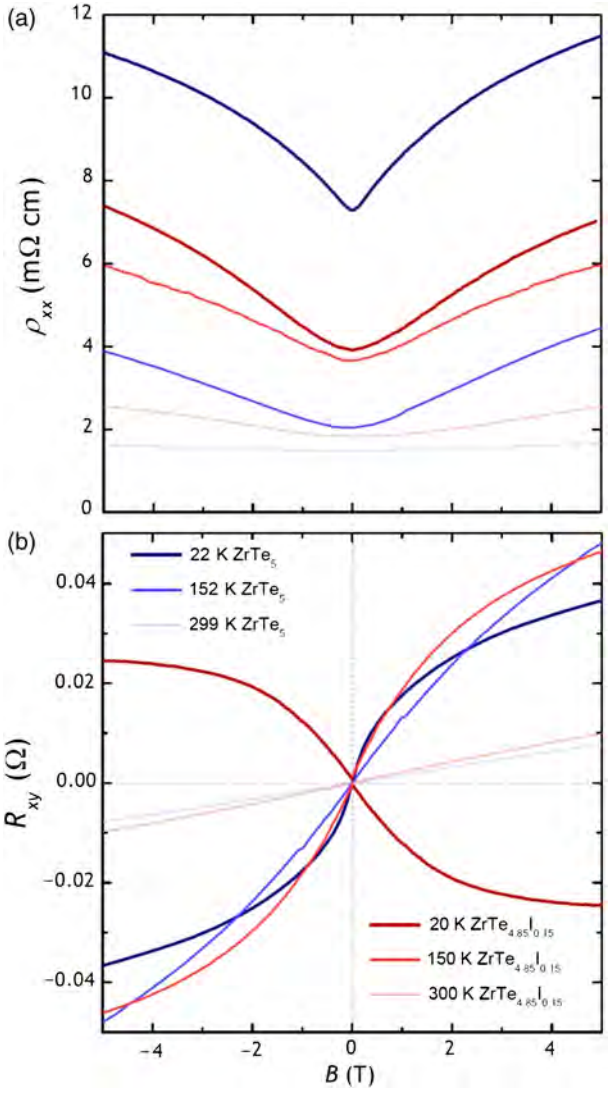

FIG. 3. Resistivity (a) and Hall resistance (b) for both $ZrTe_5$ and $ZrTe_{4.85}I_{0.15}$ at select temperatures (well below, near, and well above the transition).

and with Seebeck coefficient measurements showing n-type conduction at low temperatures and switching to p type at higher temperatures, while undoped $ZrTe_5$ remains p type at all temperatures, again consistent with Seebeck coefficient measurements. Both of the polycrystalline samples show nonlinearity of R_{xy} with B at lower temperatures, possibly indicating more than one carrier contributes to conduction. As the temperature increases, R_{xy} becomes linear with B, indicating a single charge carrier dominates.

B. Two-band modeling

Although there are prominent features in the low-temperature magnetotransport associated with spin-orbit coupling and phase-coherent scattering, as we shall demonstrate, the higher-temperature properties above 150 K can be reproduced with a simple two-band model for all of

the transport coefficients in this high temperature range. In addition, the qualitative trends at low temperature can also be reproduced with the same parametrization. We, therefore, propose a simplified two-band model that clarifies the significantly different properties observed in the $ZrTe_5$ samples produced by different methods (polycrystalline, flux, or vapor grown) and offers insight into the phenomena of the resistivity peak and Seebeck coefficient switching from n to p type. Using this simple two-band model with one valence and one conduction band, we can describe the thermoelectric properties observed for various samples by changing only the doping level.

The effective mass model used here is similar to the single parabolic band model commonly used in thermoelectrics, but it considers contributions from two bands (one conduction and one valence). To construct the model, we fix a number of parameters based on previous experimental and computational studies and then determine the mobility needed to explain the experimentally measured transport properties. The Boltzmann transport equations have previously been derived assuming the Drude model for mobility and an energy-dependent scattering time $\tau = \tau_0 E^{\lambda-1/2}$ ($\lambda = 0$ for the acoustic phonon) [60]. For the fits to the polycrystalline $ZrTe_{5-x}I_x$ samples, we fix the isotropic electron and hole Seebeck mass as $m_e = 0.5\ m_0$ and $m_h = 0.15\ m_0$, respectively, and the band gap as $E_g = 0.02$ eV. The number of donors for the iodine-doped sample is fixed at $N_d = 1.1 \times 10^{18}$ cm^{-3}, while for the undoped $ZrTe_5$ sample, the number of acceptors is $N_a = 4.5 \times 10^{17}$ cm^{-3}. To appropriately fit the data, we find that the masses, their ratio, and the band gap are required to be within a relatively narrow range. For example, it is only possible to fit the model to experimental data when the band gap is set between approximately 0.015 and 0.03 eV. Previous experimental studies using a variety of techniques have found that the band gap of $ZrTe_5$ can be anywhere from 100 meV to a gapless semimetal [27,28,31–35,54,61]. However, recent ARPES studies observed a 40-meV band gap at 255 K which decreases with decreasing temperature [54], while another measured a gap of 18–29 meV [62]. We find that the model works best with a gap of 20 meV. As this is an effective mass model, we cannot definitively determine each of the parameters without more experimental data; we can suggest only general ranges and ratios of the parameters. Additionally, an isotropic model is used here, whereas the transport properties in $ZrTe_5$ are anisotropic [58,63,64]. The transport properties are expected to be anisotropic due to the structure of $ZrTe_5$ and needlelike growth of single crystals. However, the solid-state reaction, grinding, and hot-pressing procedure used here produces a sample that is not textured, as seen in the Rietveld refinement. Instead, the sample is a collection of randomly oriented grains such that the properties for each direction are averaged out, allowing the use of a simpler, isotropic model here.

The experimental properties for both polycrystalline samples, as well as the model using two different doping levels, are shown in Fig. 4. The model fits the data reasonably well in the range of 200–600 K. The resistivity as a function of the temperature is well described by this effective mass model across the entire temperature range [Fig. 4(a)]. The Seebeck coefficient data fits well at high temperature [Fig. 4(b)]. The model deviates from the experimental data at low temperatures, though this is to be expected. As discussed previously, the unconventional transport effects start to dominate in these polycrystalline samples at low temperature. The modeled Hall coefficient qualitatively reproduces the trends observed in the experimental Hall coefficient [Fig. 4(c)], which is determined using a linear fit to the low-field R_{xy} vs B data.

The resistivity and Seebeck coefficient behavior for the $ZrTe_{4.85}I_{0.15}$ sample is very similar to previous reports for chemical-vapor-grown single crystals, showing n-type behavior at low temperature. The Seebeck coefficient is n type at low temperature and increasing in magnitude as the Fermi level is initially in the conduction band and moving toward the gap with increasing temperature. The temperature where the Seebeck coefficient crosses zero and the resistivity is at a maximum (approximately 130 K in this case) is where the Fermi level nears the middle of the gap. With increasing temperature, the Fermi level continues toward the valence band as the material becomes more p type. Finally, after the Seebeck coefficient reaches its maximum p-type value, it then decreases linearly with the temperature, when the Fermi level becomes effectively pinned within the valence band (see Fig. 1). As we demonstrate later, the initial position of the Fermi level in the conduction band is what controls the temperature at which $\alpha = 0$ and the resistivity is peaked. On the other hand, for the undoped polycrystalline $ZrTe_5$, the Seebeck coefficient is always positive due to the Fermi level residing in the valence band. At low temperatures, the Fermi level moves toward the gap leading to the linear increase in α, and eventually, it is pinned within the valence band.

The model for κ [Fig. 4(d)] considers Umklapp scattering as well as the electronic and bipolar contributions to total thermal conductivity. Umklapp scattering dominates at higher temperatures and has a T^{-1} dependence which fits the data well at higher temperatures in the area of interest for zT predictions. Below 200 K, the model fit to the experimental data is not as good, partly due to the use of a PPMS for low-temperature measurements which uses a direct measurement technique that is uncorrected for radiation. The fit below 200 K is not expected to be exact, as the measurement technique differs, and other scattering mechanisms (i.e., point defect or boundary scattering) may play a role at lower temperatures. Because of the layered crystal structure, κ is fairly low. Though $ZrTe_5$ is predicted to have a lattice thermal conductivity of 1.8 Wm^{-1} K^{-1} at 300 K [19], the initial reports in single-crystal $ZrTe_5$ found

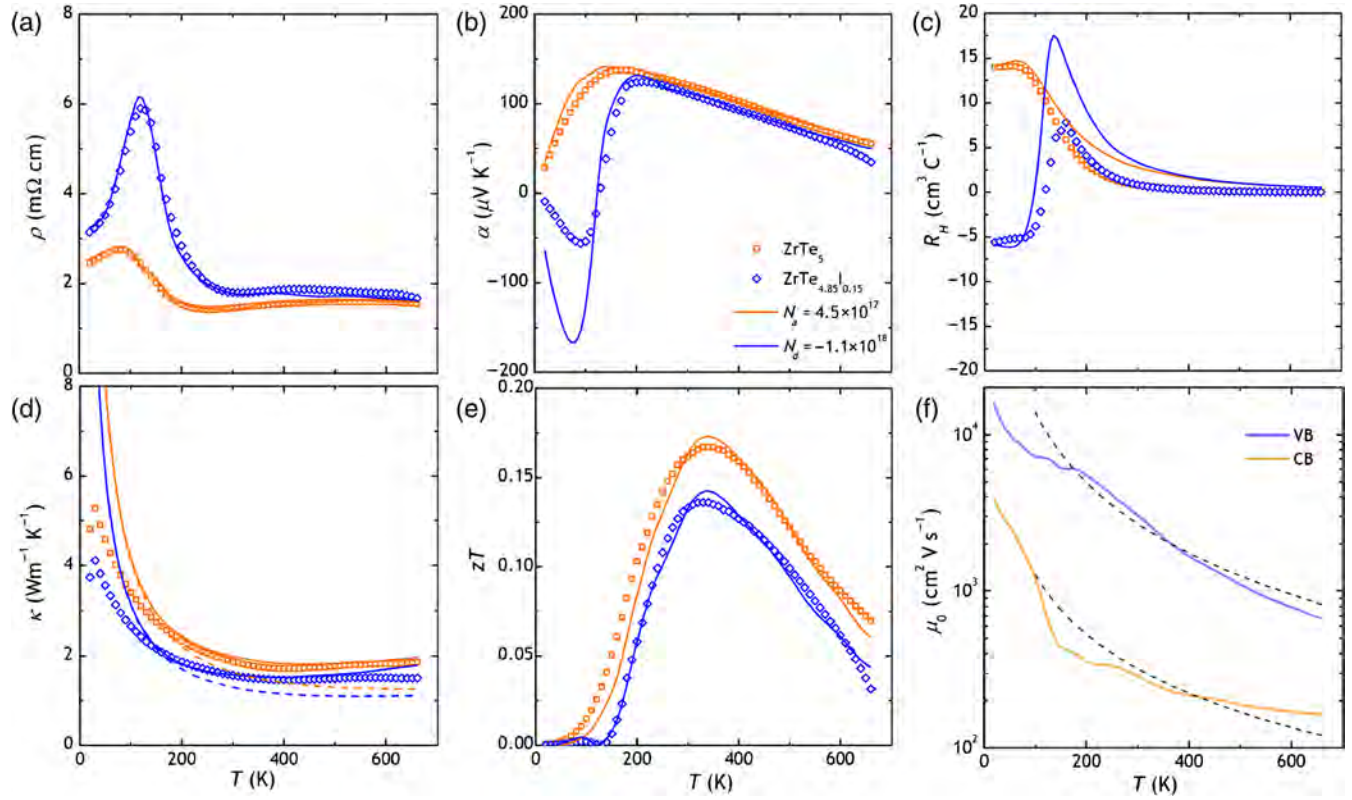

FIG. 4. Smoothed experimental data (symbols) for (a) resistivity, (b) Seebeck coefficient, (c) Hall coefficient, (d) total thermal conductivity, and (e) zT. Also shown are the modeled properties (lines) with two different carrier concentrations using the parameters listed in the text. In (e), the total (solid) and lattice plus bipolar (dashed) thermal conductivity using the model are shown. The modeled mobility is shown in (f) with dashed lines representing $T^{-3/2}$.

$\kappa \sim 8\ \mathrm{Wm^{-1}\,K^{-1}}$. However, due to the small size and needlelike shape of the single crystals measured previously, there may be a significant error in the initial report of thermal conductivity. These measurements demonstrate a much lower total thermal conductivity, experimentally confirming the prediction [Fig. 4(d)] in line with previous measurements [65]. This difference in the thermal conductivity is expected due to the polycrystalline nature, but it is also partly due to the measurement technique allowed by the larger size and shape of these samples. Our polycrystalline $ZrTe_5$ samples exhibit a total thermal conductivity 4 times lower than that measured for single crystals along the a axis, so while the power factor is reduced, the overall zT [Fig. 4(e)] is higher.

In most thermoelectric materials, it is sufficient to assume solely acoustic phonon scattering for modeling purposes, as they tend to be investigated at temperatures above 300 K. However, for these pentatelluride systems, the thermoelectric behaviors of interest occur below 200 K, where other scattering mechanisms can play a significant role. For example, in Si and Ge, ionized impurity scattering dominates the temperature dependence of mobility at low temperatures, while acoustic phonon scattering is more important at higher temperatures [60]. The Fermi integrals used in this model are for $\lambda = 0$ acoustic phonon scattering, since we are primarily concerned with high-temperature properties while the model is not expected to fit precisely at low temperatures due to the reasons discussed previously. The mobility used to fit the measured properties is shown in Fig. 4(f). The modeled mobility for both the conduction and valence bands has a temperature dependence close to $T^{-3/2}$ above 100 K, in agreement with acoustic phonon scattering.

In addition to the low-temperature effects discussed previously, there is another contribution to the discrepancy between the measured and modeled Seebeck and Hall coefficients. Because of the complex nature of the pentatellurides with a small band gap and layered structure, density-functional-theory calculations of the band structure have not always been in agreement [31,34,61,66]. Additionally, the calculated band structure is sensitive to the parameters used, including the temperature, stress or strain induced by chemical substitution, and pressure [27,58,59]. However, calculations typically show a single hole pocket centered around Γ with much higher energy than other pockets, while the conduction band has numerous pockets at comparable energy levels. As T increases, these pockets contribute to conduction leading to an increase in the Seebeck effective mass. This increase in mass is due to carriers being thermally generated across the

small gap due to broadening of the Fermi-Dirac distribution with the increasing temperature. A better fit to the experimental data can be achieved by either adding a third band or employing a temperature-dependent effective mass or band gap, but because exact fits are not expected due to the unconventional effects at low temperatures as previously discussed, the introduction of additional fitting parameters is not warranted. Nonetheless, this model does qualitatively reproduce the trends as a function of the temperature for the various property measurements.

C. Effect of varying carrier concentration

The two-band model fit to the experimental data can be extended to simulate properties at carrier concentrations not used for modeling, as shown in Fig. 5. This is done by adjusting the initial doping level in the calculations akin to experimental carrier concentration tuning using external dopants. As the *p*-type carrier concentration is increased, the peak in the Seebeck coefficient moves to a higher temperature and lower magnitude, while the resistivity peak decreases in magnitude. As the *n*-type carrier concentration is increased, the *n*-type Seebeck coefficient crosses 0 at a higher temperature for higher doping levels, while the resistivity peaks at a lower magnitude but a higher temperature. This qualitative behavior is in good agreement with previous measurements of single crystals with different carrier concentrations. Reports of iodine-vapor-grown crystals show n_H of approximately 1×10^{18} cm^{-3} at room temperature and an *n*-*p* transition temperature of about 130 K, while self-flux-grown single crystals had values of 5×10^{16} cm^{-3} and 60 K [13,24,25]. The trends from the two-band model in the Seebeck coefficient and resistivity are also in agreement with experiments where rare-earth elements are substituted for the transition metal (see Fig. S5 in the Supplemental Material [50] and Ref. [67]). The model predicts that at high *n*-type carrier concentrations, a negative Seebeck will persist to higher temperatures, as has been experimentally found for $Hf_{0.99}Ta_{0.01}Te_5$ up to at least 300 K [68].

As was previously discussed, the synthesis route used to produce the $ZrTe_5$ samples has a dramatic effect on the observed properties. Our model shows that the cause of the various properties found in different crystals is the carrier concentration variation due to processing. The traditional route for making single crystals of $ZrTe_5$, chemical-vapor-transport synthesis, is thought to produce pure samples. Iodine is used as the vapor-transport agent, so even though the crystals are washed after this procedure, it is unlikely that all iodine is removed. Substitution of I for Te will act as an electron donor causing *n*-type transport at low temperatures before the higher-mobility *p*-type conduction dominates as the carriers are thermally activated. Our model demonstrates how variations in the carrier concentration, in this case, due to unintentional doping with iodine, change the properties. This is experimentally verified by

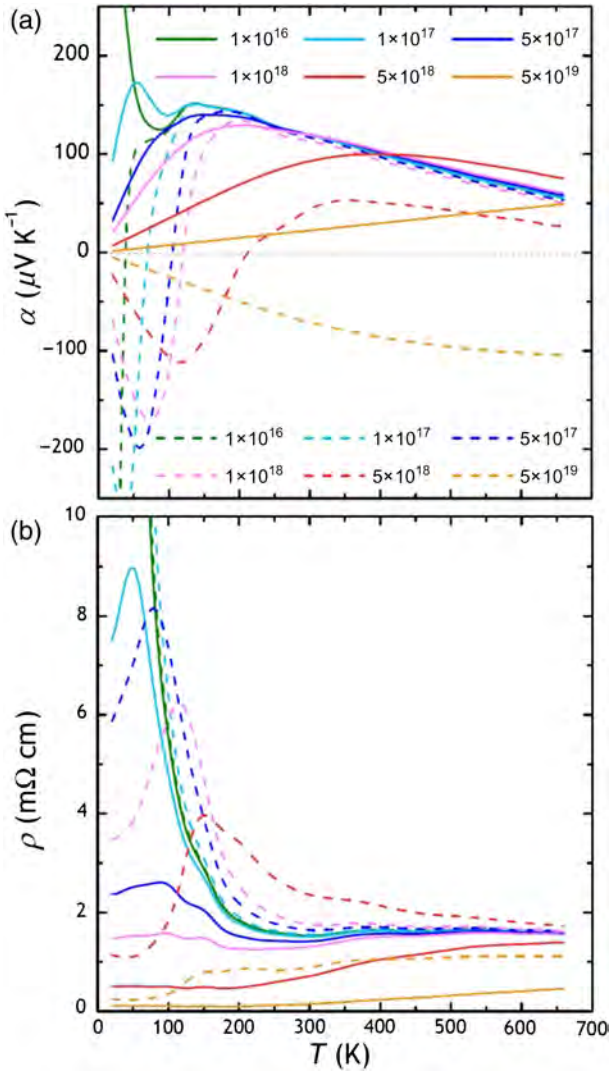

FIG. 5. The (a) Seebeck coefficient and (b) resistivity as a function of the temperature in polycrystalline $ZrTe_5$ for different doping levels (cm^{-3}) of both *p* (solid) and *n*-type (dashed) carriers.

measurements on undoped and iodine-doped polycrystalline samples. Additionally, the differences between Te self-flux-grown single crystals and undoped polycrystalline samples can be explained in the context of this model. $ZrTe_5$ is considered a line compound, though there is actually a finite phase width. So, while both the flux and solid-state reactions consist of only Zr and Te (no I), the ratio of the two elements may vary in the samples produced by different methods. This Zr:Te ratio will lead to changes in carrier concentration due to differences in actual (not nominal) stoichiometry. For example, Te vacancies caused by the high vapor pressure of tellurium will act as electron donors. Our model shows that the temperature and magnitude of the ρ peak as well as the *n*-*p* transition of α can be tuned by adjusting the carrier concentration accomplished through careful control of the Zr:Te ratio or dopant concentration.

D. Tuning model to optimize thermoelectric performance

Because of the reasons previously stated, we do not expect the model to be accurate at low temperatures, but the properties are well fit in the range of 200–600 K, where the peak zT is observed. Figure 6(a) shows the zT as a function of the temperature for various doping levels, while Fig. 6(b) shows the zT vs doping level for both p- and n-type samples at various temperatures. With low doping levels, bipolar conduction sets in by 200 K, leading to modest zT. However, as the doping level is increased, the maximum zT increases as the Fermi level is pinned into one band or the other. Controlling the carrier concentration allows for optimization of the zT in a desired temperature range.

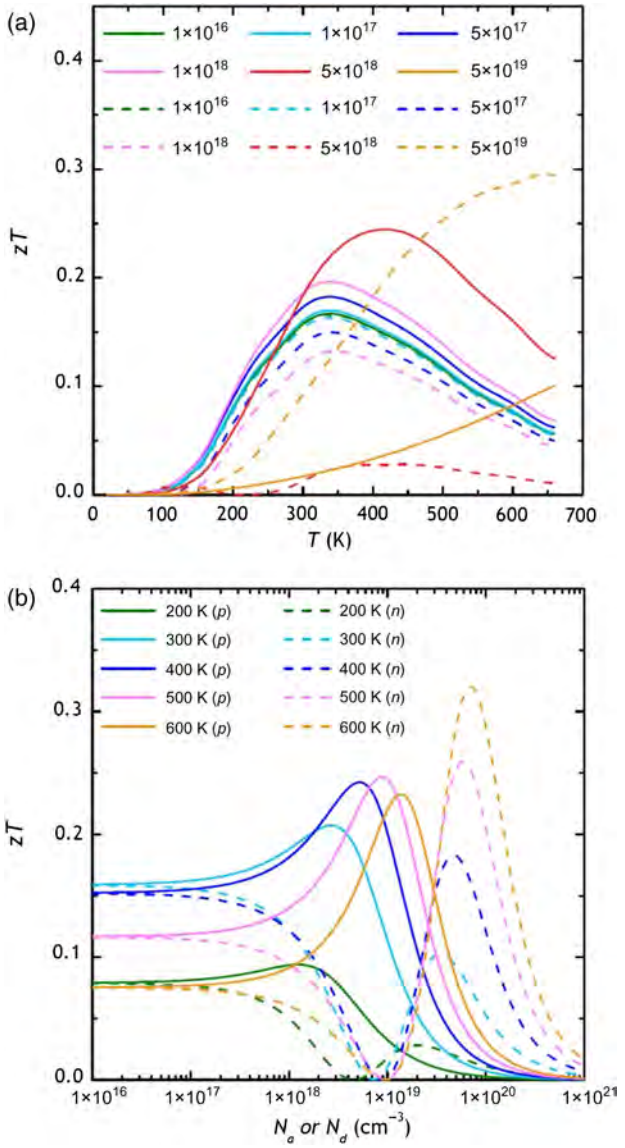

FIG. 6. For polycrystalline $ZrTe_5$, (a) the zT as a function of temperature at various acceptor (solid) or donor (dashed) levels, and (b) the zT as a function of dopant concentration for temperatures ranging from 200 to 600 K.

Using the model for predictions, strategies can be devised for optimizing the thermoelectric performance of $ZrTe_5$. By increasing the band gap, minority-carrier contributions can be suppressed, increasing the zT to approximately 0.4 at 300 K. Increasing the band gap can be achieved by substitution of Se for Te, as demonstrated previously [68]. Using our two-band model, we can estimate the zT contributions of each band independently. From this, we observe that engineering the composition such that the mobility of the minority carrier is reduced by a factor of 10 will also increase the zT at 300 K to approximately 0.35 for p type. A two- to threefold reduction in the lattice thermal conductivity through grain size reduction, softening of the lattice, alloying, or other strategies will potentially lead to a zT near 1 at room temperature. Furthermore, by controlling the carrier concentration through doping, n and p legs can be made in the $ZrTe_5$ system, providing the opportunity to make modules out of a single compound, thus, mitigating issues with chemical and thermal compatibility.

IV. CONCLUSIONS

The details of transport in the $HfTe_5$ and $ZrTe_5$ systems have been debated for many years due to the exotic transport properties observed in single crystals. The measurement of polycrystalline $ZrTe_5$ samples reveals p-type behavior at all temperatures, leading to a conjecture that the system can be explained as a semiconductor. Doping $ZrTe_5$ with iodine leads to properties similar to previous reports on single crystals, with an n to p transition near 130 K, suggesting that prior work on pentatellurides may have been contaminated by residual iodine from the typical iodine-vapor-transport synthesis. A two-band model is constructed which accurately describes the properties of polycrystalline samples as well as explains the behavior of both flux- and vapor-grown single crystals. The model has a temperature-independent band gap of 0.02 eV, a valence band with a higher mobility, and a conduction band with a higher effective mass. The experimental data are consistent with a semiconductor having a positive finite gap where the anomalous resistivity peak and change in Seebeck coefficient can be simultaneously explained. Finally, the model allows for prediction of zT by carrier concentration tuning and other strategies to optimize the thermoelectric performance. $ZrTe_5$ is promising for practical applications, as a thermoelectric device can be constructed out of a single material used for both legs.

ACKNOWLEDGMENTS

The authors thank Thomas O. Mason for helpful discussions. We acknowledge primary support from the National Science Foundation Division of Materials Research (DMR) program, Grants No. 1334713, No. 1334351, and No. 1333335. The research is performed using computational resources sponsored by the

Department of Energy's Office of Energy Efficiency and Renewable Energy and located at the National Renewable Energy Laboratory (NREL). Research is supported as part of the Solid-State Solar-Thermal Energy Conversion Center, an Energy Frontier Research Center funded by the U.S. Department of Energy, Office of Science, Basic Energy Sciences under Award No. DE-SC0001299/DE-FG02-09ER46577. Low-temperature magnetoresistance measurements made with support from Air Force Office of Scientific Research (AFOSR) Grants No. FA9550-15-1-0247 and No. FA9550-15-1-0377. The work at Argonne National Laboratory is supported by the U.S. Department of Energy, Office of Science, Basic Energy Sciences, Materials Sciences and Engineering Division under Contract No. DE-AC02-06CH11357. This work made use of the J. B. Cohen X-Ray Diffraction Facility supported by the Materials Research Science and Engineering Centers (MRSEC) program of the National Science Foundation (NSF) (Grant No. DMR-1121262) at the Materials Research Center of Northwestern University and the Soft and Hybrid Nanotechnology Experimental Resource (NSF Grant No. NNCI-1542205).

[1] D. M. Rowe, *CRC Handbook of Thermoelectrics* (CRC Press, Boca Raton, FL, 1995).

[2] C. B. Vining, W. Laskow, J. O. Hanson, R. R. Van der Beck, and P. D. Gorsuch, Thermoelectric properties of pressure-sintered $Si_{0.8}Ge_{0.2}$ thermoelectric alloys, J. Appl. Phys. **69**, 4333 (1991).

[3] S. R. Brown, S. M. Kauzlarich, F. Gascoin, and G. J. Snyder, $Yb_{14}MnSb_{11}$: New high efficiency thermoelectric material for power generation, Chem. Mater. **18**, 1873 (2006).

[4] S. Ohno, U. Aydemir, M. Amsler, J.-H. Pöhls, S. Chanakian, A. Zevalkink, M. A. White, S. K. Bux, C. Wolverton, and G. J. Snyder, Achieving $zT > 1$ in inexpensive Zintl phase $Ca_9Zn_{4+x}Sb_9$ by phase boundary mapping, Adv. Funct. Mater. **27**, 1606361 (2017).

[5] C. A. Uvarov, J. F. Rauscher, and S. M. Kauzlarich, High temperature thermoelectric properties of $Yb_{14-x}Ca_xMnSb_{11}$ made by reaction of the elements, Sci. Technol. Adv. Mater. **3**, 646 (2011).

[6] H. Jin, C. M. Jaworski, and J. P. Heremans, Enhancement in the figure of merit of *p*-type $Bi_{100-x}Sb_x$ alloys through multiple valence-band doping, Appl. Phys. Lett. **101**, 053904 (2012).

[7] S. Cho, A. DiVenere, G. K. Wong, J. B. Ketterson, and J. R. Meyer, Transport properties of $Bi_{1-x}Sb_x$ alloy thin films grown on CdTe(111)B, Phys. Rev. B **59**, 10691 (1999).

[8] D.-Y. Chung, T. P. Hogan, M. Rocci-Lane, P. Brazis, J. R. Ireland, C. R. Kannewurf, M. Bastea, C. Uher, and M. G. Kanatzidis, A new thermoelectric material: $CsBi_4Te_6$, J. Am. Chem. Soc. **126**, 6414 (2004).

[9] L. Lykke, B. B. Iversen, and G. K. H. Madsen, Electronic structure and transport in the low-temperature thermoelectric $CsBi_4Te_6$: Semiclassical transport equations, Phys. Rev. B **73**, 195121 (2006).

[10] D. A. Wright, Thermoelectric properties of bismuth telluride and its alloys, Nature (London) **181**, 834 (1958).

[11] D. Kusano and Y. Hori, Thermoelectric properties of *p*-type $(Bi_2Te_3)_{0.2}(Sb_2Te_3)_{0.8}$ thermoelectric material doped with PbTe, J. Jpn. Inst. Met. **66**, 1063 (2002).

[12] S. LeBlanc, Thermoelectric generators: Linking material properties and systems engineering for waste heat recovery applications, Sustain. Mater. Technol. **1**, 26 (2014).

[13] R. T. Littleton IV, T. M. Tritt, J. W. Kolis, and D. R. Ketchum, Transition-metal pentatellurides as potential low-temperature thermoelectric refrigeration materials, Phys. Rev. B **60**, 13453 (1999).

[14] N. D. Lowhorn, T. M. Tritt, E. E. Abbott, and J. W. Kolis, Enhancement of the power factor of the transition metal pentatelluride $HfTe_5$ by rare-earth doping, Appl. Phys. Lett. **88**, 022101 (2006).

[15] B. M. Zawilski, R. T. Littleton IV, and T. M. Tritt, Investigation of the thermal conductivity of the mixed pentatellurides $Hf_{1-x}Zr_xTe_5$, Appl. Phys. Lett. **77**, 2319 (2000).

[16] S. A. Miller, P. Gorai, B. R. Ortiz, A. Goyal, D. Gao, S. A. Barnett, T. O. Mason, G. J. Snyder, Q. Lv, V. Stevanović, and E. S. Toberer, Capturing anharmonicity in a lattice thermal conductivity model for high-throughput predictions, Chem. Mater. **29**, 2494 (2017).

[17] J. Yan, P. Gorai, B. Ortiz, S. Miller, S. A. Barnett, T. Mason, V. Stevanović, and E. S. Toberer, Material descriptors for predicting thermoelectric performance, Energy Environ. Sci. **8**, 983 (2015).

[18] P. Gorai, D. Gao, B. Ortiz, S. Miller, S. A. Barnett, T. Mason, Q. Lv, V. Stevanović, and E. S. Toberer, TE Design Lab: A virtual laboratory for thermoelectric material design, Comput. Mater. Sci. **112**, 368 (2016).

[19] P. Gorai, E. S. Toberer, and V. Stevanović, Computational identification of promising thermoelectric materials among known quasi-2D binary compounds, J. Mater. Chem. A **4**, 11110 (2016).

[20] E. F. Skelton, T. J. Wieting, S. A. Wolf, W. W. Fuller, D. U. Gubser, T. L. Francavilla, and F. Levy, Giant resistivity and x-ray diffraction anomalies in low-dimensional $ZrTe_5$ and $HfTe_5$, Solid State Commun. **42**, 1 (1982).

[21] F. J. DiSalvo, R. M. Fleming, and J. V. Waszczak, Possible phase transition in the quasi-one-dimensional materials $ZrTe_5$ or $HfTe_5$, Phys. Rev. B **24**, 2935 (1981).

[22] S. Okada, T. Sambongi, M. Ido, Y. Tazuke, R. Aoki, and O. Fujita, Negative evidences for charge/spin density wave in $ZrTe_5$, J. Phys. Soc. Jpn. **51**, 460 (1982).

[23] M. Rubinstein, $HfTe_5$ and $ZrTe_5$: Possible polaronic conductors, Phys. Rev. B **60**, 1627 (1999).

[24] P. Shahi, D. J. Singh, J. P. Sun, L. X. Zhao, G. F. Chen, J.-Q. Yan, D. G. Mandrus, and J.-G. Cheng, Bipolar conduction is the origin of the electronic transition in pentatellurides: Metallic vs. semiconducting behavior, arXiv:1611.06370.

[25] H. Chi, C. Zhang, G. Gu, D. E. Kharzeev, X. Dai, and Q. Li, Lifshitz transition mediated electronic transport anomaly in bulk $ZrTe_5$, New J. Phys. **19**, 015005 (2017).

[26] W. Yu, Y. Jiang, J. Yang, Z. L. Dun, H. D. Zhou, Z. Jiang, P. Lu, and W. Pan, Quantum oscillations at integer and fractional Landau level indices in single-crystalline $ZrTe_5$, Sci. Rep. **6**, 35357 (2016).

[27] H. Weng, X. Dai, and Z. Fang, Transition-Metal Pentatelluride $ZrTe_5$ and $HfTe_5$: A Paradigm for Large-Gap Quantum Spin Hall Insulators, Phys. Rev. X **4**, 011002 (2014).

[28] Q. Li, D. E. Kharzeev, C. Zhang, Y. Huang, I. Pletikosić, A. V. Fedorov, R. D. Zhong, J. A. Schneeloch, G. D. Gu, and T. Valla, Chiral magnetic effect in $ZrTe_5$, Nat. Phys. **12**, 550 (2016).

[29] H. Wang, C.-K. Li, H. Liu, J. Yan, J. Wang, J. Liu, Z. Lin, Y. Li, Y. Wang, L. Li, D. Mandrus, X. C. Xie, J. Feng, and J. Wang, Chiral anomaly and ultrahigh mobility in crystalline $HfTe_5$, Phys. Rev. B **93**, 165127 (2016).

[30] H. Wang, H. Liu, Y. Li, Y. Liu, J. Wang, J. Liu, Y. Wang, L. Li, J. Yan, D. Mandrus, X. C. Xie, and J. Wang, Discrete scale invariance and fermionic Efimov states in ultraquantum $ZrTe_5$, arXiv:1704.00995.

[31] Z. Fan, Q.-F. Liang, Y. B. Chen, S.-H. Yao, and J. Zhou, Transition between strong and weak topological insulator in $ZrTe_5$ and $HfTe_5$, Sci. Rep. **7**, 45667 (2017).

[32] D. N. McIlroy, S. Moore, D. Zhang, J. Wharton, B. Kempton, R. Littleton, M. Wilson, T. M. Tritt, and C. G. Olson, Observation of a semimetal-semiconductor phase transition in the intermetallic $ZrTe_5$, J. Phys. Condens. Matter **16**, L359 (2004).

[33] X.-B. Li, W.-K. Huang, Y.-Y. Lv, K.-W. Zhang, C.-L. Yang, B.-B. Zhang, Y. B. Chen, S.-H. Yao, J. Zhou, M.-H. Lu, L. Sheng, S.-C. Li, J.-F. Jia, Q.-K. Xue, Y.-F. Chen, and D.-Y. Xing, Experimental Observation of Topological Edge States at the Surface Step Edge of the Topological Insulator $ZrTe_5$, Phys. Rev. Lett. **116**, 176803 (2016).

[34] R. Wu, J.-Z. Ma, S.-M. Nie, L.-X. Zhao, X. Huang, J.-X. Yin, B.-B. Fu, P. Richard, G.-F. Chen, Z. Fang, X. Dai, H.-M. Weng, T. Qian, H. Ding, and S. H. Pan, Evidence for Topological Edge States in a Large Energy Gap Near the Step Edges on the Surface of $ZrTe_5$, Phys. Rev. X **6**, 021017 (2016).

[35] A. Pariari and P. Mandal, Coexistence of topological Dirac fermions on the surface and three-dimensional Dirac cone state in the bulk of $ZrTe_5$ single crystal, Sci. Rep. **7**, 40327 (2017).

[36] G. Zheng, J. Lu, X. Zhu, W. Ning, Y. Han, H. Zhang, J. Zhang, C. Xi, J. Yang, H. Du, K. Yang, Y. Zhang, and M. Tian, Transport evidence for the three-dimensional Dirac semimetal phase in $ZrTe_5$, Phys. Rev. B **93**, 115414 (2016).

[37] K. A. Borup, E. S. Toberer, L. D. Zoltan, G. Nakatsukasa, M. Errico, J.-P. Fleurial, B. B. Iversen, and G. J. Snyder, Measurement of the electrical resistivity and Hall coefficient at high temperatures, Rev. Sci. Instrum. **83**, 123902 (2012).

[38] C. Wood, D. Zoltan, and G. Stapfer, Measurement of Seebeck coefficient using a light pulse, Rev. Sci. Instrum. **56**, 719 (1985).

[39] A. F. May and G. J. Snyder, *Materials, Preparation, and Characterization in Thermoelectrics* (CRC Press, Boca Raton, FL, 2012), pp. 1–18.

[40] A. F. May, D. J. Singh, and G. J. Snyder, Influence oband structure on the large thermoelectric performance of lanthanum telluride, Phys. Rev. B **79**, 153101 (2009).

[41] D. J. Singh and W. E. Pickett, Skutterudite antimonides: Quasilinear bands and unusual transport, Phys. Rev. B **50**, 11235 (1994).

[42] D. J. Singh and I. I. Mazin, Calculated thermoelectric properties of La-filled skutterudites, Phys. Rev. B **56**, R1650 (1997).

[43] R. T. Littleton IV, T. M. Tritt, C. R. Feger, J. Kolis, M. L. Wilson, M. Marone, J. Payne, D. Verebeli, and F. Levy, Effect of Ti substitution on the thermoelectric properties of the pentatelluride materials $M_{1-x}Ti_xTe_5$ (M = Hf, Zr), Appl. Phys. Lett. **72**, 2056 (1998).

[44] M. Izumi, K. Uchinokura, E. Matsuura, and S. Harada, Hall effect and transverse magnetoresistance in a low-dimensional conductor $HfTe_5$, Solid State Commun. **42**, 773 (1982).

[45] M. Izumi, T. Nakayama, K. Uchinokura, S. Harada, R. Yoshizaki, and E. Matsuura, Shubnikov–de Haas oscillations and Fermi surfaces in transition-metal pentatellurides $ZrTe_5$ and $HfTe_5$, J. Phys. C **20**, 3691 (1987).

[46] W. W. Fuller, S. A. Wolf, T. J. Wieting, R. C. LaCoe, P. M. Chaikin, and C. Y. Huang, Pressure effects in $HfTe_5$ and $ZrTe_5$, J. Phys. (Paris), Colloq. **44**, C3-1709 (1983).

[47] R. T. Littleton IV, T. M. Tritt, J. W. Kolis, D. R. Ketchum, N. D. Lowhorn, and M. B. Korzenski, Suppression of the resistivity anomaly and corresponding thermopower behavior in the pentatelluride system by the addition of Sb: $Hf_{1-X}Zr_XTe_{5-Y}Sb_Y$, Phys. Rev. B **64**, 121104 (2001).

[48] T. E. Jones, W. W. Fuller, T. J. Wieting, and F. Levy, Thermoelectric power of $HfTe_5$ and $ZrTe_5$, Solid State Commun. **42**, 793 (1982).

[49] T. M. Tritt, N. D. Lowhorn, R. T. Littleton IV, A. Pope, C. R. Feger, and J. W. Kolis, Large enhancement of the resistive anomaly in the pentatelluride materials $HfTe_5$ and $ZrTe_5$ with applied magnetic field, Phys. Rev. B **60**, 7816 (1999).

[50] See the Supplemental Material at http://link.aps.org/supplemental/10.1103/PhysRevApplied.9.014025 for x-ray diffraction patterns, Rietveld refinement, and raw transport data.

[51] L. Akselrud and Y. Grin, WinCSD: Software package for crystallographic calculations (Version 4), J. Appl. Crystallogr. **47**, 803 (2014).

[52] H. Fjellvåg and A. Kjekshus, Structural properties of $ZrTe_5$ and $HfTe_5$ as seen by powder diffraction, Solid State Commun. **60**, 91 (1986).

[53] J. Wang, A. M. DaSilva, C.-Z. Chang, K. He, J. K. Jain, N. Samarth, X.-C. Ma, Q.-K. Xue, and M. H. W. Chan, Evidence for electron-electron interaction in topological insulator thin films, Phys. Rev. B **83**, 245438 (2011).

[54] Y. Zhang *et al.*, Electronic evidence of temperature-induced Lifshitz transition and topological nature in $ZrTe_5$, Nat. Commun. **8**, 15512 (2017).

[55] R. Y. Chen, S. J. Zhang, J. A. Schneeloch, C. Zhang, Q. Li, G. D. Gu, and N. L. Wang, Optical spectroscopy study of the three-dimensional Dirac semimetal $ZrTe_5$, Phys. Rev. B **92**, 075107 (2015).

[56] L. Moreschini, J. C. Johannsen, H. Berger, J. Denlinger, C. Jozwiak, E. Rotenberg, K. S. Kim, A. Bostwick, and M. Grioni, Nature and topology of the low-energy states in $ZrTe_5$, Phys. Rev. B **94**, 081101 (2016).

[57] R. Y. Chen, Z. G. Chen, X.-Y. Song, J. A. Schneeloch, G. D. Gu, F. Wang, and N. L. Wang, Magnetoinfrared Spectroscopy of Landau Levels and Zeeman Splitting of Three-Dimensional massless Dirac Fermions in $ZrTe_5$, Phys. Rev. Lett. **115**, 176404 (2015).

[58] Y. Liu, X. Yuan, C. Zhang, Z. Jin, A. Narayan, C. Luo, Z. Chen, L. Yang, J. Zou, X. Wu, S. Sanvito, Z. Xia, L. Li, Z. Wang, and F. Xiu, Zeeman splitting and dynamical mass generation in Dirac semimetal $ZrTe_5$, Nat. Commun. **7**, 12516 (2016).

[59] Y. Zhou, J. Wu, W. Ning, N. Li, Y. Du, X. Chen, R. Zhang, Z. Chi, X. Wang, X. Zhu, P. Lu, C. Ji, X. Wan, Z. Yang, J. Sun, W. Yang, M. Tian, Y. Zhang, and H.-k. Mao, Pressure-induced superconductivity in a three-dimensional topological material $ZrTe_5$, Proc. Natl. Acad. Sci. U.S.A. **113**, 2904 (2016).

[60] W. Shockley, *Electrons and Holes in Semiconductors* (Van Nostrand, Princeton, 1953).

[61] G. N. Kamm, D. J. Gillespie, A. C. Ehrlich, T. J. Wieting, and F. Levy, Fermi surface, effective masses, and Dingle temperatures of $ZrTe_5$ as derived from the Shubnikov–de Haas effect, Phys. Rev. B **31**, 7617 (1985).

[62] H. Xiong, J. A. Sobota, S.-L. Yang, H. Soifer, A. Gauthier, M.-H. Lu, Y.-Y. Lv, S.-H. Yao, D. Lu, M. Hashimoto, P. S. Kirchmann, Y.-F. Chen, and Z.-X. Shen, Three-dimensional nature of the band structure of $ZrTe_5$ measured by high-momentum-resolution photoemission spectroscopy, Phys. Rev. B **95**, 195119 (2017).

[63] G. Qiu, Y. Du, A. Charnas, H. Zhou, S. Jin, Z. Luo, D. Y. Zemlyanov, X. Xu, G. J. Cheng, and P. D. Ye, Observation of optical and electrical in-plane anisotropy in high-mobility few-layer $ZrTe_5$, Nano Lett. **16**, 7364 (2016).

[64] Y.-Y. Lv, F. Zhang, B.-B. Zhang, B. Pang, S.-H. Yao, Y. B. Chen, L. Ye, J. Zhou, S.-T. Zhang, and Y.-F. Chen, Microstructure, growth mechanism and anisotropic resistivity of quasi-one-dimensional $ZrTe_5$ crystal, J. Cryst. Growth **457**, 250 (2017).

[65] M. K. Hooda and C. S. Yadav, Enhanced thermopower and low thermal conductivity in *p*-type polycrystalline $ZrTe_5$, Appl. Phys. Lett. **111**, 053902 (2017).

[66] M.-H. Whangbo, F. J. DiSalvo, and R. M. Fleming, Electronic structure of $ZrTe_5$, Phys. Rev. B **26**, 687 (1982).

[67] N. D. Lowhorn, T. M. Tritt, E. E. Abbott, and J. W. Kolis, in *Proceedings of the 24th International Conference on Thermoelectrics, ICT 2005* (IEEE, New York, 2005), pp. 41–45.

[68] R. T. Littleton IV, Ph.D. thesis, Clemson University, 2001.